
Theses and Dissertations

Summer 2017

Search for heavy Majorana neutrinos in pp collisions at $\sqrt{s} = 8$ TeV with the CMS detector & photodetector and calorimeter R&D for particle colliders.

Emrah Tiras
University of Iowa

Follow this and additional works at: <https://ir.uiowa.edu/etd>

 Part of the [Physics Commons](#)

Copyright © 2017 Emrah Tiras


This dissertation is available at Iowa Research Online: <https://ir.uiowa.edu/etd/5864>

Recommended Citation

Tiras, Emrah. "Search for heavy Majorana neutrinos in pp collisions at $\sqrt{s} = 8$ TeV with the CMS detector & photodetector and calorimeter R&D for particle colliders.." PhD (Doctor of Philosophy) thesis, University of Iowa, 2017.

<https://doi.org/10.17077/etd.5keerkqm>

Follow this and additional works at: <https://ir.uiowa.edu/etd>

 Part of the [Physics Commons](#)

SEARCH FOR HEAVY MAJORANA NEUTRINOS IN PP COLLISIONS AT \sqrt{s}
= 8 TEV WITH THE CMS DETECTOR
&
PHOTODETECTOR AND CALORIMETER R&D FOR PARTICLE COLLIDERS

by

Emrah Tiras

A thesis submitted in partial fulfillment of the
requirements for the Doctor of Philosophy
degree in Physics
in the Graduate College of
The University of Iowa

August 2017

Thesis Supervisors: Professor Yasar Onel
Associate Professor Jane Nachtman

Copyright by
EMRAH TIRAS
2017
All Rights Reserved

Graduate College
The University of Iowa
Iowa City, Iowa

CERTIFICATE OF APPROVAL

PH.D. THESIS

This is to certify that the Ph.D. thesis of

Emrah Tiras

has been approved by the Examining Committee for the
thesis requirement for the Doctor of Philosophy degree
in Physics at the August 2017 graduation.

Thesis committee: _____
Yasar Onel, Thesis Supervisor

Jane Nachtman, Thesis Supervisor

Markus Wohlgenannt

Robert L. Merlino

John Ellison

To my family, Osman Kerem and Kevser, who kept me awake through the nights...

ACKNOWLEDGEMENTS

I would like to express my special appreciation and thanks to my advisor Prof. Yasar Onel, who opened the particle and nuclear physics' door to me. This thesis could not have been achieved without his support. I deeply appreciate him for his generous assistance and being around when needed.

I would like to thank my co-advisor Assoc. Prof. Jane Nachtman greatly for encouraging my research and for her invaluable help in the preparation of this dissertation. Her advice and help throughout my Ph.D. years have been priceless.

I also would like to thank the other thesis committee members: Prof. Markus Wohlgemant and Prof. Robert L. Merlino from the University of Iowa (UI), and Prof. John Ellison from the University of California, Riverside.

Further, I would like to thank all the professors, and administrative and support staff of the Department of Physics and Astronomy at UI for their kindness and support.

I would like to acknowledge the CMS Exotica Heavy Majorana Neutrino Search Group under the supervisions of Prof. John Ellison and Assoc. Prof. Un-ki Yang. Many thanks to Dr. James Wetzel, Dr. Warren Clarida, Dr. John Almond and Dr. Ferdinando Giordano for their useful hints for improving my physics research and this dissertation.

Special thanks to detector R&D group at UI, specifically Dr. Burak Bilki and Dr. James Wetzel who conveyed me much knowledge of particle physics and

provided constructive suggestions. Every moment was great with you, even the owl shifts during the beam tests at Fermilab and CERN.

It is also a pleasure to acknowledge my graduate student friends and colleagues, especially the group members of the High Energy & Nuclear Physics at UI: Dr. Kamuran Dilsiz, Dr. Hasan Ogul, Dr. Maksat Haytmyradov, Dr. Reddy Pratap Gandrajula, Suleyman Durgut and Christina M. Snyder who especially helped me by proofreading and editing this thesis manuscript.

Last but not least, I would like to express my love and gratitude to my beloved wife Kevser, my son Osman Kerem, and our parents for their endless love and support through the duration of my studies.

ABSTRACT

This thesis contains both physics analysis and hardware studies. It consists of two primary sections: the results of a search for heavy Majorana mass neutrinos, using the event signature of same (like) sign charged electron pairs ($e^\pm e^\pm$) and two jets, and the results of studies to upgrade the Hadronic Forward (HF) and Hadronic Endcap (HE) subdetectors in the Compact Muon Solenoid (CMS) detector in response to the high intensity proton-proton collisions generated at the Large Hadron Collider (LHC) at European Organization for Nuclear Research (CERN, Conseil Européen pour la Recherche Nucléaire).

In this search for Majorana mass neutrinos, same sign dielectron ($e^\pm e^\pm$) + dijet events in the final state have been considered as a signature for neutrino particles. The analyzed data corresponds to an integrated luminosity of 19.7 fb^{-1} of proton-proton collisions at a center of mass energy of $\sqrt{s} = 8 \text{ TeV}$, collected using the CMS detector during the 2012 operation at the LHC. Monte Carlo simulations accounting for the theoretical expectations of the Standard Model (SM) and the detector limitations, are used to prototype the experiment and to test proposed analysis steps. No excess of events is observed in the data beyond the expected SM background. Upper limits are set on the mixing element squared, $|V_{eN}|^2$, of the heavy Majorana neutrino with standard model neutrinos, as a function of Majorana neutrino mass for masses in the range of $40\text{-}500 \text{ GeV}/c^2$.

The detector upgrade search comprises three sections of this thesis. The first

section describes the test results of 1785 multianode Hamamatsu R7600U-200-M4 photomultiplier tubes (PMT) in numerous parameters such as gain, dark current, and timing characteristics, which provide insights on the expected performance of the upgraded CMS-HF detector. These PMTs replaced the previous single anode R7525 PMTs because the glass windows of previous PMTs are the source of Cherenkov radiation, which causes a background noise in the experiment. The second section reports characterization results of two types of PMTs in a novel operation mode for Secondary Emission (SE) Ionization Calorimetry, which is a novel technique to measure electromagnetic shower particles in extreme radiation environments.

The third section presents the test results of novel scintillating materials for CMS experiment in specific and future particle accelerators in general. These materials are Polyethylene Naphthalate (PEN), Polyethylene Terephthalate (PET), high efficiency mirror (HEM) and quartz plates with various organic and inorganic coating materials such as p-Terphenyl (pTp), Anthracene and Gallium-doped Zinc Oxide (ZnO:Ga). We have investigated them for radiation hardness, light yield, timing characteristics, and scintillation and transmission properties.

PUBLIC ABSTRACT

In high energy and nuclear physics, experimental work is a combination of physics analysis and detector hardware development. This thesis contains both software and hardware studies for the Compact Muon Solenoid (CMS) experiment at Large Hadron Collider (LHC) at CERN completed over the years of author's Ph.D. studies. The physics analysis in this thesis is about neutrinos, one of the most abundant particles in the universe. Neutrinos are neutral and massless particles according to the Standard Model (SM), which is currently the best theory for understanding the nature of the universe. However, confirmation of neutrino oscillation by cosmic, reactor and accelerator experiments has shown that neutrinos can be chargeless but not massless. To account for this discrepancy in the SM we include the Seesaw Mechanism, which incorporates a light neutrino and a heavy Majorana neutrino. This study concentrates on the search for the heavy Majorana neutrinos using same sign dielectron ($e^\pm e^\pm$) + jets events. The analyzed data was collected when the LHC proton-proton collisions had a center-of-mass energy of 8 TeV and an integrated luminosity of 19.7 fb^{-1} .

To test the predictions of the SM and beyond, we have very complicated particle accelerators and detectors. The most complex particle accelerator used in the world is LHC which is the home of four main experiments; ALICE, ATLAS, CMS and LHCb. The second part of the thesis focuses on the detector research and development for CMS, specifically for Hadronic Forward (HF) and Hadronic Endcap

(HE) calorimeters, subdetectors of the CMS. During the HF calorimeter upgrade, 1785 multianode photomultiplier tubes (PMT) replaced the old single anode PMTs. We tested gain, dark current, time characteristics and linearity of these tubes, which provide insights on the expected performance of the upgraded CMS-HF detector. For the upcoming HE calorimeter upgrade, we investigated several scintillating materials. We have introduced novel, radiation resistant and cheap scintillating materials such as Polyethylene Naphthalate (PEN), Polyethylene Terephthalate (PET), High Efficiency Mirror (HEM) and quartz plates with various organic and inorganic coating materials such as p-Terphenyl (pTp), Anthracene and Gallium-doped Zinc Oxide (ZnO:Ga) to the CMS experiment and other particle physics experiments around the world. We have investigated them for radiation resistance, timing characteristics, and transmission and emission properties.

TABLE OF CONTENTS

LIST OF TABLES	xii
LIST OF FIGURES	xiv
CHAPTER	
1 INTRODUCTION	1
2 THEORETICAL BACKGROUND	5
2.1 The Standard Model	5
2.2 Misfits of the Standard Model: Neutrinos	6
3 LHC AND CMS EXPERIMENTAL APPARATUS	10
3.1 Large Hadron Collider	10
3.2 Compact Muon Solenoid (CMS)	14
3.2.1 The Tracker	18
3.2.2 Electromagnetic Calorimeter	19
3.2.3 Hadronic Calorimeter	20
3.2.4 Hadronic Forward Calorimeter (HF)	21
3.2.5 Muon System	22
3.3 LHC Shutdowns and CMS Detector Upgrades	24
3.3.1 Phase I	24
3.3.2 Phase II	26
4 MAJORANA NEUTRINO SEARCH	27
4.1 Introduction	27
4.2 Datasets and Monte Carlo Event Samples	31
4.2.1 2012 Collision Data	31
4.2.2 Monte Carlo Signal Generation for Majorana Neutrino	32
4.2.3 Standard Model Monte Carlo Samples	34
4.3 Event Selection	34
4.3.1 Trigger	34
4.3.2 Primary Vertex Selection	36
4.3.3 Electron Selection	37
4.3.4 Muon Selection	38
4.3.5 Jet and E_T^{miss} Selection	38

4.3.6	Preselection Requirements	39
4.3.7	Additional Selection Requirements	40
4.3.8	Final Optimization for Signal Selection	41
4.4	Selection Efficiency	42
4.4.1	Tag and Probe Study: Data and Monte Carlo Scale Factor	45
4.5	Background Estimation	52
4.6	Systematic Uncertainties	53
4.7	Search Results	54
4.7.1	Results for Low Mass Search Region	54
4.7.2	Results for High Mass Search Region	57
4.7.3	Exclusion Limits	59
5	CMS HF CALORIMETER UPGRADE: PMT CHARACTERIZATION	62
5.1	HF Calorimeter Upgrade	62
5.2	Importance of the Multi-Anode PMTs Replacement	67
5.3	Gain Measurements	72
5.4	Dark Current Measurements	75
5.5	Timing Measurements	77
5.5.1	Pulse Width	77
5.5.2	Rise Time	78
5.5.3	Transit Time	78
5.5.4	Transit Time Spread	79
5.5.5	Single Pulse Linearity	79
5.6	Summary of the PMT Results	82
6	SECONDARY EMISSION IONIZATION CALORIMETRY	83
6.1	Introduction	83
6.2	Technical Design	86
6.3	Laboratory Measurements and Results	90
6.4	Conclusion	96
7	RADIATION HARD SCINTILLATING MATERIAL SEARCH	98
7.1	Novel Scintillating Materials	99
7.2	Laboratory Measurements	102
7.2.1	Scintillation and Transmission Measurements	103
7.2.2	Timing Measurements	108
7.2.3	Radiation Damage Studies	110
7.2.4	LED Stimulated Recovery Studies	113
7.3	Test Beam Activities and Results	118
7.4	Summary of Laboratory and Test Beam Studies	124

8	CONCLUSIONS AND FUTURE PERSPECTIVE	128
8.1	Future Work	131
	APPENDIX	133
A	MAJORANA NEUTRINO SEARCH RESULTS IN $\mu^\pm\mu^\pm$ (DIMUON) + JETS EVENTS	133
B	MAJORANA NEUTRINO SEARCH RESULTS IN $E^\pm\mu^\pm, \mu^\pm E^\pm$ + JETS EVENTS	135
	REFERENCES	137

LIST OF TABLES

Table

4.1	Summary of the 2012 complete datasets used for Majorana neutrino search in $e^\pm e^\pm + \text{jets}$ events.	31
4.2	Summary of Majorana neutrino signal Monte Carlo samples.	33
4.3	The abbreviations used in Table 4.2.	33
4.4	Summary of the used Monte Carlo datasets for the Standard Model processes.	35
4.5	The abbreviations used in Table 4.4	36
4.6	Summary of the selection requirements for the low-mass and high-mass signal regions.	41
4.7	Summary of the final optimization cuts on five variables and overall signal acceptance	43
4.8	The efficiency to select two isolated electrons with $p_T > 20, 15 \text{ GeV}/c$ passing all the selection cuts.	44
4.9	Event selection efficiencies for the events passing all the selection cuts. . .	45
4.10	Electron identification (including isolation) efficiencies in bins of p_T and $ \eta $ for both simulation and data measured with the tag-and-probe method.	50
4.11	Summary of the systematic uncertainties for Majorana neutrino signal and Standard Model background	54
5.1	Specifications for previous and current PMTs for HF calorimeter of the CMS Detector.	71
5.2	Summary of gain results of R7600U-200-M4 PMTs.	75
5.3	Summary of dark current results of R7600U-200-M4 PMTs.	77
5.4	Summary of timing characteristics of R7600U-200-M4 PMTs.	80

6.1	Summary of gains for Mode 1 and Mode 2 of R5900-00-M16 PMTs. . . .	95
6.2	Summary of gains for Mode 1, Mode 2 and Mode 3 of R7761 PMTs. . . .	96
7.1	Summary of the PEN and PET light yield results	113
7.2	Summary of the recovery plots of SiX, EJN and EJ2P with fit paramaters 'a', 'b', and 'c' of data points	118
7.3	Summary of light yield (MIP response) and timing responses of the scin- tillators.	126
7.4	Summary of radiation responses of the scintillators after ^{137}Cs gamma exposure up to 14 Mrad.	127

LIST OF FIGURES

Figure

2.1	The Standard Model of fundamental fermions (quarks and leptons) and bosons (gauge and Higgs)	7
3.1	A 3D map of the Large Hadron Collider (LHC)	10
3.2	CERN accelerator complex	13
3.3	LHC tunnel and the beam pipe	14
3.4	Total integrated luminosity at Compact Muon Solenoid (CMS)	15
3.5	The CMS detector in the cavity	16
3.6	A cartoon layout of the CMS detector	16
3.7	A transverse slice view of the CMS and particle flow in the detector . . .	17
3.8	Longitudinal view of a quadrant of the CMS and pseudorapidities, $\eta = 0.5 - 5.31$	17
3.9	Silicon strips in the CMS Tracker	18
3.10	A $PbWO_4$ crystal with a directly coupled vacuum phototriode (VPT) for ECAL calorimeter.	20
3.11	Hadronic Forward (HF) calorimeter wedges with quartz fibers stretching from absorber steel blocks	22
3.12	HF calorimeter image in the CMS cavity	22
3.13	A single muon detection in several layers of muon detectors	23
4.1	The Feynman diagram for resonance production of a heavy Majorana neutrino (N).	29
4.2	A 95% CL exclusion limit on $ V_{eN} ^2$ as a function of Majorana neutrino mass m_N set by CMS experiment	30

4.3	Next to leading order (NLO) cross section for resonance production of Majorana neutrinos as a function of m_N	31
4.4	Examples of tag-probe electron pair mass distributions for $Z \rightarrow ee$ events in data.	49
4.5	Electron efficiency results and data/MC scale factors are shown in four different η regions.	51
4.6	Kinematic distributions for low-mass region, $m_N < 80 \text{ GeV}/c^2$	56
4.7	Kinematic distributions for high-mass region, $m_N > 90 \text{ GeV}/c^2$	58
4.8	Exclusion upper limits on $ V_{eN} ^2$ with a 95% CL as a function of Majorana neutrino mass, m_N	60
4.9	Exclusion limits on branching fraction times cross section with a 95% CL as a function of Majorana neutrino mass, m_N	61
5.1	Feynman diagram of vector boson fusion Higgs production	63
5.2	Number of events reconstructed with and without PMT hits as a function of leading reconstructed jet p_T	65
5.3	Number of events versus MET with and without HF calorimeter and PMT hits.	67
5.4	Hamamatsu multianode R7600U-200-M4 PMTs and a metal package PMT	69
5.5	Muon response of HF R7525 PMTs in a 150 GeV muon test beam. . . .	70
5.6	Gain distributions of R7600U-200-M4 PMTs at various operating voltages	74
5.7	Dark current distributions of R7600U-200-M4 PMTs at various operating voltages	76
5.8	Timing distributions of R7600U-200-M4 PMTs at 800 V.	81
6.1	Circuit boards for powering R7761 and R5900-00-M16 PMTs.	87
6.2	Schematic diagram of the secondary emission baseboard common voltage divider for R7761 PMTs.	89

6.3	Schematic diagram of the secondary emission voltage divider for R5900-00-M16 PMTs.	90
6.4	The response uniformity of R5900-00-M16 PMTs	91
6.5	Gain distributions of R5900-00-M16 PMTs in different modes.	94
6.6	Gain distributions of R7761 PMTs in different modes.	95
7.1	Para-Terphenyl (pTp) evaporation (a) and Anthracene (AN) sputtering (b) on quartz plates	100
7.2	The intrinsic blue scintillation of PEN	101
7.3	Different geometries, sigma and bar shape grooved scintillators.	102
7.4	Scintillator transmission spectrum setup (a) and scintillation light yield setup (b).	104
7.5	PEN sample before irradiation in a vacuum bag.	105
7.6	Absorption spectrum (a), luminescence spectrum (b), and transmission spectrum (c) of the unirradiated and irradiated PEN samples.	106
7.7	Scintillation (light yield) spectrum of the unirradiated and irradiated PEN samples	107
7.8	Signal timing of PEN (a), PET (b) and Kuraray SCSN-81 HE Tile (c) .	109
7.9	Experimental setup for the light yield measurement.	110
7.10	PEN and PET light yield results over 50 days after irradiation.	112
7.11	PEN sample resting on Arduino-powered “radiation damage recovery” LED array.	114
7.12	Scintillation (light yield) spectrum of PEN samples for recovery from 13.73 Mrad gamma ray exposure.	115
7.13	Percent damage on various tiles after irradiation.	117
7.14	Light-tight 3D printed cases for tiles (a) and the experimental setup at CERN H2 Test Beam Area (b).	120

7.15	Response uniformity of PEN with different geometries	121
7.16	The MIP (muon) response of various tiles, tested at CERN H2 Test Beam Area	122
7.17	Experimental setup at Fermilab Test Beam Facility (FTBF).	123
7.18	Average scintillation waveform of various tiles	124
A.1	Exclusion upper limits on $ V_{\mu N} ^2$ with a 95% CL as a function of Majorana neutrino mass, m_N	133
A.2	Exclusion limits on cross section times branching fraction with a 95% CL as a function of Majorana neutrino mass, m_N	134
B.1	Exclusion upper limits on $ V_{eN}V_{\mu N}^* $ with a 95% CL as a function of Majorana neutrino mass, m_N	135
B.2	Exclusion limits on cross section times branching fraction with a 95% CL as a function of Majorana neutrino mass, m_N	136

CHAPTER 1 INTRODUCTION

In high energy and nuclear physics, experimental work depends on a skilled physics analysis and good detector hardware tools and applications. This thesis contains both software and hardware studies for the Compact Muon Solenoid (CMS) experiment [1] at Large Hadron Collider (LHC) at CERN [2] completed over the years of author's Ph.D. studies.

The primary goal of experimental particle physics is to explore undiscovered laws of nature and understand the building blocks of matter and energy. The question is which theoretical model(s) and experimental tools and machines are the most useful for exploring the mysteries of matter, energy, space and time.

The Standard Model (SM) is the best theory for understanding the nature of the universe. The SM provides a periodic table of matter's fundamental particles and the forces which act upon them. Most of the predictions made by the SM have been confirmed by various experimental results. However, there are still some deficiencies in the model, such as the hierarchy problem, the matter-antimatter asymmetry problem and neutrino oscillations. According to the SM, neutrinos are neutral and massless particles but the neutrino oscillation confirmation by cosmic, reactor and accelerator experiments have showed that neutrinos can be chargeless but not massless. More detailed information about the SM and neutrinos is presented in Chapter 2.

To test the predictions of the SM and beyond, very complicated particle accelerators and detectors have been used to explore how the universe came into being.

The most complex and powerful particle accelerator used in the world to date is Large Hadron Collider (LHC), which is the home of four main experiments; ALICE, ATLAS, CMS and LHCb. The LHC collides proton beam bunches at very close to the speed of light (pp collision), and the stream of particles resulting from the collision are detected by the main detectors and sub-detectors. The LHC will reach its design luminosity, $2 \times 10^{34} \text{ cm}^{-2} \text{ s}^{-1}$, and center of mass energy, 14 TeV during Run-3, which will start in 2021. The higher instantaneous luminosity and unprecedented radiation conditions necessitate a detector upgrade at the LHC so it will be shut down and upgraded over a twenty-year period. In Chapter 3, LHC and CMS collaboration are described with a detailed description of experimental apparatus of the CMS detector and sub-detectors. Also, this long-term upgrade period of the LHC and its objectives for physics are discussed in detail in this chapter.

Chapter 4 concentrates on the results of a search for heavy Majorana neutrinos using same sign dielectron ($e^{\pm}e^{\pm}$) + jets events. The data correspond to an integrated luminosity (L) of 19.7 fb^{-1} of proton-proton collisions at a center-of-mass energy (\sqrt{s}) of 8 TeV, collected with the CMS detector at the CERN LHC. There are several extensions of the SM, which predict the production of heavy Majorana neutrinos in pp collisions. The processes that violate lepton number conservation by two units are possible since they are their own antiparticle. The production of these particles at the LHC is considered in this analysis.

The description of the upgrade hardware studies is divided in three main sections. The first section reports the results of characterization studies of 1785 multi-

anode Hamamatsu R7600U-200-M4 photomultiplier tubes (PMTs) for CMS Hadronic Forward (HF) calorimeter. They replaced the previous single anode Hamamatsu R7525 PMTs of the HF calorimeter to increase the resolution of the calorimeter. These new multi-anode tubes were examined for numerous parameters such as gain, dark current, timing characteristics and response linearity. Chapter 5 describes the tests in more detail and the roles of the new multi-anode PMTs in the calorimeter.

The second section presents the results of characterization studies of photomultiplier tubes in a novel operation mode for Secondary Emission (SE) Ionization Calorimetry. SE Ionization Calorimetry is a novel technique to measure electromagnetic shower particles in extreme radiation environments. The different operation modes used in these tests were developed by modifying the conventional PMT bias circuit. Two kinds of PMTs have been characterized for use in a SE Ionization Calorimetry study, which are Hamamatsu single anode R7761 and multi-anode R5900-00-M16 PMTs. Chapter 6 reports the technical design of different operation modes, as well as the characterization measurements of both SE modes and the conventional PMT mode.

The third section of hardware studies, the last section of this thesis, concentrates on the results of a search for novel, radiation resistant, and high light yield scintillating materials for the upcoming CMS Hadronic Endcap (HE) calorimeter upgrade in specific and for other particle physics experiments in general. Various high light yield scintillators such as Polyethylene Naphthalate (PEN), Polyethylene Terephthalate (PET), High Efficiency Mirror (HEM) and quartz plates with vari-

ous coatings were studied. The coatings are applied as thin layers on the surface of the quartz plates and different organic and inorganic materials such as p-Terphenyl (pTp), Anthracene (AN) and Gallium-doped Zinc Oxide (ZnO:Ga) to increase the light output. The radiation hardness, light yield, timing characteristics, and emission and transmission properties of these materials have been investigated. In Chapter 7, the results of the laboratory measurements, related test beam activities and recent developments are discussed in detail.

The thesis finishes with the conclusions and discussions in Chapter 8.

CHAPTER 2 THEORETICAL BACKGROUND

2.1 The Standard Model

The Standard Model (SM) is a mathematical theory in particle physics, which explains the main particle interactions between the fundamental particles of the universe. The SM includes electromagnetic, strong and weak forces, but gravitational force since there isn't a quantum theory for it yet. In other words, the model has its limitations [3].

The model is a specific quantum field theory equation which represents matter particles (fermions) and force particles (bosons) and their interactions. There are nineteen physical constants in the equation. These constants need to be measured precisely from experimental data. In the SM, fermions are the particles with half-integer spin and they are characterized by Fermi-Dirac statistics. Quarks, leptons and most of the composite particles such as protons and neutrons¹ are fermions. Bosons, which are characterized by Bose-Einstein statistics, are force carriers with integer spin. There are elementary bosons such as gauge bosons ($\gamma, g, W^\pm, Z, graviton$)² and scalar Higgs (H) boson and composite particles such as mesons.

In Relativistic Quantum Mechanics (RQM), the static fields of forces do not exist. The interaction between two particles is transmitted by *intermediate particles*

¹Protons are made up of two up quarks and one down quark (uud) and neutrons are made up of two down quarks and one up quark (ddu).

²Graviton is an hypothetical particle that is a force carrier of Gravity.

acting as *interaction carriers*. The photon (γ) is the carrier of electromagnetic interactions, W^\pm and Z are responsible for weak interactions and gluons (g) are the carriers of the strong interaction.

Figure 2.1 shows the fundamental fermions and bosons³ including the recently discovered Higgs boson⁴ [4] [5]. Here, the letters on the top left corner refer to up (u), down (d), charm (c), strange (s), top (t) and bottom (b) quarks. The letters on the left bottom corner refer to charged leptons: electron (e), muon (μ) and tau (τ), and neutral leptons: electron neutrino (ν_e), muon neutrino (ν_μ) and tau neutrino (ν_τ). There is a corresponding neutrino flavor for each charged lepton. Many more composite particles with fancy names are made from combinations of fermions and studied at the particle physics experiments. They are so many to list them here, and for more information please check the particle data group's website [6].

2.2 Misfits of the Standard Model: Neutrinos

Neutrinos, one of the most abundant particles in the universe are created in certain type of nuclear reactions and radioactive decays [7–9]. They are weakly interacting particles that in every second, billions of them pass through our body without any harm. David Griffiths, a physicist at Reed College, describes neutrinos in his particle physics book [3]: “...neutrinos interact extraordinarily weakly with

³Antiparticles are not shown here; each particle has an identical antiparticle with opposite charge.

⁴It was observed by the ATLAS and CMS experiments in 2012. Peter W. Higgs and Francois Englert were awarded with the Nobel Prize in Physics in 2013 for their theoretical explanation of the Higgs mechanism.

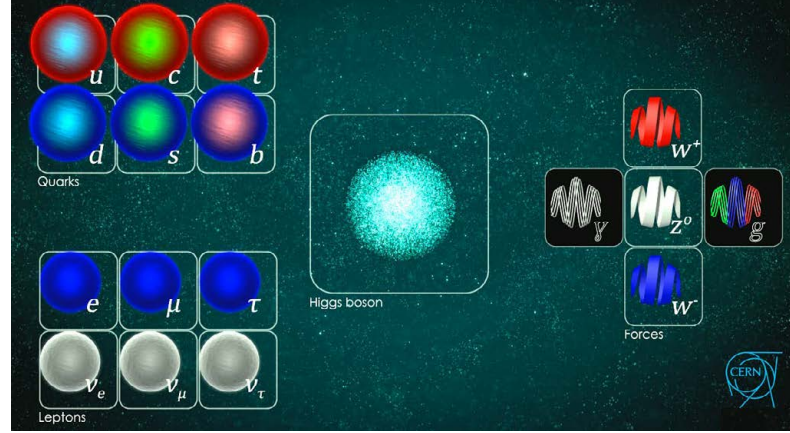


Figure 2.1: The Standard Model of fundamental fermions (quarks and leptons) and bosons (gauge and Higgs) (CERN, 2016).

matter; a neutrino of moderate energy could easily penetrate a thousand light years of lead. That’s a comforting realization when you learn that hundreds of billions of neutrinos per second pass through every square inch of your body, night and day, coming from the sun.”

Enrico Fermi reformulated Pauli’s idea of a light neutral particle involved in radioactive decays, and renamed it neutrino which means “little neutral one” in Italian (1934) [7]. His famous beta decay theory [10] proposed that an electron antineutrino ($\bar{\nu}_e$) is generated in the reaction, $n \rightarrow p + e^- + \bar{\nu}_e$. In this theory the electron and electron antineutrino are created as a pair. This theory of the neutrino was tested by observing the inverse reaction $p + \bar{\nu}_e \rightarrow n + e^+$ at reactor experiments. This inverse beta decay process was observed in a $\bar{\nu}_e$ scattering experiment at the Savannah River reactor in South Carolina in 1955 [11]. The observed and predicted cross section of the inverse beta decay process agreed; it was a milestone for the neutrino theory.

After the parity violation confirmation in the experiments of radioactive beta

decays of ^{60}Co [12] and the discovery of vector-axial vector (V-A) structure of weak interactions, which is chiral, neutrinos and antineutrinos were hypothesized as left-handed and right-handed particles, respectively. This was confirmed at Brookhaven National Laboratory (BNL) in 1958 [13].

Later in 1962, a group of scientists led by Leon Lederman, Melvin Schwartz and Jack Steinberger at BNL discovered the second member of the neutrino family, the muon neutrino (ν_μ) while studying pion decays ($\pi^+ \rightarrow \mu^+ + \nu_\mu$)⁵.

Then, the neutrino family was expanded with the discovery of tau neutrino, (ν_τ). The observation of ν_τ was announced in 2000 by DONUT detector collaboration at Fermilab [14]. Finally, all three neutrino flavors, ν_e , ν_μ and ν_τ were observed and each flavor has a corresponding antineutrino.

The idea of neutrino oscillations, which is a quantum mechanical phenomenon describes neutrino transitions from one flavor (type) to other was made by Bruno Pontecorvo in 1957 [15]. In 1962, theorists; Ziro Maki, Masami Nakagawa and Schoichi Sakata introduced a 2×2 matrix (MNS matrix) to represent the mixing of two neutrinos [16]. Later, the MNS matrix was extended to a 3×3 matrix to represent all three generations of neutrinos.

Since neutrinos are interacting weakly with other particles and matter, observation of the neutrino oscillations was an experimental challenge during the second half of the 20th century. The accelerator experiments set only the upper bounds on the oscillation probabilities of the flavor exchange over three decades until the late

⁵This discovery was rewarded with Nobel Prize in Physics in 1988.

1990s. Later, the neutrino oscillations were discovered by atmospheric in 1998 [17], solar in 2001 [18, 19], reactor in 2002 [20] and accelerator experiments in 2006 [21], respectively⁶. The discoveries confirmed that neutrinos can be chargeless but not massless.

However, neutrinos are neutral and massless particles according to the Standard Model (SM), which is currently the best theory for understanding the nature of the universe. As a result, the existence of neutrino oscillations require new physics *beyond the Standard Model* (BSM) and that opens doors to more questions about the neutrinos. The neutrino mass is the first evidence of physics beyond the SM. Various extensions of the SM address non-zero neutrino mass.

The discovery of neutrino masses would be another milestone in particle physics, as important as the Higgs boson discovery at the LHC [4] [5].

⁶Recently, Prof. Takaaki Kajita and Prof. Arthur B. McDonald, leading two teams, respectively Super-Kamiokande in Japan and Sudbury Neutrino Observatory in Canada were awarded with 2015 Nobel Physics Prize for their contributions to the discovery of neutrino oscillations.

CHAPTER 3

LHC AND CMS EXPERIMENTAL APPARATUS

3.1 Large Hadron Collider

The Large Hadron Collider (LHC) is presently the world's biggest and most energetic particle accelerator. It is located in a large circular tunnel at European Organization for Nuclear Research (CERN) in Geneva at the Swiss-French border. Figure 3.1 shows the LHC tunnel with a circumference of twenty-seven kilometers and about one hundred meters beneath the surface at its greatest depth. The LHC provides collisions of two groups of high-energy particles at a speed very close to the speed of light ($0.999999990\ c$) such as protons (pp collisions) and lead ions (lead-lead collisions). The LHC enables scientists to study a broad range of physics and explore the universe from the tiniest of subatomic particles to the highest energies [2].

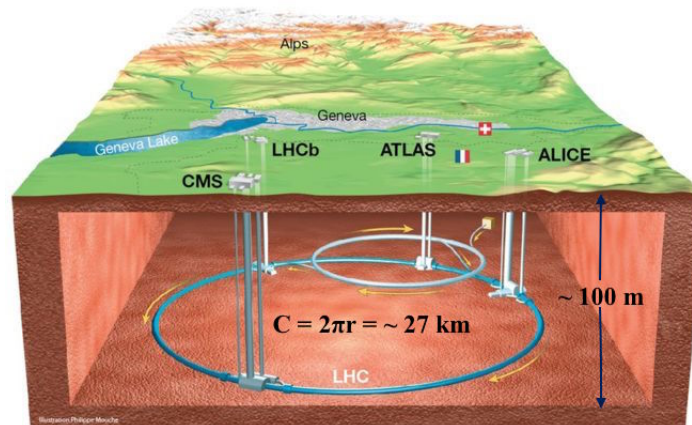


Figure 3.1: A 3D map of the Large Hadron Collider (LHC) (CERN, 2016).

Some of the main physics purposes of the LHC can be listed as:

- to find the origin of mass, the Higgs boson,
- to look for unification, Supersymmetry (SUSY) and other candidates for dark energy and dark matter,
- to investigate the mystery of anti-matter disappearance in the universe,
- to understand physics at the early stage of the universe, heavy ion collisions and quark-gluon (qg) stages.

At the LHC, there are four main experiments and each of them consists of a large array of detectors located at four separate collision halls under the ground. Each experiment is designed for a distinctive purpose. Two of them, Compact Muon Solenoid (CMS) and A Toroidal LHC ApparatuS (ATLAS) are general-purpose detectors. The other two, A Large Ion Collider Experiment (ALICE) and Large Hadron Collider beauty (LHC-b) are specific purpose detectors. The pp collisions occur in the center of each detector and the generated particles are detected by each experiment for further analysis.

Currently, CERN is running the most advanced accelerators by using the most powerful electromagnetic devices and dipole magnets (superconducting electromagnets). Dipole magnets steer the charged particles in circular orbits and electromagnetic resonators accelerate particles and keep them at a constant energy. LHC, the main accelerator at CERN, as seen in Fig. 3.2, has 9,600 magnets to steer beams of protons and lead ions. The magnets are cooled to 1.9 Kelvin ($-271.25\text{ }^{\circ}\text{C}$ and -456.25

F°), which is colder than the vacuum of outer space. These dipole magnets at the LHC provide up to 8.3 T over their length.

The LHC is not the only accelerator at CERN, but the biggest one. The other accelerators are used to boost the speed of protons (lead ions) step by step. All these accelerators can be seen as circles in Fig. 3.2. The protons at LHC are made by stripping electrons from hydrogen atoms and then are fed to the Booster from the Linear Accelerator (LINAC). The booster accelerates them up to 1.4 GeV and feeds them into the Proton Synchrotron (PS). PS accelerates them up to 25 GeV and feeds them into the Super Proton Synchrotron (SPS). SPS accelerates proton bunches up to 450 GeV and they are fed to the LHC in both clockwise and counterclockwise directions to accelerate each of them up to 7 TeV and they are collided at their maximum speed.

The LHC is also accelerating lead ions, which are produced from a purified lead sample and fed into LHC by passing similar steps as protons. Each lead ion bunch is accelerated up to 2.76 TeV in the LHC ring and collided. Before the lead ion bunches are fed into the LHC ring, they are accelerated up to a certain speed by Low Energy Ion Ring (LEIR), PS and SPS, respectively. The path of the lead ion bunches can also be seen in Fig. 3.2. Since the scope of this study is limited to pp collisions, no further details are given for lead-lead collisions.

Figure 3.3 shows the LHC tunnel with vacuum vessel, iron yoke, superconduction coils, liquid helium line and the beam pipe.

The LHC is allowing scientists to study wide range of physical processes by

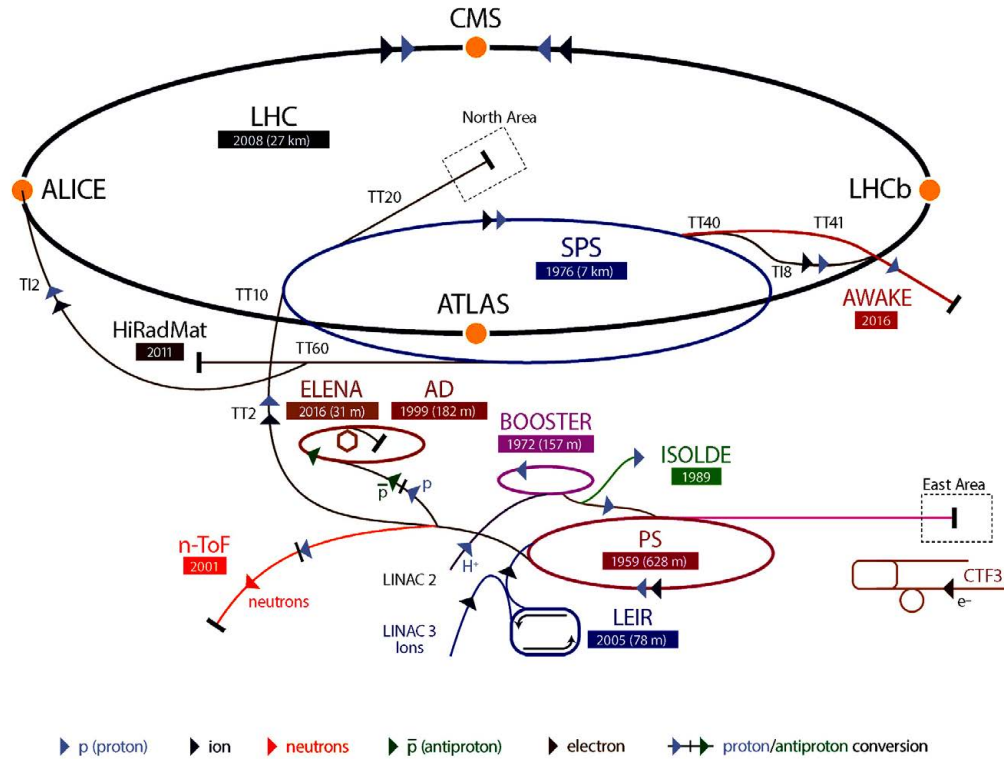


Figure 3.2: CERN accelerator complex (CERN, 2016).

smashing the protons and lead ions in those collision halls at unprecedented center of mass energy and luminosity¹ (L), which gives a measure of how many collisions occur per square centimeter per second.

The LHC operation center of mass energy was 7 TeV in 2011 and 8 TeV in 2012. The total integrated luminosity respectively is 5.55 fb^{-1} and 21.79 fb^{-1} . Figure 3.4 shows the total integrated luminosity recorded by CMS in 2011 and 2012 [22].

¹At LHC in 2010, there was a few million proton collisions per second occurred but in the near future with the upgrades, this number is expected to be around 600 million proton collisions per second.

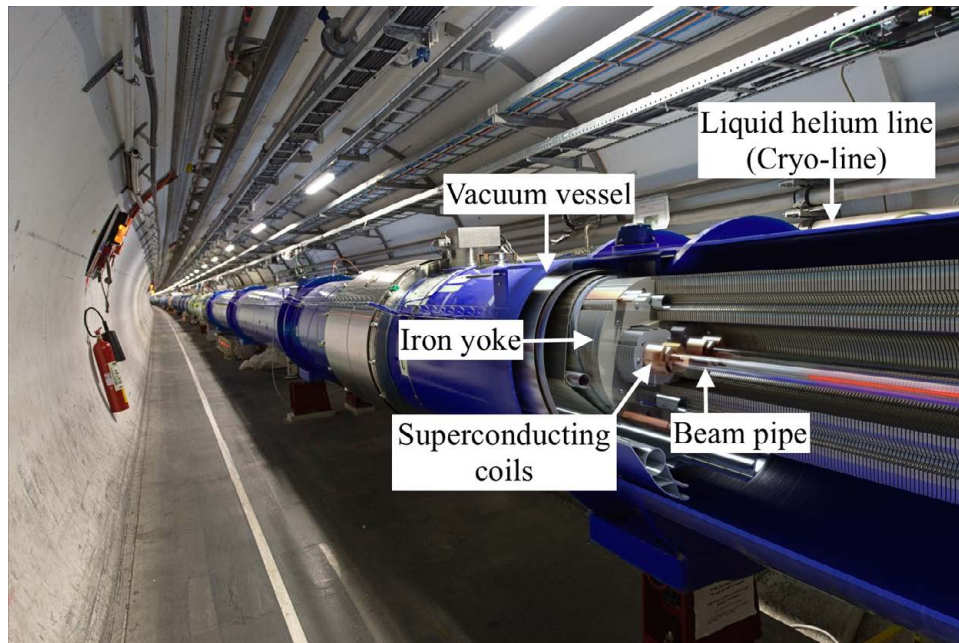


Figure 3.3: LHC tunnel and the beam pipe (CERN, 2016).

3.2 Compact Muon Solenoid (CMS)

CMS is one of the two general-purpose detectors [1] at CERN, which means that it was designed to observe all possible decay products from a pp collision. It is weighing in at 12,500 tons, standing 15 meters and stretching 22 meters long, as shown in Fig. 3.5.

CMS detector works like a huge camera, recording the events of decay particles from pp and lead-lead collisions. It is aimed to measure the positions and energies of hadrons, gammas, leptons and jets produced by pp collisions at very high energies. CMS detector consists of a tracker, an electromagnetic calorimeter (ECAL), a hadronic calorimeter (HCAL), a solenoid magnet and muon detectors inside a return yoke.

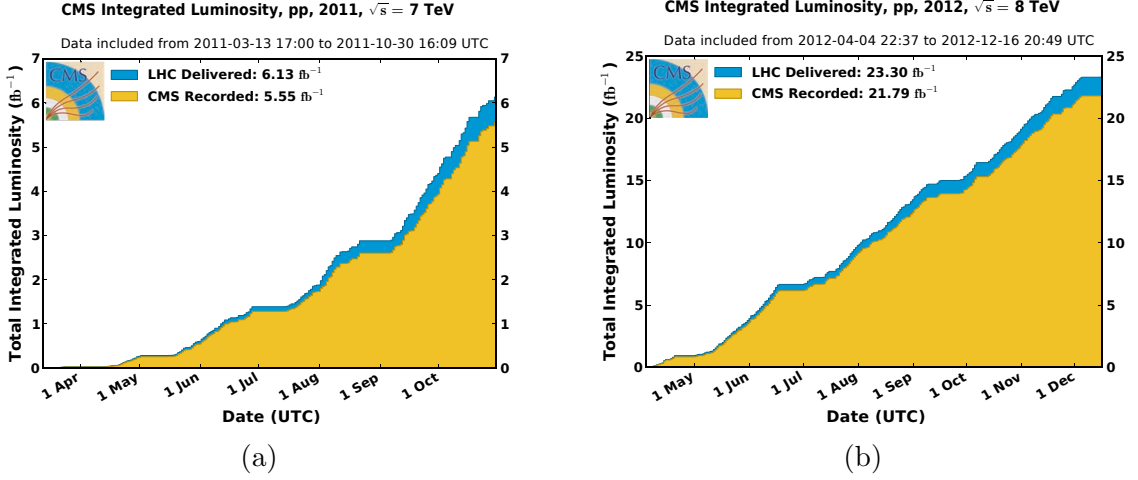


Figure 3.4: Total integrated luminosity at Compact Muon Solenoid (CMS) in 2011 (a) and 2012 (b) (CMS, 2016)

The overall layout and a transverse slice of the CMS are shown in Fig. 3.6 and Fig. 3.7. The magnetic field (\vec{B}) inside the CMS is $\sim 4 \text{ T}$ and it is a hermetic, 4π detector covering all the directions around the interaction point. The coordinate system in the CMS defined as follows: x -axis points towards the center of the LHC ring, y -axis points vertically upward from the interaction point and z -axis is parallel to the beam direction. The *polar angle*, θ is defined in the rz plane, and the *azimuthal angle*, ϕ is measured from the x -axis in the xy plane and r , which is the radial coordinate in this plane. The *pseudorapidity*, η is defined as $\eta = -\ln[\tan(\theta/2)]$. The transverse energy of the decay particles is defined as $E_T = E \sin\theta$ and the transverse momentum, p_T of the decay particles is calculated from the x and y components of their momentum.

Figure 3.8 shows a longitudinal view of a quadrant of the CMS including

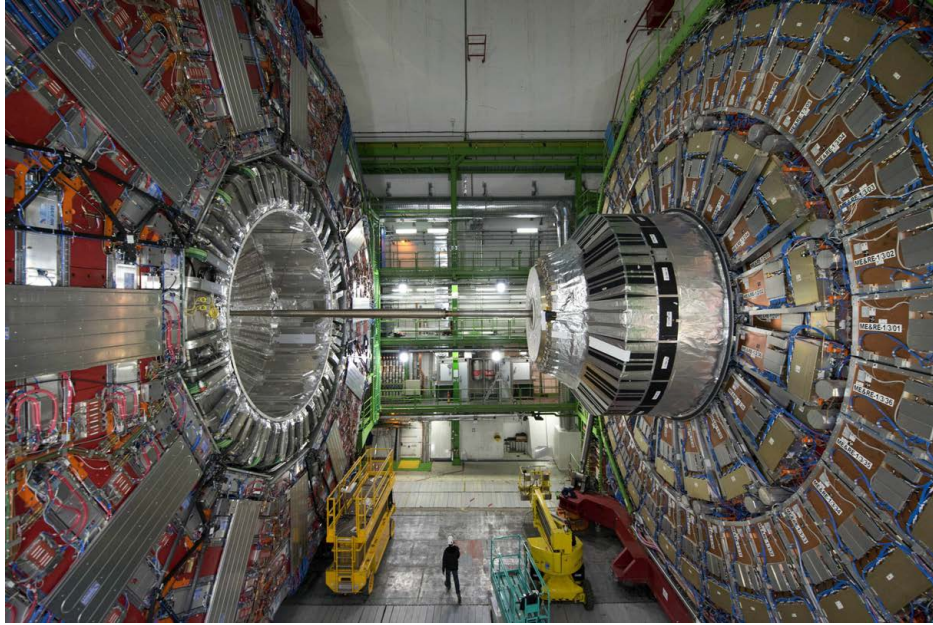


Figure 3.5: The CMS detector in the cavity (CERN, 2016).

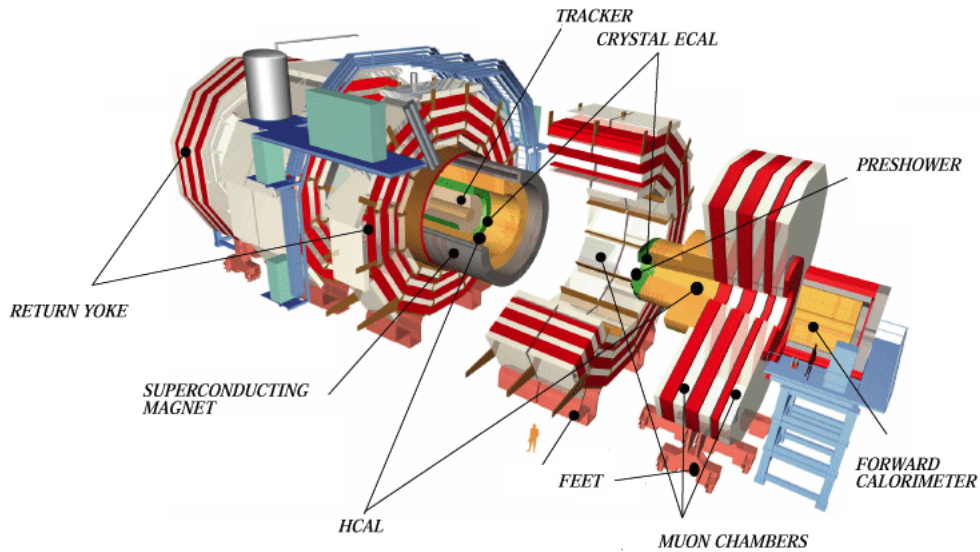


Figure 3.6: A cartoon layout of the CMS detector (CERN, 2016).

subdetectors and calculated pseudorapidities, η between 0.5 and 5.31. LHC and CMS public websites [1, 2] and technical design reports [23] would be helpful for detailed

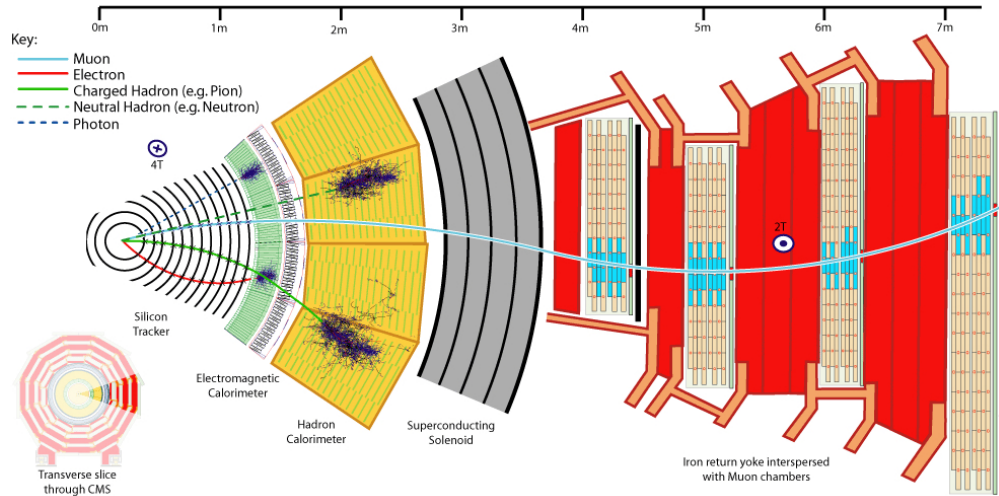


Figure 3.7: A transverse slice view of the CMS and particle flow in the detector (CERN, 2016).

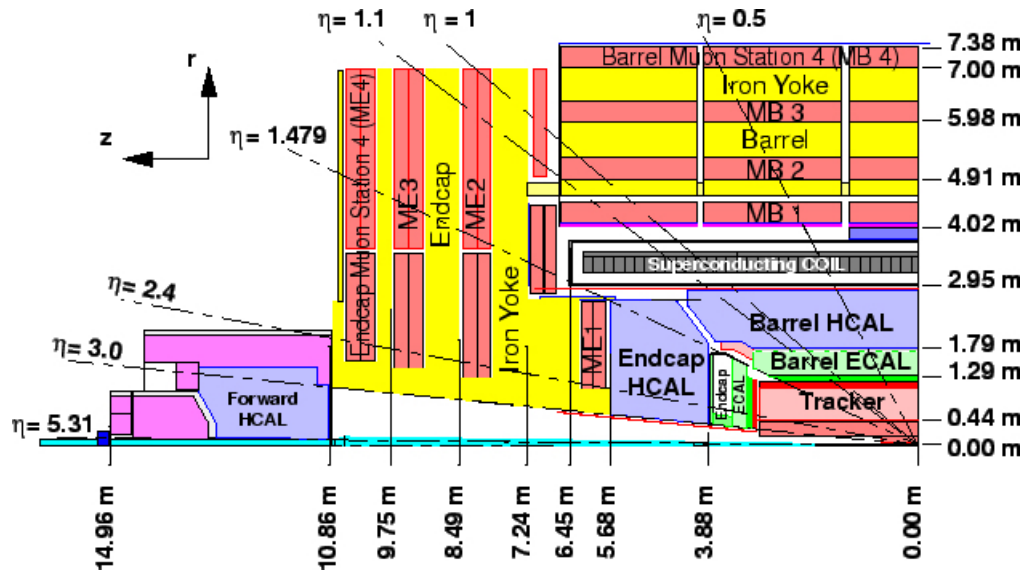


Figure 3.8: Longitudinal view of a quadrant of the CMS and pseudorapidities, $\eta = 0.5 - 5.31$ (CERN, 2016).

information about the CMS detector and the LHC program.

3.2.1 The Tracker

The particle tracker reconstructs charged particles by taking position measurements of them in a magnetic field. The charged particles are curved when they enter into a magnetic field and their curvature paths provide information about their identity. For instance, particles with less momentum have a more curved path so they have a smaller radius of curvature than higher momentum particles.

Since the tracker is so close to the interaction point, and exposed to high-flux of particles, each component should be radiation resistant. In this regard, radiation resistant silicon pixels and silicon microstrip detectors form the tracker at CMS, Fig. 3.9. [24]. It consists of three main sections, barrel, disk and endcap. The barrel has three pixel and ten strip layers and the disk and endcap have two pixel and twelve strip layers.

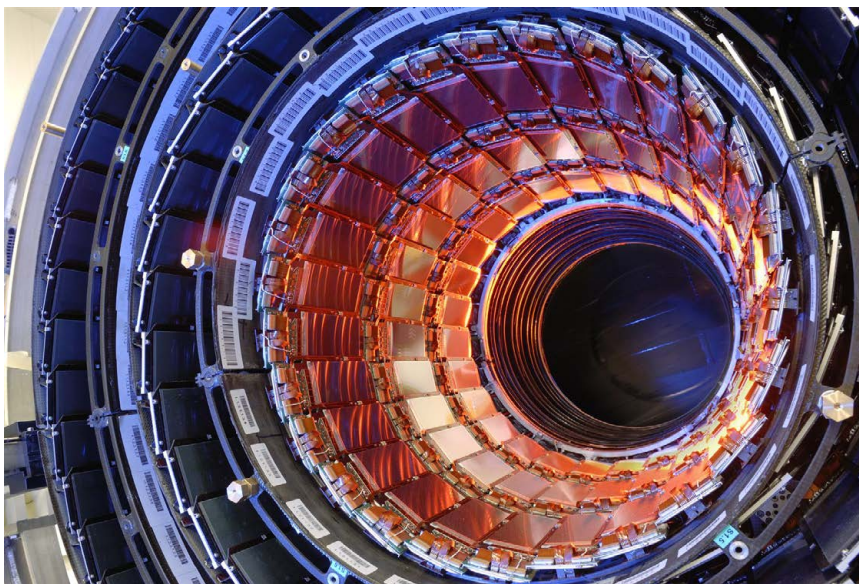


Figure 3.9: Silicon strips in the CMS Tracker (CERN, 2016).

The particle hits are recorded by these silicon strips and microstrips and the track reconstruction starts from the innermost layer and continues until the full track is found in a radial direction. More detailed information about the track reconstruction and the technical design of the tracker can be found in the TDR [25].

3.2.2 Electromagnetic Calorimeter

Electromagnetic Calorimeter (ECAL) is crystal calorimeter and consists of a cylindrical barrel (EB) and two flat endcap (EE) sections [26]. The main purpose of the ECAL is to precisely measure the energy of electrons and photons. The active material of the ECAL is lead tungstate ($PbWO_4$) crystals, which scintillate when electrons and photons pass through them. The scintillation light from the crystals in EB and EE is read out by avalanche photodiodes (APDs) and vacuum phototriodes (VPTs), respectively. APDs are not radiation resistant enough to be used in the endcap regions. The EB consists of 61,200 crystals in a size of $2.2 \times 2.2 \times 23 \text{ cm}^3$ and EE sections have a total of 15,000 crystals in a size of $3 \times 3 \times 22 \text{ cm}^3$. Figure 3.10 shows one of these crystals with a direct coupled VPT and a shower simulation due to photons and electrons.

There is also a preshower detector, which is made of lead planes and silicon sensors, sits just in front of the ECAL to distinguish for high-energy photons from the Higgs boson decay and lower-energy photons from short-lived particles such as neutral pions.

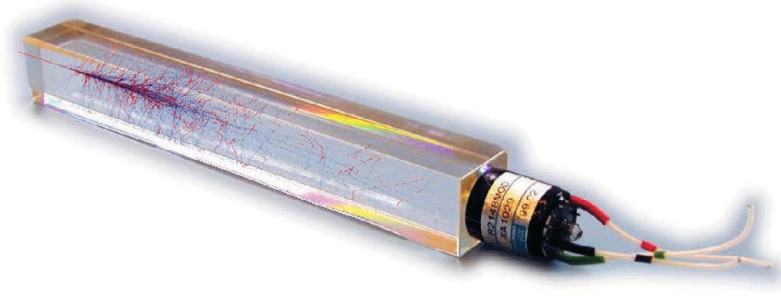


Figure 3.10: A $PbWO_4$ crystal with a directly coupled vacuum phototriode (VPT) for ECAL calorimeter. The figure shows the shower simulation due to photons and electrons (CERN, 2016).

3.2.3 Hadronic Calorimeter

The Hadronic Calorimeter (HCAL) is a central, brass-scintillator sampling calorimeter at CMS [27]. It provides coverage up to $\eta = 3$. The main purpose of the HCAL is to find the energy, position and arrival time of the hadrons, which are the particles made of quarks such as pions and protons. It consists of alternating layers of absorbers and scintillators. Absorbers are basically used to slow down hadronic particles and scintillators are used to generate photons in proportion to the energies of the particles traversing them. These photons are collected by wavelength shifting fibers (WLS), which are then read out by photodetectors. These photodetectors transform the signal into a voltage signal and the calibration factors are applied offline to reconstruct the particles energy and position.

The HCAL consists of four main sections, hadronic barrel (HB) and hadronic outer (HO) in $\eta < 1.3$, hadronic endcap (HE) in $1.3 < \eta < 3$ and hadronic forward (HF) calorimeter $3 < \eta < 5$. HB and HE calorimeters are using the same materials;

brass is used as absorbers and plastic scintillators (SCSN-81, known as HE scintillator) as scintillator materials. The photodetectors are hybrid photodiodes (HPDs) and the light channeled through clear fibers from WLS (Kuraray Y11) to the face of the HPDs to get the light out of the radiation zone. The HE calorimeter has 10 interaction length (19 active layers). HO is the outer barrel and used as a tail catcher in the barrel region.

The HF calorimeter of the HCAL is located in $3 < \eta < 5$ corresponding to polar angle range $0.78^\circ < \theta < 5.70^\circ$ with respect to the beam direction. There are two HF calorimeters (HF+ and HF-) mounted at each end of the CMS detector and located at about 11 m from the interaction point.

3.2.4 Hadronic Forward Calorimeter (HF)

Each HF calorimeter is composed of quartz fibers (Long fibers, L=1.65 m and Short fibers, S=1.43 m) embedded in a radiation-hard steel absorber². There are a total of 18 steel absorber wedges and 864 towers in the two HF modules. Each tower is read out by two photomultiplier tubes (PMT); one is coupled to S fibers, another to L fibers, Fig. 3.11. As can be seen in the Fig. 3.12, the structure of the HF with 72 readout boxes (RBX) host a total of 1728 PMTs in the two HF calorimeters. Each quadrant of a HF calorimeter has nine RBXs that includes 216 PMTs.

The main purposes of the HF is improving the measurement of the missing transverse energy (MET) and identifying high energy jets from the pp collisions.

²In this region, the total of ten years accumulated radiation is ~ 1 Grad.

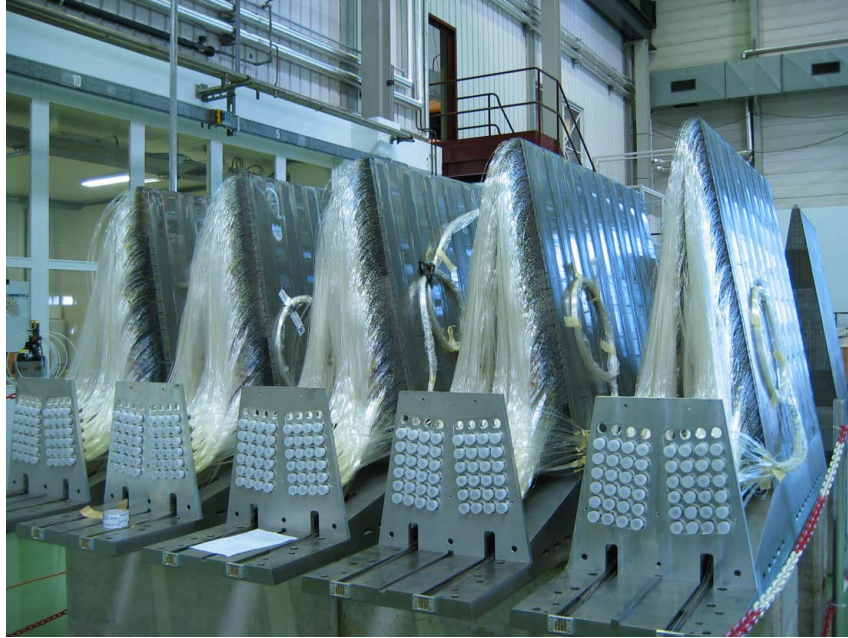
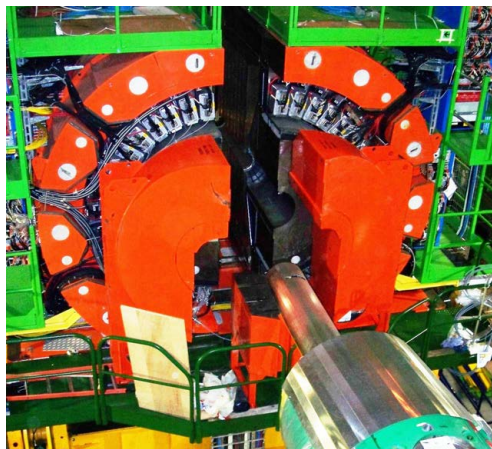
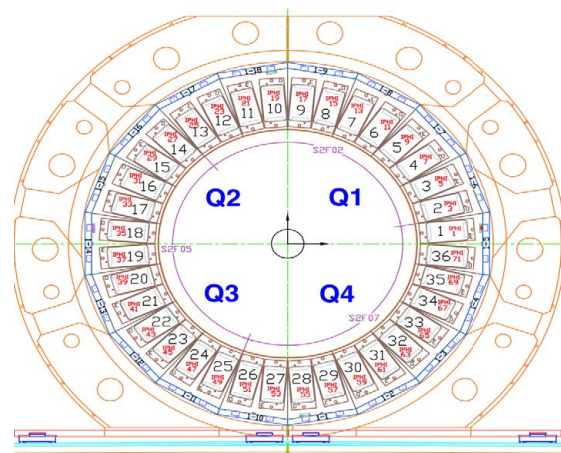


Figure 3.11: Hadronic Forward (HF) calorimeter wedges with quartz fibers stretching from absorber steel blocks (CERN, 2016).



(a)



(b)

Figure 3.12: HF calorimeter image in the CMS cavity (a) and the back view of HF with tower structure (b) (CERN, 2016).

3.2.5 Muon System

Muons are minimum ionizing particles (MIP), which means that they can penetrate through even several meters of iron without interacting. As the name of

“Compact Muon Solenoid” implies, detecting muons is an important task for CMS experiment. The magnets in the central barrel of the CMS detector bend the paths of these charged particles and they are detected in the muon chambers, at the outer edge of the detector. Figure 3.13 shows a single muon coming from the interaction point is detected in four layer of muon detectors.

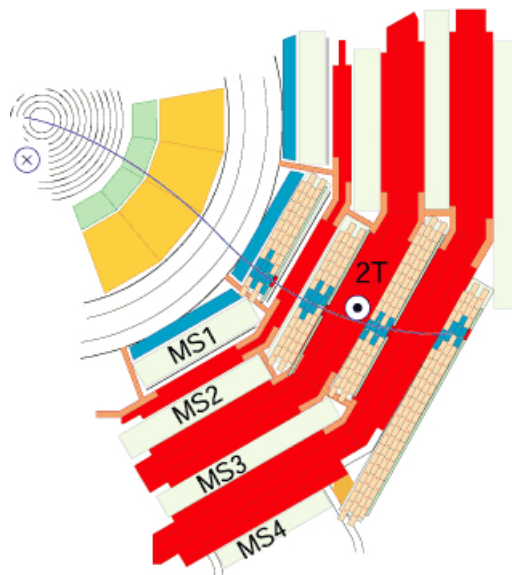


Figure 3.13: A single muon detection in several layers of muon detectors (CERN, 2016).

There are a total of 1400 high muon chambers are used CMS, which consists of 250 drift tubes (DTs), 540 cathode strip chambers (CSCs) and 610 plate chambers (RPCs). DTs and CSCs track the positions of the particles and provide muon trigger while RPCs work as a pilot trigger system to decide to keep a muon’s data or reject it [28].

3.3 LHC Shutdowns and CMS Detector Upgrades

The designed luminosity (L) is $10^{34} \text{ cm}^{-2} \text{ s}^{-1}$ and the center of mass energy is 14 TeV at the LHC. To reach its designed luminosity and center of mass energy, the LHC needs to be shut down and upgraded over a twenty-year period [29]. This long-term upgrade period is divided into two parts, Phase I and II. These two phases will be discussed in the next subsection but a detailed information can be found in Technical Proposals (TPs) [30,31]. During the Phase I and Phase II, not only CMS is upgraded but also ATLAS, LHC-b and ALICE. However, the scope of our study is limited to CMS upgrade only. The goal with the upgraded CMS detector is optimizing the CMS performance and maximize the physics output. After the upgrade, the detector will be ready to fully probe TeV scale physics processes as listed:

- Electroweak symmetry breaking.
- Higgs phenomenon.
- Supersymmetry.
- Beyond the Standard Model (BSM) physics.
- Extra dimensions of space and time.

3.3.1 Phase I

There are two long-term shutdown periods under Phase I, called *LS1* and *LS2*. *LS1* was successfully undergone in 2012-2015. The center of mass energy (collision energy) at the LHC was 7 TeV in 2011 and 8 TeV in 2012, and these runs are called Run 1. After the *LS1* upgrade, the LHC was started to operate again at 13 TeV in

2015 and it's expected to reach up to 14 TeV by the end of 2016. This data taking period is called Run 2. Then it will be shut down again for *LS2* upgrade in 2017 and *LS2* is expected to end by the next operation schedule in 2018. After then, operation will resume with the luminosity rising gradually up to $2 \times 10^{34} \text{ cm}^{-2} \text{ s}^{-1}$.

What are the goals to be accomplished with the upgrades during *LS1* and *LS2*?

- (a) During *LS1*, some detector parts were upgraded, electronics were replaced, muon trigger system was improved and magnet splices were repaired to reach the designed center-of-mass energy of 14 TeV.
- (b) During *LS2*, the pixel detector and the beam pipe will be replaced and trigger system will be improved to reach two times the designed luminosity, $2 \times 10^{34} \text{ cm}^{-2} \text{ s}^{-1}$.

During *LS1*, HF calorimeter at HCAL was upgraded to deal with larger beam currents and higher center-of-mass energy collisions expected in the LHC during Run 2. The High Energy Physics (HEP) group at the University of Iowa (UI) was responsible for characterization and installation of 1728 multi-anode photo-multiplier tubes (PMT), testing of readout boxes and light guide systems and the replacement of the front-end electronics. We also participated in simulation studies to understand the expected performance of the upgraded HF. Chapter 5 provides more information about the characterization studies of the PMTs and the other upgrade studies for HF calorimeter. Also, more detailed information about the Phase I upgrade can be found in the TP [30].

3.3.2 Phase II

There will be one foreseen long-term shutdown after 2020, *LS3*. It will be a major machine upgrade to be able to reach ten times the designed luminosity, $10 \times 10^{34} \text{ cm}^{-2} \text{ s}^{-1}$. This will be a major transformation to handle the highest luminosity will be achieved in particle colliders. After the *LS3*, the LHC will start its high luminosity (HL) era, and that is referred as HL-LHC.

During *LS3*, the tracking detector, HCAL Endcap (HE) calorimeter and ECAL barrel electronics will be replaced. Many changes are also planned for sub-detectors. The LHC is aimed to produce many more particles with the upgrade. To precisely measure the events of the interesting collisions, data acquisition (DAQ) systems and the trigger systems will be upgraded.

The LHC will be running for many years by 2020 and the degradation of the detector parts due to the integrated radiation dose needs to be addressed. Simulation studies and laboratory tests have been done by many CMS collaborators to estimate the upgrade work needs to be done. More detailed information about the results of those studies and the technical design of the new systems can be found in the TP [31].

CHAPTER 4 MAJORANA NEUTRINO SEARCH

4.1 Introduction

As detailed in Chapter 2.2, the discovery of neutrino oscillations¹ [32, 33], a quantum mechanical phenomenon describes neutrino transitions from one flavor (type) to another, at cosmic, reactor and accelerator neutrino experiments implies that at least two of the observed neutrinos have tiny non-zero mass. Since the neutrinos in the SM are massless, the existence of neutrino oscillations require new physics *beyond the Standard Model* (BSM) and it opens doors to more questions about the neutrinos.

The neutrino mass is the first evidence beyond the SM for which various extensions of the SM have been theorized. The most common model generating light neutrinos is so-called “SeeSaw” mechanism [34–42]. The simplest seesaw is the Type-I seesaw in which heavy, right handed neutrino singlets (N) can be added to the SM Lagrangian. It produces a new heavy state (Majorana mass neutrino) and a corresponding a light neutrino for each flavor. The mass eigenvalues for the light neutrinos are given by Eq. 4.1 below; where m_ν is the SM light neutrino mass, m_N is the Majorana mass of the right-handed neutrino (N), y_ν is a Yukawa coupling, ν is the Higgs vacuum expectation value, and m_D is the Dirac mass. Here, both the light

¹Recently, Prof. Takaaki Kajita and Prof. Arthur B. McDonald, leading two teams, respectively Super-Kamiokande in Japan and Sudbury Neutrino Observatory in Canada were awarded with 2015 Nobel Physics Prize for their contributions to the discovery of neutrino oscillations.

and heavy neutrinos would be Majorana particles and it implies that processes that violate lepton number conservation (LNC) by two units would be possible.

$$m_\nu = \frac{y_\nu^2 \nu^2}{m_N} \text{ and } y_\nu^2 \nu^2 \sim m_D^2 \quad (4.1)$$

The extension models of the SM for neutrino mass can be tested by searching for these new predicted particles. From this perspective, this thesis concentrates on the search for the resonance production of a heavy neutrino, Fig. 4.1, at the LHC using CMS detector. Searches for heavy Majorana neutrinos at hadron colliders have been considered by many authors [43–47] and we follow the studies in Refs. [48–50]. These studies estimated the sensitivity for resonant production of a Majorana neutrino in the mass range of 10-400 GeV at the LHC, which is corresponding to the expected light neutrino masses in the eV range.

As can be seen in Fig. 4.1, the final state can be any dileptons: $e^\pm e^\pm$, $\mu^\pm \mu^\pm$, $\tau^\pm \tau^\pm$, also $\mu^\pm e^\pm$ and $e^\pm \mu^\pm$ are possible. Here, this process violates the LNC by two units.

Here, we present a search for heavy Majorana neutrino in the same-sign (like-sign) dielectron ($e^\pm e^\pm$) channel using 19.7 fb^{-1} of data from 8 TeV collisions, which was collected with the CMS detector at LHC in 2012 [51–53]. We search for two isolated (prompt) electrons and we require at least two accompanying jets. The CMS results of Majorana neutrino search in $\mu^\pm \mu^\pm$ and $e^\pm \mu^\pm$ channels² for the same dataset

²The author’s primary focus was the dielectron ($e^\pm e^\pm$) channel but contributed to dimuon ($\mu^\pm \mu^\pm$) and e-mu ($e^\pm \mu^\pm$, $\mu^\pm e^\pm$) channel analysis as well. The physics analysis of all three channels were done by CMS Exotica Heavy Majorana Neutrino Search Group

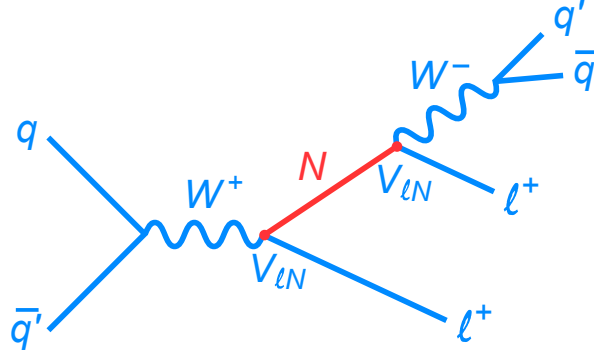


Figure 4.1: The Feynman diagram for resonance production of a heavy Majorana neutrino (N). The charge conjugate diagram results in a $l^-l^-q\bar{q}$.

can be found in the Appendix A and B.

Direct search limits on heavy Majorana neutrino mixing element squared, $|V_{lN}|^2$ ($l = e, \mu, \tau$) were set previously by L3 [54] and DELPHI [55] experiments at LEP. Here, V_{eN} is the mixing element of the heavy Majorana neutrino with the SM ν_e , the limits were set for $m_N < 200$ GeV by the LEP experiments.

The CMS and ATLAS collaborations at the LHC also reported limits on heavy Majorana neutrino production at LHC. The CMS collaboration set limits on $|V_{lN}|^2$ for $l = e$ and $l = \mu$ with the data corresponding to an integrated luminosity of 4.98 fb^{-1} of pp collisions at a center of mass energy of 7 TeV, collected by CMS detector in 2011 [56]. Figure 4.2 shows the limits set by CMS experiment on $|V_{eN}|^2$ as a function of Majorana neutrino mass m_N , and also upper limits from DELPHI and L3 experiments. The ATLAS collaboration set limits on $|V_{\mu N}|^2$ and on cross section

under the supervisions of Prof. John Ellison from the University of California, Riverside and Prof. Un-Ki Yang from Seoul National University and the author is a member of the group with many others.

times branching fraction, $\sigma(pp \rightarrow N\mu^\pm \rightarrow \mu^\pm\mu^\pm q\bar{q}')$ as a function of m_N with the data correspond to 4.7 fb^{-1} of pp collisions at 7 TeV, collected by ATLAS detector in 2011 [57, 58].

The CMS collaboration previously searched for heavy Majorana neutrinos up to $m_N = 200 \text{ GeV}$ at $\sqrt{s}=7 \text{ TeV}$. This study is an updated search for heavy Majorana neutrino with mass up to 500 GeV in the dielectron channel.

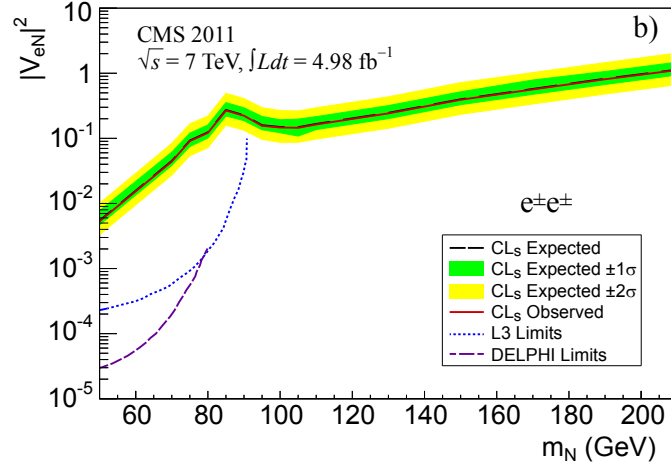


Figure 4.2: A 95% CL exclusion limit on $|V_{eN}|^2$ as a function of Majorana neutrino mass m_N set by CMS experiment [56].

Figure 4.3 shows the cross section results from del Aguila et al. [50] for heavy Majorana neutrino production via the process in Fig. 4.1 as a function of m_N for $|V_{eN}|^2 = 1$.

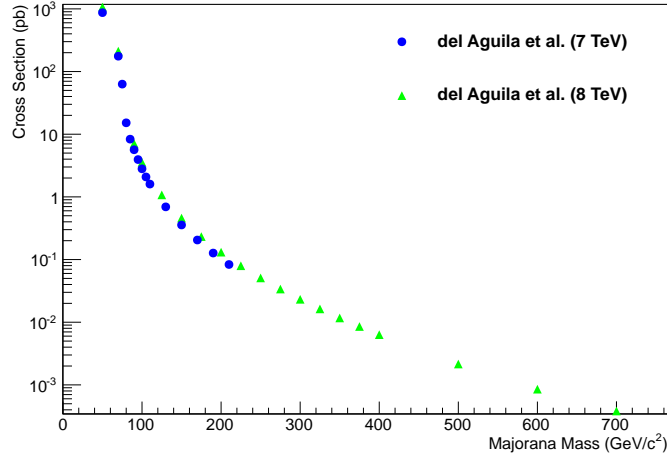


Figure 4.3: Next to leading order (NLO) cross section for resonance production of Majorana neutrinos as a function of m_N .

4.2 Datasets and Monte Carlo Event Samples

4.2.1 2012 Collision Data

The full dataset collected by CMS detector in 2012, Run2012A-Run2012D datasets are used for this analysis as listed in Table 4.1. The corresponding total integrated luminosity is $19.7 \pm 0.5 \text{ fb}^{-1}$.

Table 4.1: Summary of the 2012 complete datasets used for Majorana neutrino search in $e^\pm e^\pm + \text{jets}$ events.

Dataset	Run Range
/DoubleElectron/Run2012A-22Jan2013-v1/AOD	190456 – 193621
/DoubleElectron/Run2012B-22Jan2013-v1/AOD	193833 – 196531
/DoubleElectron/Run2012C-22Jan2013-v1/AOD	198022 – 203742
/DoubleElectron/Run2012D-22Jan2013-v1/AOD	203777 – 208686

4.2.2 Monte Carlo Signal Generation for Majorana Neutrino

The heavy Majorana neutrino production and decay process, Fig. 4.1, is simulated using the leading order (LO) event generator described in Ref. [50] and implemented in ALPGEN v2.14 with the CTEQ6M parton distribution functions (PDFs). The output of the ALPGEN generator was stored in the Les Houches 1.0 file format [59]. The datasets were unweighted using PYTHIA v6.4.22 version [60] to generate events for each neutrino mass. Then, the generated event files were interfaced with CMS Software, CMSSW (version, 5_3_12_patch2) with which parton showering, vertex smearing, GEANT4 [61] detector simulation, digitization of simulated electronics signal, and reconstruction were performed. All the signal samples were reweighted for proper simulation of the number of interactions per crossing.

We have generated thirteen samples for dielectron ($e^\pm e^\pm$) channel as a function of m_N , ranging from 40 to 500 GeV/c^2 . Table 4.2 summarizes all the produced Monte Carlo signal samples and the LO cross section values of the samples while $|V_{eN}|^2 = 1$. Table 4.3 shows the list of abbreviations used in Table 4.2. Here, the cross section is proportional to $|V_{eN}|^2$. As can be seen in Table 4.2, the LO cross section at center of mass energy of $\sqrt{s} = 8$ TeV for $pp \rightarrow Ne^\pm \rightarrow e^\pm e^\pm q\bar{q}'$ with $|V_{eN}|^2 = 1$ is 1515 pb for $m_N = 40$ GeV/c^2 and it drops to 2150×10^{-6} pb (2.15 fb) for $m_N = 500$ GeV/c^2 .

A scaling factor (k-factor) of 1.34 was applied to LO cross sections to account for higher order corrections, based on the next-to-next-to-leading-order (NNLO) calculations for W' in FEWZ [62, 63].

Table 4.2: Summary of Majorana neutrino signal Monte Carlo samples. The calculated LO cross sections, while $|V_{eN}|^2 = 1$ (without k-factor scaling) are shown as a function of m_N . The abbreviations are listed in Table 4.3.

Mass (GeV/c^2)	Dataset Name	σ (pb)	$\int \mathcal{L} dt$ (pb^{-1})
40	/MNTtoEE_M-40_TZ8_alp/S12a	1515 ± 1	65.6
50	/MNTtoEE_M-50_TZ8_alp/S12	1071 ± 1.4	46.68
60	/MNTtoEE_M-60_TZ8_alp/S12a	607.6 ± 0.4	163.7
70	/MNTtoEE_M-70_TZ8_alp/S12	212.0 ± 0.3	235.9
80	/MNTtoEE_M-80_TZ8_alp/S12a	19.06 ± 0.01	5165
90	/MNTtoEE_M-90_TZ8_alp/S12	$(7105 \pm 3) \times 10^{-3}$	7037
100	/MNTtoEE_M-100_TZ8_alp/S12	$(3562 \pm 1) \times 10^{-3}$	14037
125	/MNTtoEE_M-125_TZ8_alp/S12	$(1076.7 \pm 0.3) \times 10^{-3}$	46242
150	/MNTtoEE_M-150_TZ8_alp/S12	$(4594 \pm 1) \times 10^{-4}$	108827
175	/MNTtoEE_M-175_TZ8_alp/S12	$(2326.6 \pm 0.7) \times 10^{-4}$	214442
200	/MNTtoEE_M-200_TZ8_alp/S12	$(1312.7 \pm 0.4) \times 10^{-4}$	380833
225	/MNTtoEE_M-225_TZ8_alp/S12	$(7966 \pm 2) \times 10^{-5}$	627547
250	/MNTtoEE_M-250_TZ8_alp/S12	$(5093 \pm 2) \times 10^{-5}$	979699
275	/MNTtoEE_M-275_TZ8_alp/S12	$(3386 \pm 1) \times 10^{-5}$	1476652
300	/MNTtoEE_M-300_TZ8_alp/S12	$(2321.4 \pm 0.7) \times 10^{-5}$	2153700
325	/MNTtoEE_M-325_TZ8_alp/S12	$(1631.7 \pm 0.5) \times 10^{-5}$	3063798
350	/MNTtoEE_M-350_TZ8_alp/S12	$(1170.5 \pm 0.4) \times 10^{-5}$	4271252
375	/MNTtoEE_M-375_TZ8_alp/S12	$(8545 \pm 3) \times 10^{-6}$	5826500
400	/MNTtoEE_M-400_TZ8_alp/S12	$(6332 \pm 2) \times 10^{-6}$	7879057
500	/MNTtoEE_M-500_TZ8_alp/S12	$(2154 \pm 1) \times 10^{-6}$	23208152
600	/MNTtoEE_M-600_TZ8_alp/S12	$(8545 \pm 5) \times 10^{-7}$	58506729
700	/MNTtoEE_M-700_TZ8_alp/S12	$(3831 \pm 3) \times 10^{-7}$	130502193

Table 4.3: The abbreviations used in Table 4.2.

S12	=	Summer12_DR53X-PU_S10_START53_V7A-v1/AODSIM
S12a	=	Summer12_DR53X-PU_S10_START53_V19-v1/AODSIM
MNTtoEE	=	MajoranaNeutrinoToEE
TZ8_alp	=	TuneZ2star_8TeV-alp

4.2.3 Standard Model Monte Carlo Samples

Table 4.4 summarizes all the Monte Carlo (MC) samples used in this analysis for background estimation and validation of the data-driven background estimation methods. Table 4.5 shows the lists of abbreviations used in Table 4.4. The cross section, $\sigma(pb)$ and integrated luminosity $L(pb^{-1})$ of each sample is given. In the table, diboson, $t\bar{t}W$ and same sign W pair production samples are used to estimate the number of events from the SM. The $t\bar{t}$, W+jets, and QCD samples are used for validation of the fake background estimation method. The MC samples are reweighted for proper simulation of the number of interactions.

4.3 Event Selection

The signal signature for Majorana neutrino search in dielectron channel is two electrons and two jets. Normally, both same-sign and opposite-sign dielectons are possible but we concentrate on the same-sign dielectron production ($pp \rightarrow Ne^\pm \rightarrow e^\pm e^\pm q\bar{q}'$) in this study due to the fact that this final state has very low SM backgrounds. The Majorana neutrino produces an accompanying W boson. We are interested in signatures in which W decays to two jets, as this allows us to reconstruct the mass of heavy neutrino without any missing final state energy.

4.3.1 Trigger

In this search, we selected the signal events by using dilepton triggers, requiring the first electron, *leading electron*, has a $p_T > 17$ GeV/c and the second electron, *trailing electron*, has a $p_T > 8$ GeV/c at the High-Level Trigger (HLT). The efficiency

Table 4.4: Summary of the used Monte Carlo datasets for the Standard Model processes. The abbreviations are listed in Table 4.5.

Dataset	Dataset Name	σ (pb)	$\int \mathcal{L} dt$ (pb $^{-1}$)
W^+W^-	/WW_TZ8_py6.ta/S12a	54.8	1.82×10^5
WZ	/WZ_TZ8_py6.ta/S12a	33.2	3.01×10^5
ZZ	/ZZ_TZ8_py6.ta/S12a	17.7	5.55×10^5
$W\gamma$	/WGToLNUG_TZ8-ma-ta/S12a	462	1.04×10^4
W^+W^+	/WpWpqq_8-ma/S12a	0.248	4.03×10^5
W^-W^-	/WmWmqq_8-ma/S12a	0.0888	1.08×10^6
dp $W^\pm W^\pm$	/WW_DS_8TeV-pythia8/S12a	0.588	1.42×10^6
$WW\gamma$	/WWGJets_8-ma_v2/S12a	0.528	5.76×10^5
WWW	/WWWJets_8-ma/S12a	0.082	2.68×10^6
WWZ	/WWZNoGstarJets_8-ma/S12a	0.058	3.83×10^6
WZZ	/WZZNoGstarJets_8-ma/S12b	0.0197	1.12×10^7
ZZZ	/ZZZNoGstarJets_8-ma/S12a	5.53×10^{-3}	4.07×10^7
$t\bar{t}$	/TTJets_MBD_TZ8-ma-ta/S12b	234	2.96×10^4
t (tW^-)	/T_tW-channel-DR_TZ8-po-ta/S12a	10.7	4.65×10^4
\bar{t} ($\bar{t}W^+$)	/Tbar_tW-channel-DR_TZ8-po-ta/S12a	10.7	4.61×10^4
t (s -channel)	/T_s-channel_TZ8-po-ta/S12a	2.82	9.22×10^4
\bar{t} (s -channel)	/Tbar_s-channel_TZ8-po-ta/S12a	1.57	8.92×10^4
t (t -channel)	/T_t-channel_TZ8-po-ta/Summer12a	47.0	8.00×10^4
\bar{t} (t -channel)	/Tbar_t-channel_TZ8-po-ta/S12a	25.0	7.74×10^4
$t\bar{t}W$	/TTWJets_8-ma/S12a	0.232	8.45×10^5
$t\bar{t}Z$	/TTZJets_8-ma_v2/S12a	0.174	1.21×10^6
$t\bar{t}WW$	/TTWWJets_8-ma/S12a	2.04×10^{-3}	1.07×10^8
VH ($H \rightarrow WW$)	/WH_ZH_TTH1/S12a	0.2604	7.70×10^5
VH ($H \rightarrow \tau\tau$)	/WH_ZH_TTH2/S12a	0.0177	5.49×10^6
ggH ($H \rightarrow ZZ$)	/Glu/S12a	0.0524	1.90×10^7
Drell-Yan	/DYJetsToLL_M-10To50_TZ8-ma/S12a	1.11×10^4	3.42×10^3
Drell-Yan	/DYJetsToLL_M-50_TZ8-ma-tar/S12a	3.50×10^3	8.69×10^3
W +jets	/WJetsToLNu_TZ8-ma-tar/S12c	3.75×10^4	1.54×10^3
QCD_20to30E	/QCD_Pt_20_30_EM_TZ8_py6/S12a	2.91×10^6	12.0
QCD_30to80E	/QCD_Pt_30_80_EM_TZ8_py6/S12a	4.62×10^6	7.2
QCD_80to170E	/QCD_Pt_80_170_EM_TZ8_py6/S12a	1.83×10^5	188
QCD_170to250E	/QCD_Pt_170_250_EM_TZ8_py6/S12a	4590	6910
QCD_250to350E	/QCD_Pt_250_350_EM_TZ8_py6/S12a	560	62200
QCD_350E	/QCD_Pt_350_EM_TZ8_py6/S12a	89	382000
QCD_20to30E	/QCD_Pt_20_30_BCtoE_TZ8_py6/S12a	167000	10.4
QCD_30to80E	/QCD_Pt_30_80_BCtoE_TZ8_py6/S12a	167000	12.3
QCD_80to170E	/QCD_Pt_80_170_BCtoE_TZ8_py6/S12a	13000	150
QCD_170to250E	/QCD_Pt_170_250_BCtoE_TZ8_py6/S12a	631	3080
QCD_250to350E	/QCD_Pt_250_350_BCtoE_TZ8_py6/S12a	103	19600
QCD_350E	/QCD_Pt_350_BCtoE_TZ8_py6/S12a	24	81500
QCD_30to40EE	/QCD_Pt-30to40_dEM_TZ8_py6/S12a	12200	497
QCD_40EE	/QCD_Pt-40_dEM_TZ8_py6/S12a	113000	86

Table 4.5: The abbreviations used in Table 4.4

S12a	=	Summer12_DR53X-PU_S10_START53_V7A-v1/AODSIM
S12b	=	Summer12_DR53X-PU_S10_START53_V7C-v1/AODSIM
S12c	=	Summer12_DR53X-PU_S10_START53_V7A-v2/AODSIM
S12d	=	Summer12_DR53X-PU_S10_START53_V7A-v3/AODSIM
dEM_TZ8-py6	=	doubleEMEnriched_TuneZ2star_8TeV-pythia6
EM_TZ8_py6	=	EMEnriched_TuneZ2star_8TeV-pythia6
TZ8-ma-tar	=	TuneZ2Star_8TeV-madgraph-tarball
TZ8-ma-ta	=	TuneZ2star_8TeV-madgraph-tauola
TZ8_py6-ta	=	TuneZ2star_8TeV-pythia6-tauola
TZ8-po-ta	=	TuneZ2star_8TeV-powheg-tauola
ld8-py6-ta	=	lepdecay_8TeV-pythia6-tauola
TTH1	=	TTH_HToWW_M-125_8TeV-pythia6
TTH2	=	TTH_HToTauTau_M-125_ld8-py6-ta
Glu	=	GluGluToHToZZTo4L_M-125_8-po-py6
TZ8_py6	=	TuneZ2star_8TeV-pythia6
dp $W^\pm W^\pm$	=	double parton $W^\pm W^\pm$
TZ8-ma	=	TuneZ2star_8TeV-madgraph
8-po-py6	=	8TeV-powheg-pythia6
MBD	=	MassiveBinDECAY
DS	=	DoubleScattering
8-ma	=	8TeV-madgraph
ld	=	lepdecay

of this trigger is discussed in Section 4.4 and the corresponding integrated luminosity for this trigger is 19.7 fb^{-1} .

Trigger = HLT_Ele17_CaloIdT_CaloIsoVL_TrkIdVL_TrkIsoVL_Ele8_CaloIdT_CaloIsoVL_TrkIdVL_TrkIsoVL.

For the fake rate calculations to determine the background, the events collected with single electron triggers were used. These triggers are HLT_Ele8 and HLT_Ele17 and the corresponding integrated luminosity for these triggers are 20 pb^{-1} .

4.3.2 Primary Vertex Selection

In this study, every event is required to have at least one good primary vertex to ensure they are coming from good collision events and not fakes. The primary vertex reconstruction consists of three steps: (a) track selection, (b) track clustering, which

are from the same interaction vertex and (c) position fitting for each vertex using the associated tracks [64]. Following these steps, if a vertex has all the requirements listed below is accepted as a primary vertex.

- a vertex has more than 4 degrees of freedom in the fit.
- a vertex within 24 cm of the nominal detector center in z-direction.
- a vertex within 2 cm of the beam spot in transverse direction.

4.3.3 Electron Selection

In this analysis, we require to have at least two “tight” electrons, which are selected by using tight cut based electron ID as defined by the EGamma Physics Object Group (POG) [65, 66]. The EGamma POG defines cut severity levels on the cut variables for selecting dielectrons from Z events. These cut levels are called *veto*, *loose*, *medium* and *tight* and the names imply the severity of the cuts.

Here, we use the *tight* selection and in addition, we require the following cuts for electrons:

- the transverse impact parameter (d_{xy}) relative to the primary vertex < 0.1 mm,
- required consistency of the three independent charge measurements (CTF, GSF, SC),
- $p_T > 15$ GeV/c,
- $|\eta| < 2.5$,
- well isolated electrons: particle flow (PF)-base relative isolation, $I_{rel} < 0.09$ for electrons in the barrel and $I_{rel} < 0.05$ for electrons in the endcap (forward

electrons) region,

- electrons in the transition region between the ECAL barrel and endcap ($1.4442 < |\eta| < 1.566$) are vetoed because they are not considered as good reconstructed electrons.

Electron candidates are reconstructed using the medium cut ID (medium working point (WP)) provided by the EGamma POG to clean the jet events with respect to every lepton within $\Delta R = \sqrt{(\Delta\eta)^2 + (\Delta\phi)^2} < 0.4$.

4.3.4 Muon Selection

We use muons, which pass the loose ID defined by the Muon POG [67]. Similar to EGamma POG, Muon POG defines cut severity levels on the muon cut variables for selecting dimuon events and the cut levels are called *loose*, *medium* and *tight*. Here, *tight* implies the most and *loose* implies the least severe cut. In our study, the cuts below are applied to remove events with muons.

- $p_T > 10 \text{ GeV}/c$
- $|\eta| < 2.4$

4.3.5 Jet and E_T^{miss} Selection

We required preselection events with two or more jets, which are well separated from the electron candidates with $\Delta R > 0.4$ and they have $p_T > 20 \text{ GeV}/c$. They must be within the tracker coverage, $|\eta| < 2.5$.

Jets are reconstructed from calorimeter and tracker information using particle

flow algorithm. To reduce possible fake backgrounds from top quark decays, events including a jet that is identified from a b quark decay are rejected.

In order to reject the events with incorrectly reconstructed E_T^{miss} , we filter the events according to the prescription provided by JetMET Physics Object Group (POG) [68, 69].

4.3.6 Preselection Requirements

After selecting only events with two electrons and two jets, the following criteria is applied:

- leading electron $p_T > 20 \text{ GeV}/c$,
- dielectron mass (m_{ee}) $> 10 \text{ GeV}/c^2$,
- dielectron mass not within the Z peak, $|m_{ee} - 90| > 10 \text{ GeV}/c^2$,
- events with a muon passing the loose ID are excluded,
- events with an extra electron, which is passing a veto ID are excluded and veto

ID is:

- POG ID working points (WP) (analysis uses *tight* and veto uses *veto WP*),
- RelIso (analysis cut < 0.09 for EB and < 0.05 for EE, veto cut < 0.6),
- $p_T > 10 \text{ GeV}/c$.

The Z peak region is removed in this analysis due to the large background from charge flip events in this region. For a detailed information about the charge flip background, please see Section 4.5. Good agreements between data and backgrounds were observed, and the preselection cuts were optimized accordingly.

4.3.7 Additional Selection Requirements

We have defined two different heavy neutrino mass search regions due to the possibility of having an on-shell (real) or off-shell (virtual) W-boson propagator. Further selection requirements are made according to different selection criteria for these two search regions.

- Low-mass search region, $40 \text{ GeV}/c^2 < m_N < 80 \text{ GeV}/c^2$
- High-mass search region, $90 \text{ GeV}/c^2 < m_N < 500 \text{ GeV}/c^2$

Low-mass search region: When $m_N < m_W$, the W-boson propagator, which produces heavy neutrino, Fig. 4.1, is on-shell and the final state system of $e^\pm e^\pm + \bar{q}q'$ should have an invariant mass close to m_W . The following selection cuts are applied for this search region.

- Events with one or more b-tags (using the CSV Medium working point) are excluded,
- missing transverse energy (MET) less than 30 GeV,
- invariant mass of the two electrons and two jets $m(eejj) < 200 \text{ GeV}/c^2$, where the two jets chosen are those which result in $m(e^\pm e^\pm + jj)$ closest to m_W ,
- invariant mass of two jets $m(jj) < 120 \text{ GeV}/c^2$, where the two jets used are the same ones selected for the $m(e^\pm e^\pm jj)$ cut.

High-mass search region: When $m_N > m_W$, the W-boson propagator is off-shell but the W-boson from the Majorana neutrino (N) decay is on-shell so the $W \rightarrow \bar{q}q'$ decay should result in a dijet invariant mass close to m_W . The following selection cuts are

Table 4.6: Summary of the selection requirements for the low-mass and high-mass signal regions.

Region	MET (GeV)	$m(e^\pm e^\pm jj)$ (GeV/c ²)	$m(e^\pm e^\pm)$ (GeV/c ²)	$m(jj)$ (GeV/c ²)	$p_T^{j_1}$ (GeV/c)
Low-Mass	< 30	< 200	> 10	< 120	> 20
High-Mass	< 35	> 80	> 15	50 – 110	> 30

imposed for this search region.

- Events with one or more b-tags (using the CSV Medium working point) are excluded,
- leading jet $p_T > 30 \text{ GeV}/c$,
- dielectron invariant mass $m(ee) > 15 \text{ GeV}/c^2$,
- MET is less than 35 GeV (relaxed from 30 GeV to avoid the losing signal efficiency in high mass events where the MET distribution is broader due to higher jet activity),
- dijet invariant mass $50 < m(jj) < 110 \text{ GeV}/c^2$, where the two jets with invariant mass closest to m_W are chosen.

Table 4.6 summarizes the selection requirements for the low-mass and high-mass signal regions.

4.3.8 Final Optimization for Signal Selection

After applying all the selection criteria explained above, we further optimized signal significance based on five variables by using the Punzi figure of merit [70],

defined as $\epsilon_S/(a/2 + \delta B)$. In the equation, $a = 2$ with the number of standard deviations, ϵ_S is the signal selection efficiency and δB is the uncertainty on the estimated background. The five variables are:

- p_T^{e1} , transverse momentum of the leading electron
- p_T^{e2} , transverse momentum of the sub-leading electron
- $m(eejj)$, invariant mass of two electrons and two jets
- $m(ee)$, invariant mass of two electrons
- $m(e_2jj)$, invariant mass of the sub-leading electron and two jets.

The final optimized cuts on these variables and overall signal acceptance for Majorana mass points, $40 - 500 \text{ GeV}/c^2$ are listed in Table 4.7. The signal acceptance is ranging between 0.19-17 % for the neutrino mass range of 40-500 GeV/c^2 .

4.4 Selection Efficiency

In this section, efficiency of the chosen dielectron triggers, efficiency of the selecting two isolated electrons with all the selection cuts and scale factor calculations for data and Monte Carlo will be discussed.

The efficiency of the dielectrons triggers discussed in Section 4.3.1 were directly taken from [71]. The electron trigger efficiency was 0.92 when sub-leading electron has $p_T^{e2} < 30 \text{ GeV}/c$ and it was 0.96 when $p_T^{e2} > 30 \text{ GeV}/c$.

The efficiency of selecting two isolated electrons, $p_T > 20, 15 \text{ GeV}/c$ passing all the selection cuts described in Section 4.3 is provided in Table 4.8. The table shows the individual as well as all cut efficiencies obtained from the signal Monte

Table 4.7: Summary of the final optimization cuts on five variables and overall signal acceptance [52].

m_N (GeV/c^2)	$m(e^\pm e^\pm jj)$ (GeV/c^2)	$p_T^{e_1}$ (GeV/c)	$p_T^{e_2}$ (GeV/c)	$m(e_2 jj)$ (GeV/c^2)	$m(e^\pm e^\pm)$ (GeV/c^2)	Acc. Eff. (%)
40	80-160	> 20	> 15	< 120	$10 - 60$	0.19
50	80-160	> 20	> 15	< 120	$10 - 60$	0.26
60	80-160	> 20	> 15	< 120	$10 - 60$	0.22
70	80-160	> 20	> 15	< 120	$10 - 60$	0.09
80	80-160	> 20	> 15	< 120	$10 - 60$	0.32
90	> 120	> 20	> 15	$60 - 120$	> 15	0.46
100	> 120	> 20	> 15	$80 - 120$	> 15	1.9
125	> 140	> 25	> 25	$105 - 145$	> 15	4.2
150	> 195	> 40	> 25	$125 - 175$	> 15	6.5
175	> 235	> 45	> 30	$155 - 200$	> 15	6.4
200	> 280	> 65	> 40	$160 - 255$	> 15	8.4
250	> 300	> 110	> 40	--	> 15	11
300	> 320	> 120	> 40	--	> 15	14
350	> 360	> 120	> 40	--	> 15	16
400	> 360	> 120	> 40	--	> 15	17
500	> 360	> 120	> 40	--	> 15	17

Carlo samples. Here only statistical errors are included.

Around $m_N = 80 \text{ GeV}/c^2$, the efficiency of two isolated electrons selection drops considerably. This is due to the fact that Majorana neutrino is either producing a W boson or it is produced from an on-shell W-boson. When the mass of neutrino is getting closer to the mass of W boson ($m_W = 80.4 \text{ GeV}/c^2$), the electrons' momentum drop below our threshold and they can not pass the selection cuts.

Table 4.8: The efficiency to select two isolated electrons with $p_T > 20, 15 \text{ GeV}/c$ passing all the selection cuts.

m_N (GeV/c^2)	Total Events	% Events Accepted			
		Tight ID	η and p_T	Isolation	All
40	99390	9.1 ± 0.1	13.6 ± 0.1	15.3 ± 0.1	4.2 ± 0.1
60	99494	9.0 ± 0.1	9.5 ± 0.1	15.6 ± 0.1	2.6 ± 0.1
70	49994	3.5 ± 0.1	3.0 ± 0.1	6.8 ± 0.1	0.9 ± 0.0
80	98492	7.1 ± 0.1	10.5 ± 0.1	10.9 ± 0.1	3.5 ± 0.1
90	49996	6.9 ± 0.1	8.9 ± 0.1	9.9 ± 0.1	2.4 ± 0.1
100	49996	16.6 ± 0.2	24.7 ± 0.2	23.0 ± 0.2	8.1 ± 0.1
125	49995	29.1 ± 0.2	46.3 ± 0.3	38.4 ± 0.3	21.3 ± 0.2
150	49995	35.0 ± 0.3	52.6 ± 0.3	45.4 ± 0.3	27.9 ± 0.2
175	49995	38.7 ± 0.3	56.5 ± 0.3	50.1 ± 0.3	32.4 ± 0.3
200	49992	41.6 ± 0.3	59.1 ± 0.3	53.8 ± 0.3	35.8 ± 0.3
250	49997	45.4 ± 0.3	62.2 ± 0.4	58.4 ± 0.3	40.1 ± 0.3
300	49996	48.1 ± 0.3	64.4 ± 0.4	61.7 ± 0.4	43.3 ± 0.3
350	49995	49.4 ± 0.3	65.0 ± 0.4	63.2 ± 0.4	44.6 ± 0.3
400	49996	50.5 ± 0.3	66.3 ± 0.4	64.7 ± 0.4	45.9 ± 0.3
500	49995	50.8 ± 0.3	66.8 ± 0.4	65.1 ± 0.4	46.2 ± 0.3

Table 4.9 shows the overall efficiency to select signal events passing all the final cuts discussed in Section 4.3.1. The efficiencies were obtained from signal Monte

Table 4.9: Event selection efficiencies for the events passing all the selection cuts.

m_N (GeV/c^2)	Total Events	% Events Accepted			Number of Events for 19.7 fb^{-1}
		All Electron	Jets	All Cuts	
40	99390	4.2 ± 0.1	24.2 ± 0.13	0.19 ± 0.02	76435.0 ± 2126.0
60	99494	2.6 ± 0.1	30.4 ± 0.18	0.22 ± 0.02	26418 ± 1000
70	49994	0.9 ± 0.0	35.1 ± 0.26	0.09 ± 0.02	5442 ± 460
80	98942	3.5 ± 0.1	47.1 ± 0.22	0.32 ± 0.04	2019 ± 59
90	49996	2.4 ± 0.1	60.3 ± 0.35	0.46 ± 0.05	691 ± 40
100	49996	8.1 ± 0.1	64.8 ± 0.36	1.90 ± 0.09	1400 ± 46
125	49995	21.3 ± 0.2	70.1 ± 0.37	4.19 ± 0.16	2798 ± 33
150	49995	27.9 ± 0.2	74.5 ± 0.39	6.52 ± 0.19	588 ± 6
175	49995	32.4 ± 0.3	77.4 ± 0.39	6.39 ± 0.21	352 ± 3
200	49992	35.8 ± 0.3	80.3 ± 0.40	8.36 ± 0.22	254 ± 5
250	49997	40.1 ± 0.3	83.5 ± 0.41	10.59 ± 0.24	95 ± 3
300	49996	43.3 ± 0.3	85.4 ± 0.41	13.96 ± 0.26	63.1 ± 0.9
350	49995	44.6 ± 0.3	86.5 ± 0.42	16.07 ± 0.27	37.5 ± 0.4
400	49996	45.9 ± 0.3	86.7 ± 0.42	17.16 ± 0.27	20.9 ± 0.2
500	49995	46.2 ± 0.3	85.2 ± 0.41	16.62 ± 0.27	6.0 ± 0.1

Carlo samples and only statistical errors are included.

4.4.1 Tag and Probe Study: Data and Monte Carlo Scale Factor

The accuracy of the simulation of the signal events can be examined via a tag and probe method on events where a Z boson decays to two charged leptons. This method has been used successfully in previous CMS analyses [72–75]. It is a common tool to measure the defined object (electron in our case) efficiency from data at the experiment. In this method, resonances (Z boson in our case) are reconstructed as pairs of tag (passing a tight identification) and probe (passing a loose identification) particles. A particle ID requirement is defined later according to whatever

is the efficiency to measure. Probes passing this ID requirement are called passing probes and the probes failing the ID requirement are called failing probes. Then, resonances of the tag+passing probes and tag+failing probes are fit separately with a signal+background model. Later, the efficiency is calculated from the ratio of the signal yields of those two lineshapes. The efficiency calculation is done for Monte Carlo and data separately and the efficiency ratio of data and MC provides a scale factor that is used for the rest of the analysis.

In this study, we used the full double electron-triggered data collected by CMS detector in 2012, shown in Table 4.1 and full Drell-Yan Monte Carlo sample, shown as ‘/DYJetsToLL_M-50_TZ8-ma-tar/S12a’ in Table 4.4. This study is done for p_T regions of 10-15, 15-20, 20-30, 30-40, 40-50 and 50-200 GeV, and $|\eta|$ in regions of 0.0-0.8, 0.8-1.4442, 1.566-2.0 and 2.0-2.5. The $1.4442 < |\eta| < 1.566$ region is not included because that is the transition region between the ECAL barrel and endcap. Electrons in that region are not considered as good reconstructed electrons.

In both data and Monte Carlo, we require probes as set of all electrons that initially pass:

- $p_T > 15 \text{ GeV}/c$
- $|\eta| < 2.5$

Here, passing probes (P) and failing probes (F) are the subsets of all probe collection. P denotes a probe that passes the full ID requirement and F are probe electrons that fail our electron ID requirement. The tag electrons (T) pass our full selection criteria:

- $p_T > 25 \text{ GeV}/c$
- $|\eta| < 2.5$
- Tight ID criteria

We used the tight electron ID introduced by EGamma POG in Refs. [66,76,77] with the additional cuts below:

- the transverse impact parameter (d_{xy}) relative to the primary vertex < 0.1 mm,
- well isolated electrons: particle flow (PF)-base relative isolation, $I_{rel} < 0.09$ for electrons in the barrel and $I_{rel} < 0.05$ for electrons in the endcap (forward electrons) region,
- *ElectronGsfCtfScPixCharge* required (a consistency of the three independent charge measurements: CTF, GSF, SC).

A detailed description of the method used to extract the efficiencies is discussed in Refs. [66,76,77]. In summary, the fitting method is used for data selection efficiencies and simply counting method is used for MC selection efficiencies assuming negligible backgrounds. The electron efficiency (ϵ) is determined with the equation 4.2, where N_{TT} , N_{TP} and N_{TF} are the number of events for the types of ‘tag-tag’, ‘tag-passing probe’ and ‘tag-failing probe’ electron pairs, respectively. The scale factor (ρ) is determined with the equation below, which is the efficiency ratio of the data to the Monte Carlo.

$$\epsilon = \frac{2N_{TT} + N_{TP}}{2N_{TT} + (N_{TP} + N_{TF})} \quad (4.2)$$

$$\rho = \frac{\epsilon_{Data}}{\epsilon_{MC}} \quad (4.3)$$

In Monte Carlo simulation, the efficiencies are obtained by simply counting the number of events in Z -boson. While in data these numbers are the yields from fitting the tag-probe electron pair mass distributions with a three-part fit equation. The resonant part of the distribution was fitted with the convolution of *Breit-Wigner* (BW) and *Crystal-Ball* (CB) functions, the non-resonant part was fitted with a second-order *Chebyshev* (CC) and the background was fitted with an *Exponential* function. The Z peak is expected to be nontrivial and it is described well with these functions. The fit is performed in the invariant mass region of $60 \text{ GeV}/c^2 < m(e^+e^-) < 120 \text{ GeV}/c^2$ and the signal is taken as the integral of the fitted signal function.

Figure 4.4 shows examples of the Z boson mass peak for $Z \rightarrow ee$ in data. Here, (a) and (b) plots are passing probes (numerator in Eq. 4.2) and all probes (denominator in Eq. 4.2) respectively in $0.0 < \eta < 0.8$ region for $15 < p_T < 20 \text{ GeV}$ and (c) and (d) plots are passing probes and all probes in $0.8 < \eta < 1.4442$ region for $50 < p_T < 200 \text{ GeV}$. All the mass distribution plots for all p_T and in all η regions can be found at the author's website [78].

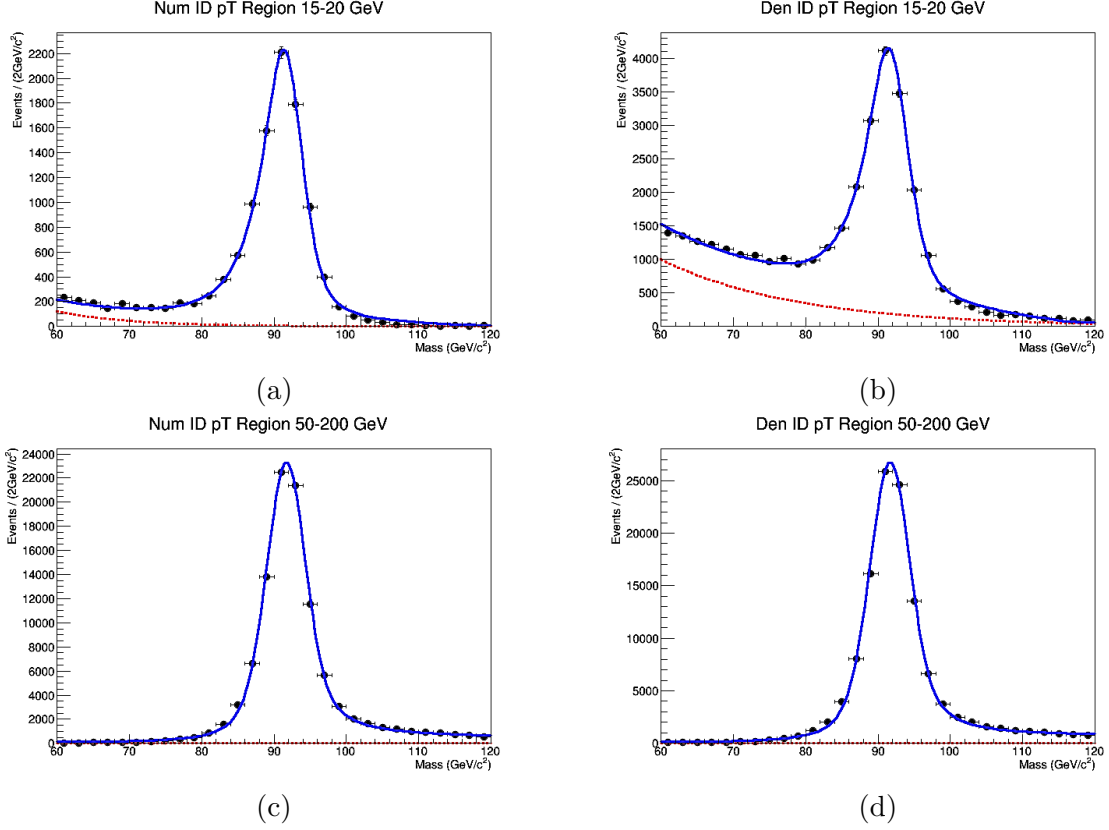


Figure 4.4: Examples of tag-probe electron pair mass distributions for $Z \rightarrow ee$ events in data.

In the kinematic range of the electrons produced by our signal we find that the electrons are well modelled by the simulation, as seen in Table 4.10. The scale factors are applied according to one of four kinematic regions, depending on p_T and η , shown in Fig. 4.5.

A systematic error of 2% on the electron identification and isolation is estimated by varying the fit function used in the tag-and-probe studies [76].

Table 4.10: Electron identification (including isolation) efficiencies in bins of p_T and $|\eta|$ for both simulation and data measured with the tag-and-probe method.

$ \eta $	p_T (GeV/c)	Data	MC	Data/MC
0.0 – 0.8	15 – 20	0.516	0.532	0.969 ± 0.013
	20 – 30	0.653	0.682	0.958 ± 0.003
	30 – 40	0.756	0.783	0.966 ± 0.001
	40 – 50	0.812	0.834	0.973 ± 0.001
	50 – 200	0.831	0.859	0.967 ± 0.002
0.8 – 1.4442	15 – 20	0.475	0.496	0.957 ± 0.014
	20 – 30	0.576	0.635	0.908 ± 0.004
	30 – 40	0.688	0.748	0.920 ± 0.002
	40 – 50	0.772	0.813	0.949 ± 0.002
	50 – 200	0.797	0.840	0.948 ± 0.002
1.566 – 2.0	15 – 20	0.220	0.252	0.875 ± 0.030
	20 – 30	0.355	0.402	0.884 ± 0.009
	30 – 40	0.430	0.508	0.847 ± 0.004
	40 – 50	0.512	0.570	0.898 ± 0.004
	50 – 200	0.560	0.616	0.910 ± 0.006
2.0 – 2.5	15 – 20	0.202	0.253	0.801 ± 0.028
	20 – 30	0.310	0.355	0.872 ± 0.010
	30 – 40	0.382	0.426	0.895 ± 0.006
	40 – 50	0.445	0.476	0.936 ± 0.005
	50 – 200	0.484	0.515	0.940 ± 0.009

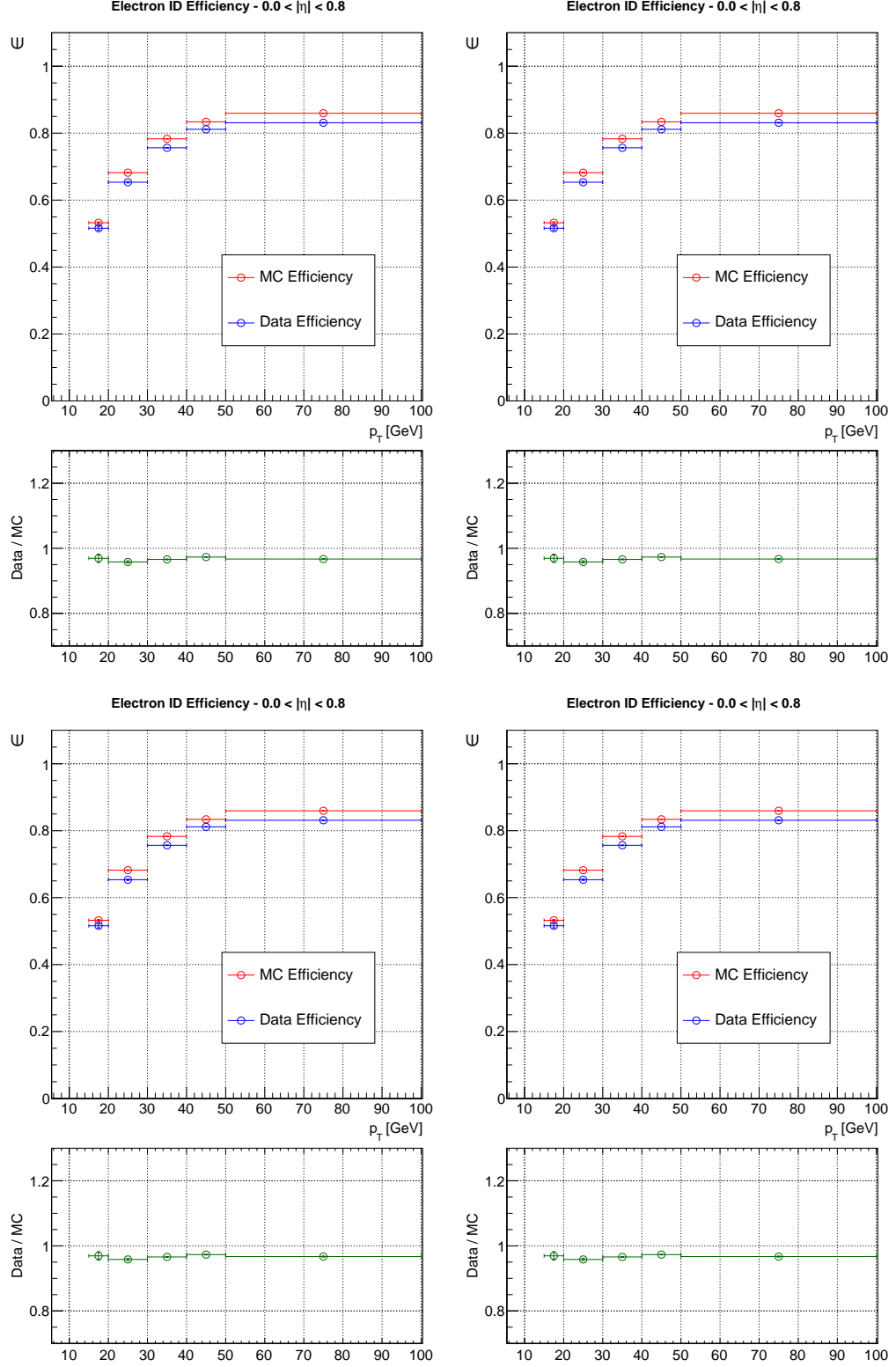


Figure 4.5: Electron efficiency results and data/MC scale factors are shown in four different η regions. Efficiency results are including isolation and impact parameter cuts.

4.5 Background Estimation

There are mainly two methods to estimate the background and they provide us a rough idea of what to expect in the data. The first one is *Monte Carlo estimation* using simulation and the second method is *data-driven estimation* using real data. The Monte Carlo is sometimes not reliable to estimate the background due to several reasons including inexact modeling of parton showering processes and lack of statistics. In that case, we use enriched control samples from collision data (data-driven) to estimate the background.

In this study, we have three major same-sign dielectron backgrounds, named as *charge-flip*, *misidentification (fakes)* and *prompt* background. The former two backgrounds were estimated by using data-driven estimate methods and the latter one was estimated by using Monte Carlo estimation.

Here, we summarized the potential background sources but more detailed information can be found in Ref. [53].

Electron misidentification background: This is the most important background source in this study in which either one or both electrons are misidentified as electrons. They are called *fakes*. In the first case, when we choose same-sign electron pair, one electron originates from a W decay while the second electron originates from a jet (b-jet) or a photon. In the second case, both electrons originate from jets and misidentified as electrons. This background is estimated using data-driven *fake rate method* with a special data sample enriched in multi-jet events. The probability for a jet that passes our *loose* electron selection cuts to that to that also passes our *tight*

electron selection cuts. This probability was determined as a function of electron transverse momentum (p_T) and pseudorapidity (η) and later used as a ‘weight’ in the calculation of the background. More details about the *fake rate method* can be found in Ref. [53].

Electron charge-flip background: The main source for this background is opposite-sign dielectron events from Z or WW decays ($Z \rightarrow e^+e^-$ and $WW \rightarrow e^\pm e^\mp$). This background is estimated using a data-driven method with a control sample of $Z \rightarrow e^\pm e^\mp$ events. The charge mismeasurement probability and scale factors (a ratio of prediction and data) were determined for barrel and endcap regions of the CMS experiment. Then, the background events such as $Z \rightarrow e^+e^-$ and $WW \rightarrow e^\pm e^\mp$ were weighted with these calculated scale factors.

Prompt electron background: This background is due to Standard Model (SM) sources from production of two same sign isolated electrons. This SM background consists of diboson events such as WZ, ZZ, $t\bar{t}$ boson events ($t\bar{t}W$, $t\bar{t}Z$, $t\bar{t}WW$), Higgs events ($H \rightarrow ZZ$ and $H \rightarrow WW$ contributes as well). All of these processes are estimated by MC simulation since they have relatively small cross sections.

4.6 Systematic Uncertainties

The dominant systematical uncertainty in this analysis coming from *signal model*, *efficiencies* and *background prediction*. Table 4.11 summarizes all the systematic uncertainties of the sources for irreducible Standard Model background and heavy Majorana neutrino signal in low-mass and high-mass selection. The largest systematic

Table 4.11: Summary of the systematic uncertainties for Majorana neutrino signal and Standard Model background (SM Bkgd.) in low-mass and high-mass search regions. Here, PDF stands for Parton Distribution Function and R&F stands for Renormalization and Factorization.

Source	Low-mass region		High-mass region	
	Signal (%)	SM Bkgd. (%)	Signal (%)	SM Bkgd. (%)
<i>MC Simulation</i>				
SM cross section	—	9-25	—	9-25
Jet energy scale	6-8	5	1-3	7
Jet energy resolution	3-7	10	2-3	7
Event pileup	2-3	4	0-2	1
Unclustered energy	1-3	4	1-2	5
Integrated luminosity	2.6	2.6	2.6	2.6
Electron selection	2	2	2	2
Trigger selection	6	6	6	6
b tagging	0-1	2	1-2	1
PDF (shape)	2.0	—	2.0	—
PDF (rate)	3.5	—	3.5	—
R&F scales	8-10	—	1-6	—
Signal MC statistics	5-15	—	1-6	—
<i>Data-Driven</i>				
Misidentified leptons	—	40	—	40
Mismeasured charge	—	12	—	12

cal uncertainty is associated with the background estimates. The uncertainties on the predictions of mismeasured electron charge (charge-flip) and misidentified electrons (misidentification) are 12% and 40% respectively for both selection regions.

4.7 Search Results

4.7.1 Results for Low Mass Search Region

In the low-mass search region ($40 \text{ GeV}/c^2 < m_N < 80 \text{ GeV}/c^2$), we observed 33 events in data after applying all selection cuts except the final optimization cuts.

The total background estimate was 32.6 ± 3.2 (stat) ± 10.7 (syst) events. In the total background, misidentified lepton background, mismeasured charge background and prompt SM background are respectively 26.7 ± 10.7 , 2.0 ± 0.2 and 4.0 ± 0.5 events. Figure 4.6 shows the kinematic distributions in the low-mass region [51]. The top distribution is the invariant mass of two electrons, the middle distribution is the invariant mass of sub-leading electron and two jets, and the bottom distribution is the transverse momentum of leading electron. The plots show the data, major background sources and two selected heavy Majorana neutrino signal, $m_N = 40 \text{ GeV}/c^2$ and $m_N = 80 \text{ GeV}/c^2$ with corresponding mixing element squared values, $|V_{eN}|^2$. As can be seen on the plots, the data yield is in agreement with the estimated backgrounds.

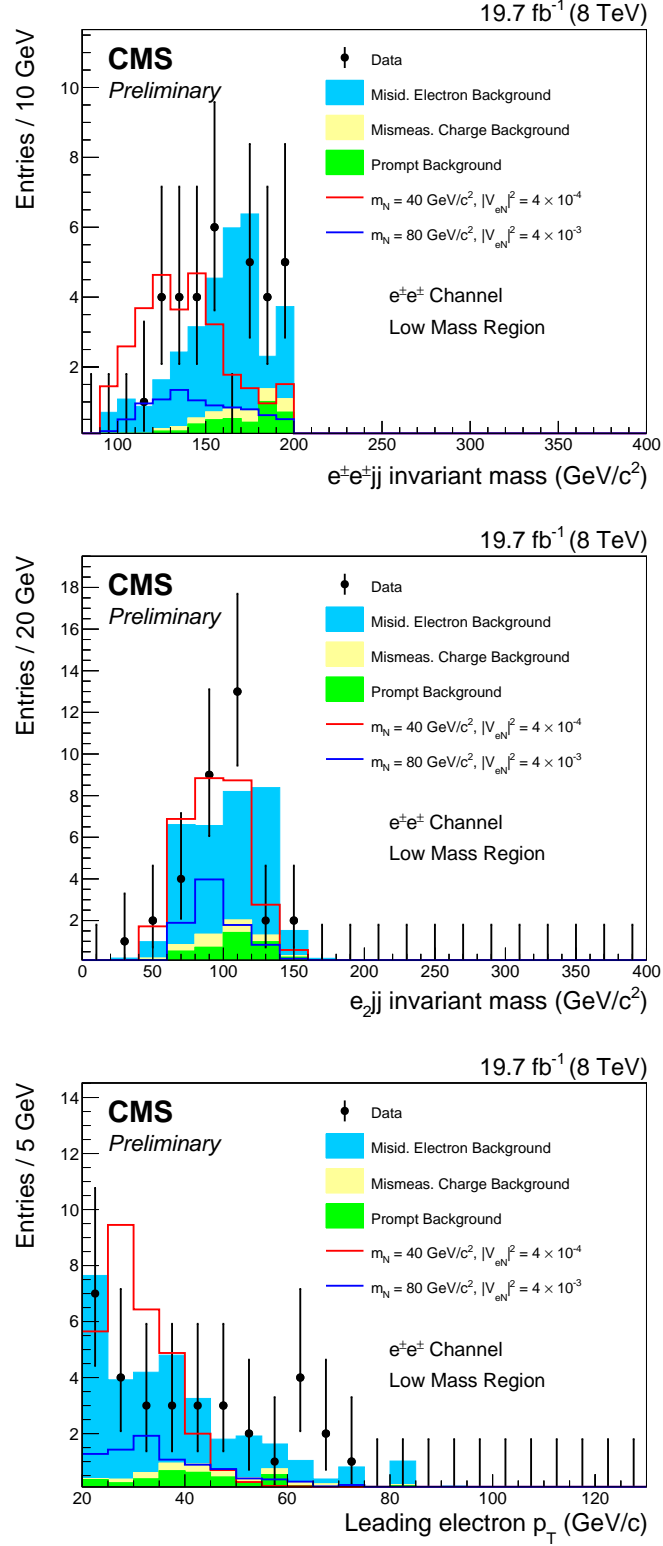


Figure 4.6: Kinematic distributions for low-mass region, $m_N < 80 \text{ GeV}/c^2$ (CMS, 2016).

4.7.2 Results for High Mass Search Region

In the high-mass region ($90 \text{ GeV}/c^2 < m_N < 500 \text{ GeV}/c^2$), we observed 54 events after all the selection cuts except final optimization cuts applied. The total background estimate was $55.4 \pm 3.6 \text{ (stat)} \pm 14.8 \text{ (syst)}$ events. Misidentified lepton background yields 36.9 ± 14.8 events, mismeasured charge background yields 7.0 ± 0.8 events, and prompt SM background yields 10.8 ± 2.2 events in this region. Figure 4.7 shows the kinematic distributions in the high-mass region, $m_N > 90 \text{ GeV}/c^2$ [51]. Top distribution is the invariant mass of two electrons, middle distribution is the invariant mass of sub-leading electron and two jets, and the bottom distribution is the transverse momentum of leading electron. The plots show the data, major background sources and two selected heavy Majorana neutrino signal, $m_N = 100 \text{ GeV}/c^2$ and $m_N = 300 \text{ GeV}/c^2$ with corresponding mixing element squared values, $|V_{eN}|^2$. As can be seen on the plots, the data yield is in agreement with the estimated backgrounds.

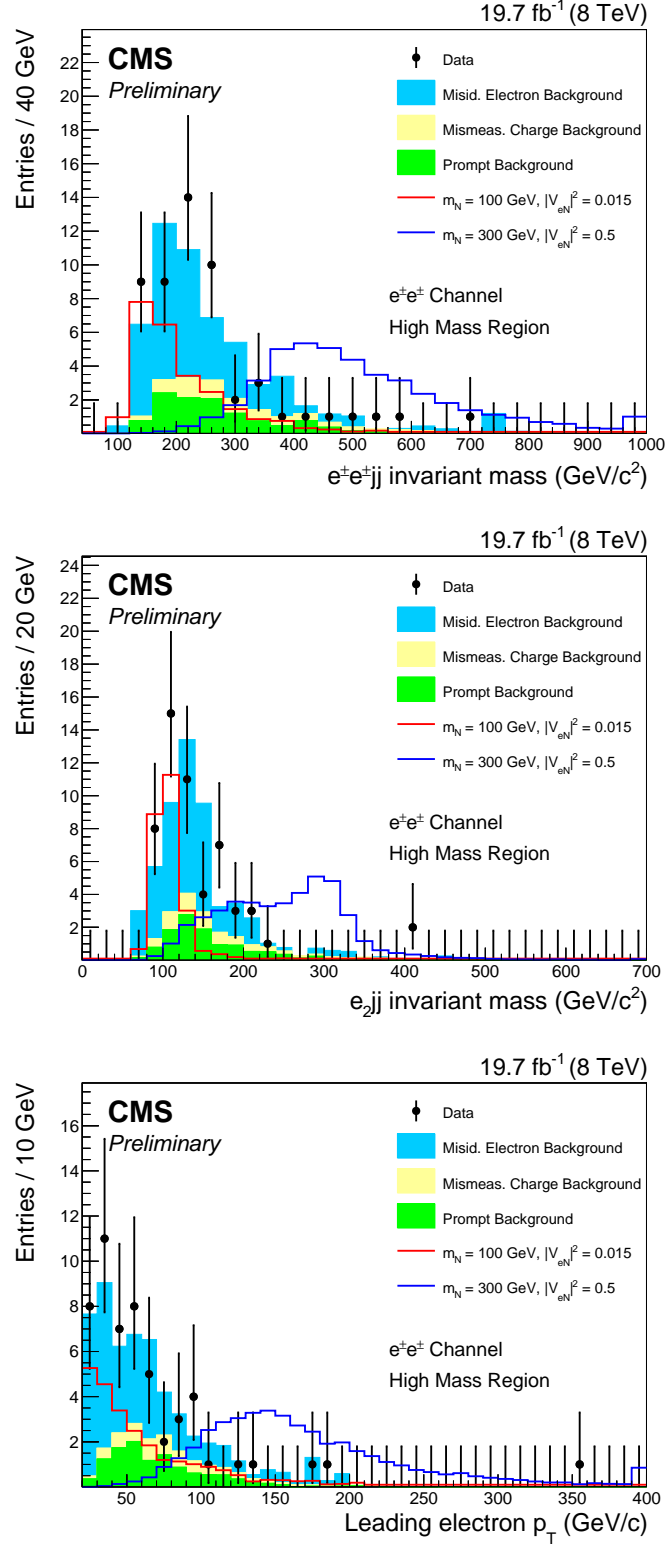
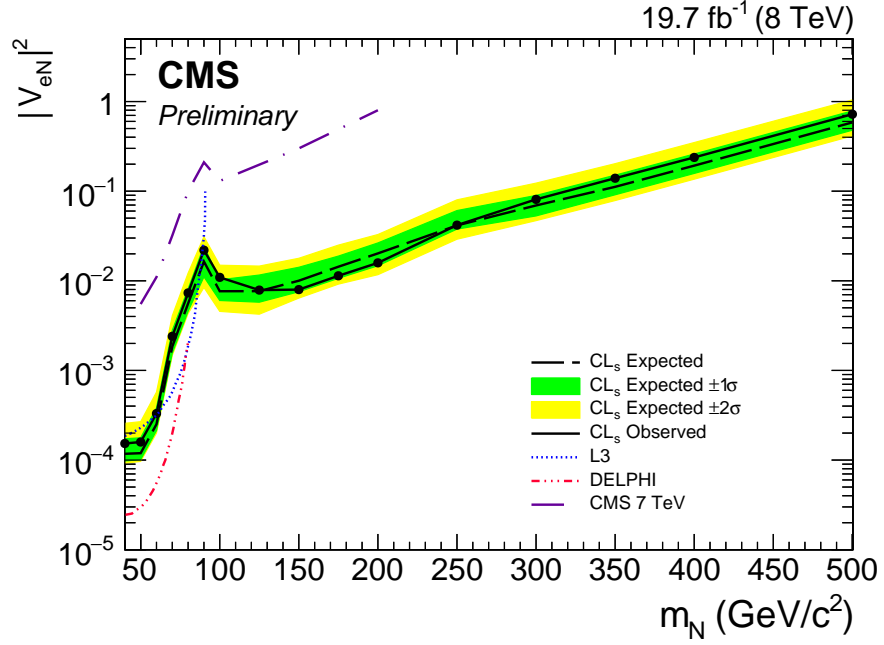


Figure 4.7: Kinematic distributions for high-mass region, $m_N > 90$ GeV/c² (CMS, 2016).

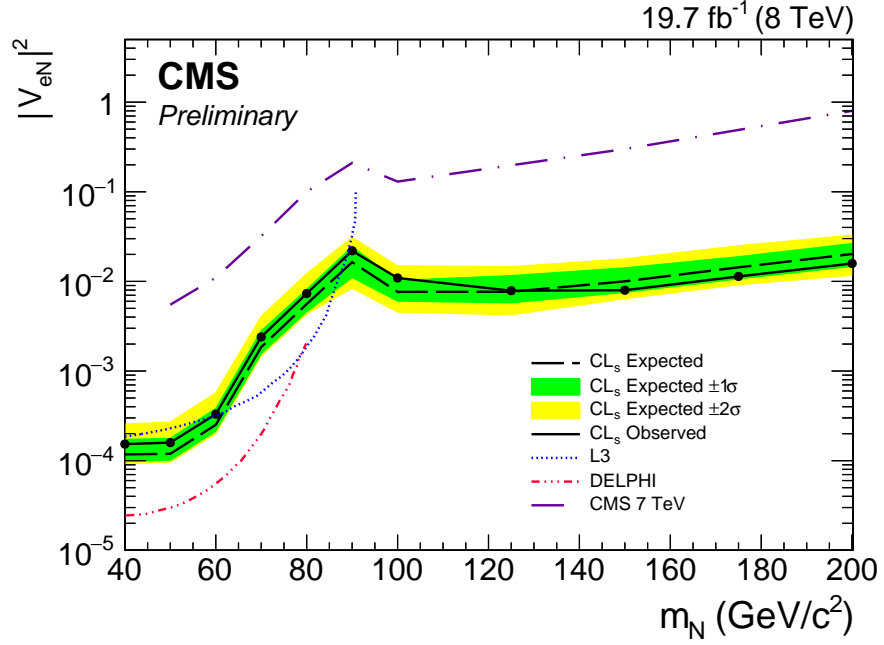
4.7.3 Exclusion Limits

We haven't observed any excess events in the data beyond the expected background predicted from SM. We have set exclusion upper limits on $|V_{eN}|^2$ with a 95% confidence level (CL), where V_{eN} is the mixing element of the heavy Majorana neutrino with the standard model ν_e neutrino. The limits are $|V_{eN}|^2 < 0.020$ for $m_N = 90$ GeV, $|V_{eN}|^2 < 0.017$ for $m_N = 200$ GeV, $|V_{eN}|^2 < 0.71$ for $m_N = 500$ GeV. At least an order of magnitude more stringent limits have been achieved on $|V_{eN}|^2$ than the limits previously set by CMS with $\sqrt{s} = 7$ TeV data. The limits are the most restricted limits for $m_N > 100$ GeV and the first limits for $m_N > 200$ GeV so far.

The resulting limits on $|V_{eN}|^2$ as a function of Majorana neutrino mass, m_N are shown in Fig. 4.8 (a) and (b) provides the expended view for the mass region of $40 \text{ GeV}/c^2 < m_N < 200 \text{ GeV}/c^2$ [51]. The dashed black curve is the expected upper limit, with one (dark green) and two (light yellow) standard-deviation bands. The plot also includes the previous upper limits set by CMS experiment with $\sqrt{s} = 7$ TeV data and the limits by DELPHI and L3 collaborations.



(a)



(b)

Figure 4.8: Exclusion upper limits on $|V_{eN}|^2$ with a 95% CL as a function of Majorana neutrino mass, m_N (a) and expanded view of the $40 \text{ GeV}/c^2 < m_N < 200 \text{ GeV}/c^2$ (b) (CMS, 2016).

As shown in Fig. 4.9, the 95% CL exclusion limits on cross section times branching fraction were also set for $\sigma(pp \rightarrow Ne^\pm \rightarrow e^\pm e^\pm q\bar{q}')$ as a function of m_N [51]. The dashed black curve is the expected upper limit, with one (dark green) and two (light yellow) standard-deviation bands. (light yellow) standard-deviation bands.

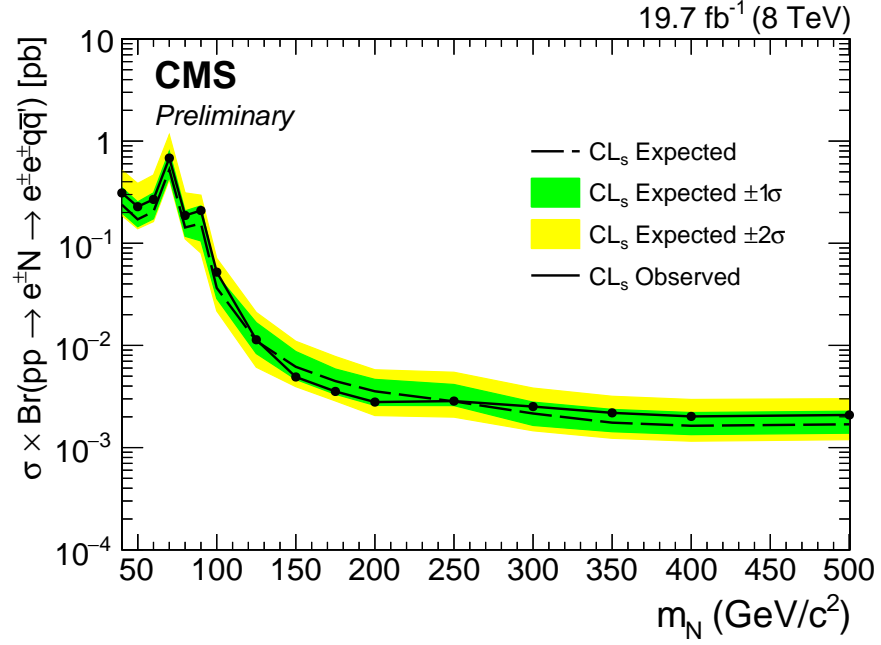


Figure 4.9: Exclusion limits on branching fraction times cross section with a 95% CL as a function of Majorana neutrino mass, m_N (CMS, 2016).

CHAPTER 5

CMS HF CALORIMETER UPGRADE: PMT CHARACTERIZATION

In this chapter, the upgrade plan of Hadronic Forward (HF) calorimeter at Compact Muon Solenoid (CMS) and the necessity of photomultiplier tube (PMT) replacement are discussed. The results of characterization of 1785 multi-anode PMTs in various parameters are presented. The testing procedure for the characterization tests are not discussed here, however they can be found in the author's M.Sc. thesis [79].

5.1 HF Calorimeter Upgrade

As mentioned in Section 3.2.4, the HF calorimeter is a sub-detector of CMS Hadronic Calorimeter (HCAL) and it is undergoing upgrade recently. The center of mass energy of proton-proton (pp) collisions at Large Hadron Collider (LHC) was 8 TeV in 2012 and the LHC has a potential up to a maximum of 14 TeV. With the energy increase, some of the sub-detectors need to be replaced with high radiation resistant ones while others need only to be calibrated. The following list is the plan of the upgrade studies for the HF calorimeters. Some of them have been already done and some will be done in the near future.

- Replacement of 1728 photomultipliers (PMT) with new four way segmented anode PMTs that have thinner glass windows, metal envelopes and higher quantum efficiency (QE).
- Replacement of total 72 readout boxes (RBX) [80].

- Replacement of timing electronics with new cable design.
- Improvement of the calibration and monitoring systems.

The physics impacts as indicated in previous studies and main physics goals of the HF calorimeters at CMS can be categorized as:

- Vector Boson Fusion (VBF) Higgs search
- Measurement of missing transverse energy (MET), E_T^{miss} .

Vector boson fusion ($qq \rightarrow Hqq$) and gluon fusion ($gg \rightarrow H$), shown in Figure 5.1, are favorable production mechanisms for Standard Model (SM) Higgs boson at the LHC. The decay products of Higgs are detected and reconstructed since Higgs particle can not be detected directly. In the VBF Higgs search, two virtual vector bosons (W^\pm/Z , W^\pm/Z) are radiated from quarks and a Higgs boson is produced from them with two jets alongside. These jets, called forward jets, are reconstructed in the HF calorimeter. So, the precise reconstruction of these forward jets with HF calorimeter plays an important role for the Higgs discovery.

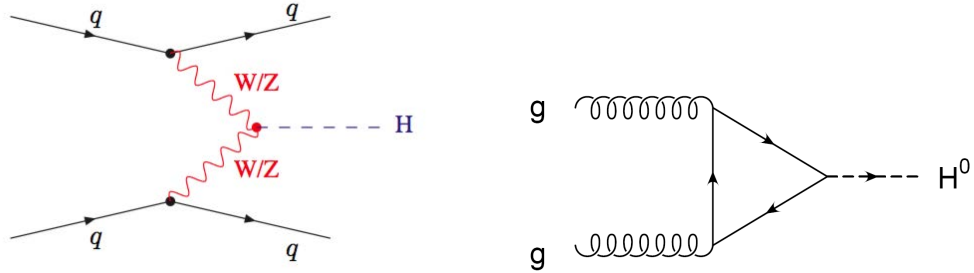
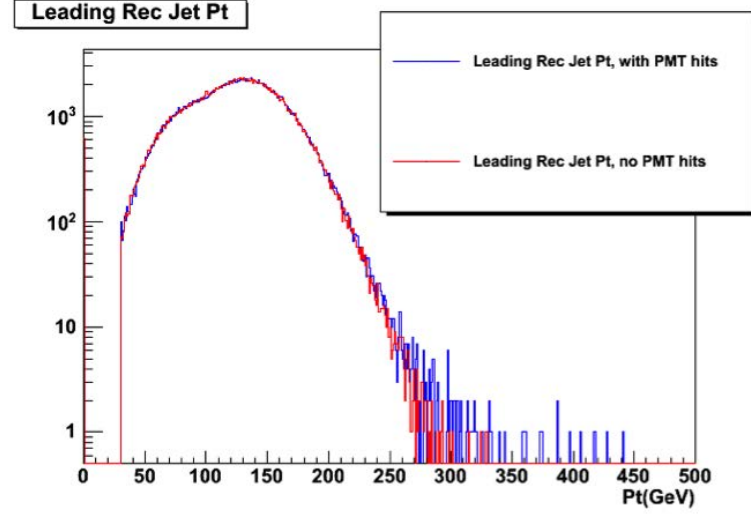
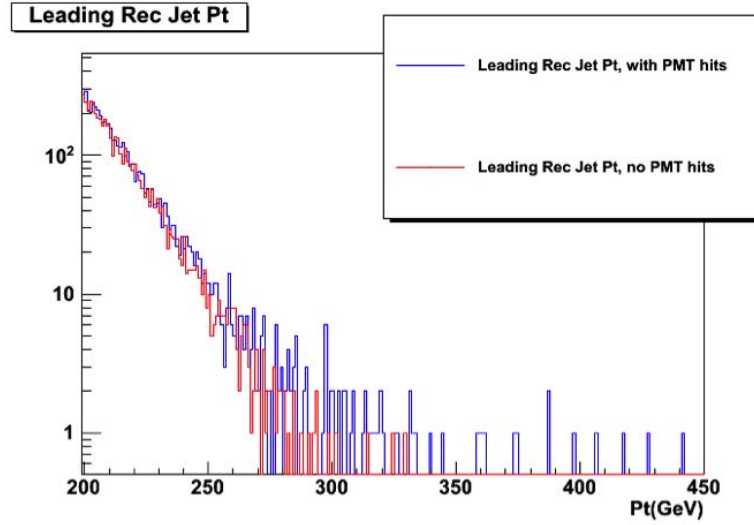


Figure 5.1: Feynman diagram of vector boson fusion Higgs production ($qq \rightarrow Hqq$) on the left and gluon fusion ($gg \rightarrow H$) on the right.

Dr. Moeller at the University of Iowa has simulated (known as PMT simulation) the impact of HF PMT hits on the QCD jets. The result indicated that when the PMT hits were included, there was an increase of QCD background events of about 68% when the p_T of leading jet was higher than 250 GeV. This shows that extra jets reconstructed in HF will lead to increased background in the search for VBF Higgs, shown in Figure 5.2 [81].



(a)



(b)

Figure 5.2: Number of events reconstructed with and without PMT hits as a function of leading reconstructed jet p_T (a) and extended view for the tail (b). Blue distribution indicates results with PMT hits and red without PMT hits (Moeller, 2014).

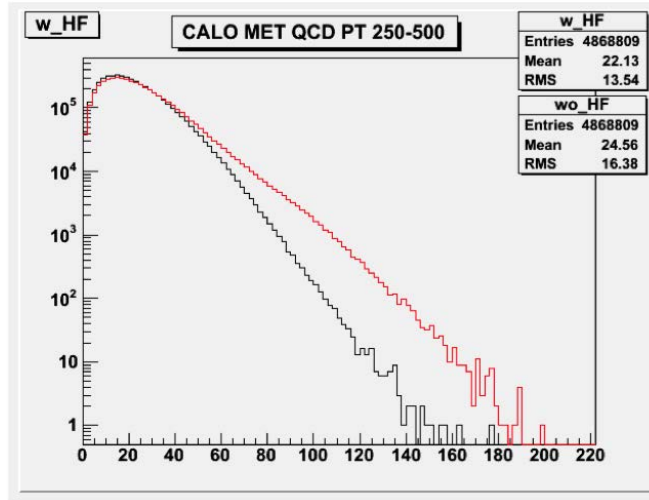
The second physics goal of HF is measurement of the missing transverse energy, MET. This is a primary characterization signature of new physics at the LHC [82]. HF and other hadronic calorimeters at the experiment provide an indirect measurement

of MET, E_T^{miss} due to their sampling nature. Uncharged particles such as neutrinos interact weakly with the matter and no direct response is produced in the detector element. Their presence is perceived from the imbalance of the total momentum at the experiment. The missing vector momentum perpendicular to the beam interaction, \vec{p}_T is known as missing transverse momentum and the total missing momentum in the transverse direction is defined as missing transverse energy (MET), Eq. 5.1 [82].

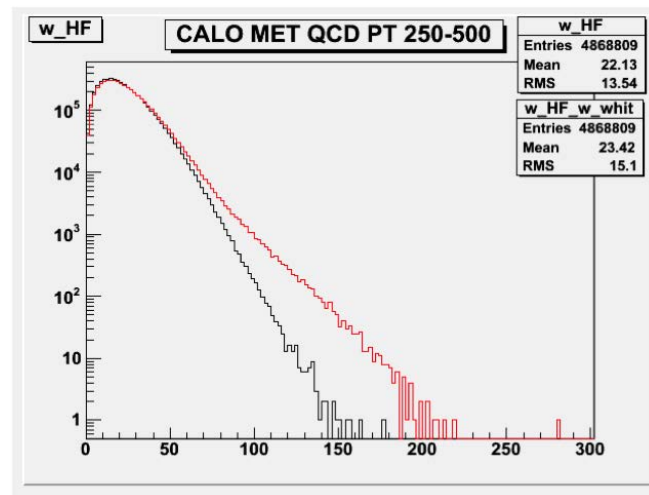
$$\sum_i \vec{p}_T(i) = E_T^{miss} \quad (5.1)$$

Dr. Wetzel at the University of Iowa studied the effect of PMT hits on MET at CMS. As can be seen in Fig. 5.3 (a), MET is noticeably decreased with HF at CMS experiment. The energy measurement with HF calorimeter (black distribution) shows that MET ($\text{MET} > 100 \text{ GeV}$) in the tail of QCD multi-jet events is reduced when compared to without HF calorimeter measurement.

Additionally, MET with and without PMT hits are observed in Fig. 5.3 (b). The distribution with PMT hits (red) shows an increase of MET in the tail of QCD jet events. The old Hamamatsu R7525 PMTs at the HF calorimeter produce Cherenkov light when charged particles pass through their thicker glass windows, which produces a background noise in the experiment resulting an increase of MET.



(a)



(b)

Figure 5.3: Number of events versus MET with and without HF calorimeter and PMT hits. Black distribution is with HF calorimeter hits and red distribution is without HF calorimeter hits in (a) and red distribution is with PMT hits and black distribution is without PMT hits in (b).

5.2 Importance of the Multi-Anode PMTs Replacement

PMTs are extremely sensitive light detectors and they are used to detect photons. A traditional PMT consists of a photocathode (usually coated metals with a

favorable work function), an anode and several intermediate dynodes. The dynodes are electron multiplier sections and they are usually nickel, stainless steel or copper-beryllium alloy that are coated with different emissive materials such as BeO, MgO, GaP and GaAsP. A regular PMT baseboard generates a high potential between the photocathode and anode of the PMT with increasing potentials among dynodes. Electron emission is induced by photons striking the photocathode. These photoelectrons are accelerated toward the first PMT dynode through the potential difference. This knocks secondary electrons from the first dynode and this process is called as secondary emission. Those free electrons are then accelerated into the next dynode, and so forth, creating a cascading amplifying effect. This multiplication process provides the experimenter with enough signal to work with. These sensitive photon detectors convert photons to an electrical signal and that can be recorded in both analog and digital format for further analysis.

PMTs are also used to measure secondary processes as Cherenkov radiation, which is an emitted electromagnetic radiation when charged particles pass through a media. When particles are a lot faster than the phase velocity of light in that media, light waves are generated in a cone shape similar to a sonic boom of a supersonic aircraft. This light boom is called as Cherenkov radiation and it is read out with PMTs in the experiment.

There are a total of 1728 PMTs collecting data in two HF calorimeters positioned at either end of CMS. Hamamatsu single-anode R7525 PMTs were used to collect data during Phase I of the LHC. The proposed replacement is Hamamatsu

multianode, metal package R7600U-200-M4 PMTs, Fig. 5.4, because of the large energy events detected by the previous PMTs, Fig. 5.5. These large energy events are caused by Cherenkov light produced by the glass window of the PMTs when high energy muons from pp collisions and charged particles from late showering hadrons pass through them.



Figure 5.4: Hamamatsu multianode R7600U-200-M4 PMTs and a metal package PMT on the right.

These large energy events in Fig. 5.5 produce an anomalous signal (noise) which results in missing transverse energy (MET). This incident causes problems in trigger rates, luminosity monitoring and minimum bias event triggering. The new multianode PMTs were proposed to overcome the large energy event issue as well as to reduce fake background, thereby make the experiment more efficient. The outstanding features of the new PMTs are:

- A thin ($< 1\text{mm}$) glass window
- A metal envelope to reduce Cherenkov effects on the sides of the glass window

- 38-39% peak quantum efficiency (QE)
- 4 anodes to distribute pattern of light among anodes.

The new PMTs were installed during the first long shutdown (LS1) and they are expected to reduce the impact of charged particles passing through them.

Figure 5.5 shows the beam test results for HF calorimeter at CERN H2 Test Beam Area in 2004. The 200 GeV peak is due to muons interacting with the PMTs and the 4 GeV peak is due to muons interacting with the HF detector itself. The large tail events are due to muons interacting with the glass windows of the PMTs. This muon interactions produce more photoelectrons in the PMTs. This confirms our hypothesis that the Cherenkov interactions in the glass windows of the original HF R7525 PMTs is the cause of excess energy events and those PMTs need to be replaced for improved detector operation.

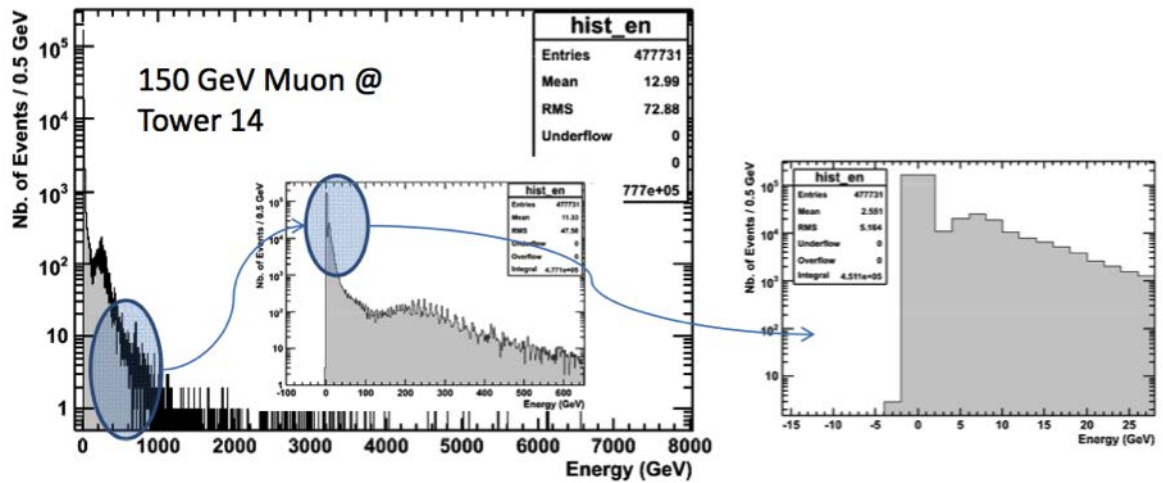


Figure 5.5: Muon response of HF R7525 PMTs in a 150 GeV muon test beam. Extended view on the right shows the lower energy region, 0-25 GeV.

Before the new PMTs are mounted to the CMS detector, their characterization tests need to be done. Since the PMT quality is a major factor for the successful operation of HF calorimeter, CMS Collaboration specifies quality requirements for each PMT in terms of the operation and mechanical design of the HF calorimeter. Table 5.1 indicates the required specifications for old R7525 PMTs and new four-anode R7600U-200-M4 PMTs.

Table 5.1: Specifications for previous and current PMTs for HF calorimeter of the CMS Detector.

Specifications	R7525 (old)	R7600U-200-M4 (new)
Window Thickness	1 mm	0.6 ± 0.4 mm
Photocathode	Bialkali	Super Bialkali
Quantum Efficiency (QE)	25%	38-39%
Gain	$> 10^4$	$> 10^6$
Dark Current	< 2 nA	< 1 nA (per anode at 800V)
Rise Time	< 5 ns	< 2 ns (at 800V)
Pulse Width	< 15 ns	< 15 ns (at 800V)
Transit Time	< 25 ns	< 25 ns (at 800V)
Transit Time Spread	< 2 ns	< 2 ns
Pulse Linearity	$\pm 2\%$ for 1-3000 pe.	$\pm 2\%$ for 1-3000 pe.

All the characterization tests were done at the University of Iowa PMT test station [79,83]. We tested in total 1800 multianode PMTs for gain, dark current, pulse width, rise time, average transit time, transit time spread and single pulse linearity. The detailed experimental setups for the characterization tests can be found in the author's M.Sc. thesis [79].

The statistical uncertainty of gains, dark currents and timing measurements

were determined after retesting the some of the PMTs several times and it was about 10% for all the measurements.

5.3 Gain Measurements

As explained in Section 6.2, the ejected electrons from the metallic surfaces cascade down the PMT and an amplified signal is provided. The gain of a PMT is simply a unit of this amplification measurement. The mean gain here is defined as the ratio of the anode current to cathode current. If the exposed light intensity varies for the anode and cathode measurements, the equation below provides the gain of a PMT. In the equation below, I_a and I_c are anode and cathode currents, and LI_a and LI_c are exposed uniform light intensities on anode and cathode respectively.

$$G = \frac{I_a}{I_c} \times \frac{LI_c}{LI_a} \quad (5.2)$$

The LHC will reach its design center of mass energy of 14 TeV and integrated luminosity¹ of 40 fb⁻¹ per year, which means that a lot more particles will be produced per square centimeter per second. In the CMS experiment, more particles will produce more scintillation light, so high-gain PMTs will play a crucial role to detect the high photon flux. HF calorimeter requires that each PMT should have gain higher than 1×10^6 at 800 V for robust and reliable performance. This limit was designated according to the capability of the readout electronics and expected Cherenkov light

¹40 fb⁻¹ is the total integrated luminosity in one year, which gives a measure of how many collisions occur per square centimeter per second. At LHC in 2010, there was a few million proton collisions per second occurred but with the upgrades, this number is expected to be around 600 million proton collisions per second.

intensity at the forward region of the CMS detector.

Each PMT was tested for gain at the range of operating voltages 600-900 V in increments of 50 V. The data was plotted for each voltage value. The histograms in Fig. 5.6 shows the gain distributions of 1785 multi-anode R7600U-200-M4 PMTs. Table 5.2 summarizes the gain results for all the operating voltages. The mean (RMS) gain of the PMTs is 2.44×10^6 (1.19×10^6) at 800 V, which is higher than the required gain ($> 10^6$) for the new PMTs to have reliable performance with the calorimeter.

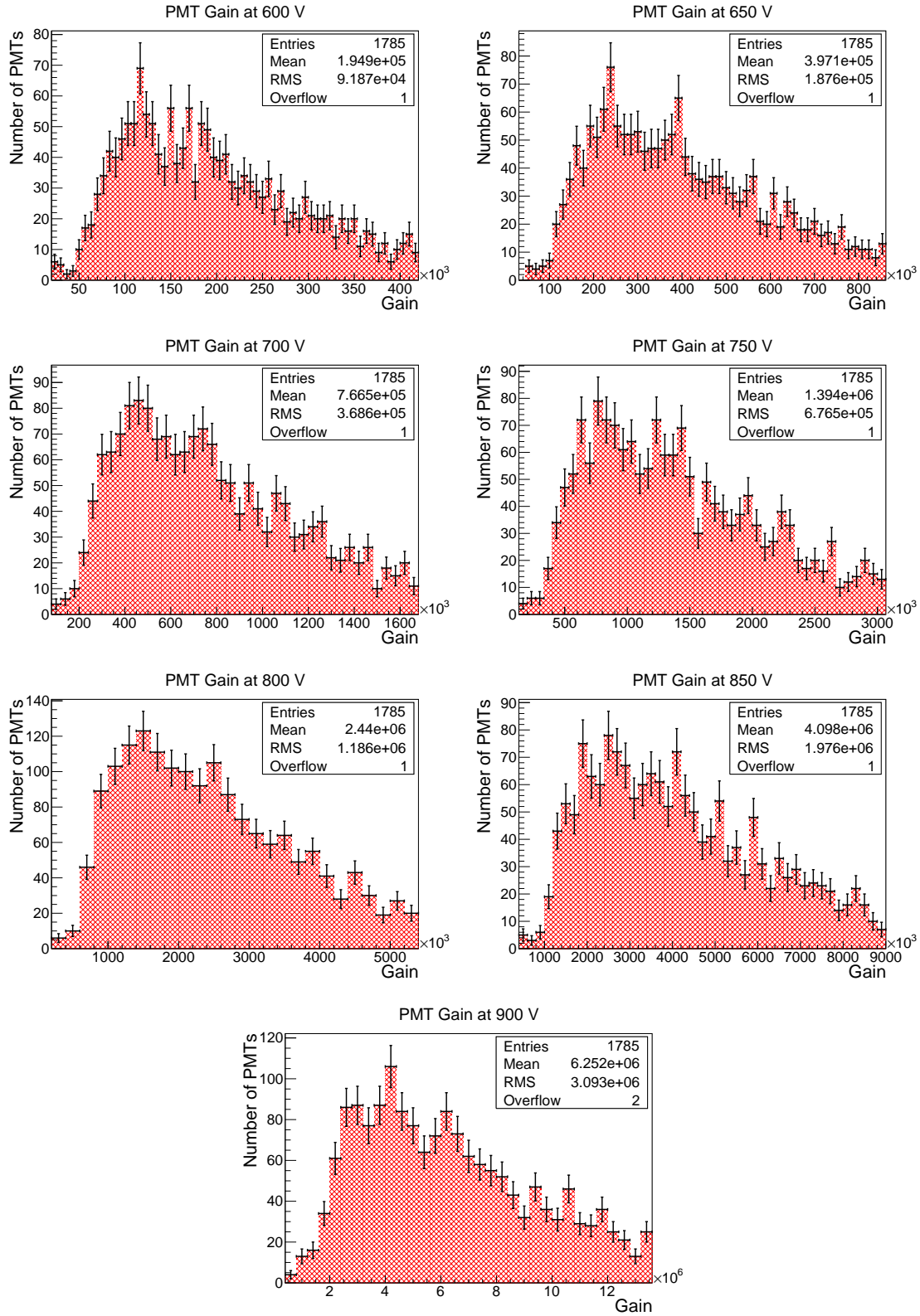


Figure 5.6: Gain distributions of R7600U-200-M4 PMTs at various operating voltages of 600, 650, 700, 750, 800, 850 and 900 V.

Table 5.2: Summary of gain results of R7600U-200-M4 PMTs.

Gains ($\times 10^5$)	Operating Voltages (V)						
	600	650	700	750	800	850	900
Mean	1.949	3.971	7.665	13.94	24.40	40.98	62.52
RMS	0.919	1.876	3.686	6.765	11.86	19.76	30.93

5.4 Dark Current Measurements

Dark current (DC) is a relatively small background current, which is produced by a photomultiplier tube when placed in a light-tight box with no light sources. When the current was settled after some time, the signal was recorded.

Dark current is one of the important parameters for PMTs because comprehensive understanding and control of the residual background is necessary. Dark current is usually caused by thermionic emission of electrons, ionization of remaining gases, leakage currents, contamination and emitted electrons.

Figure 5.7 shows the dark current distributions for 1785 R7600U-200-M4 PMTs. Table 5.3 summarizes the dark current results for all the operating voltages. These results indicate that the majority of the PMTs have dark current below 2 nA at the range of operation voltages 600-800V. At 800 V, the mean (RMS) dark current values are 0.665 (0.770) nA, which is less than the required, 1 nA dark current for the PMTs.

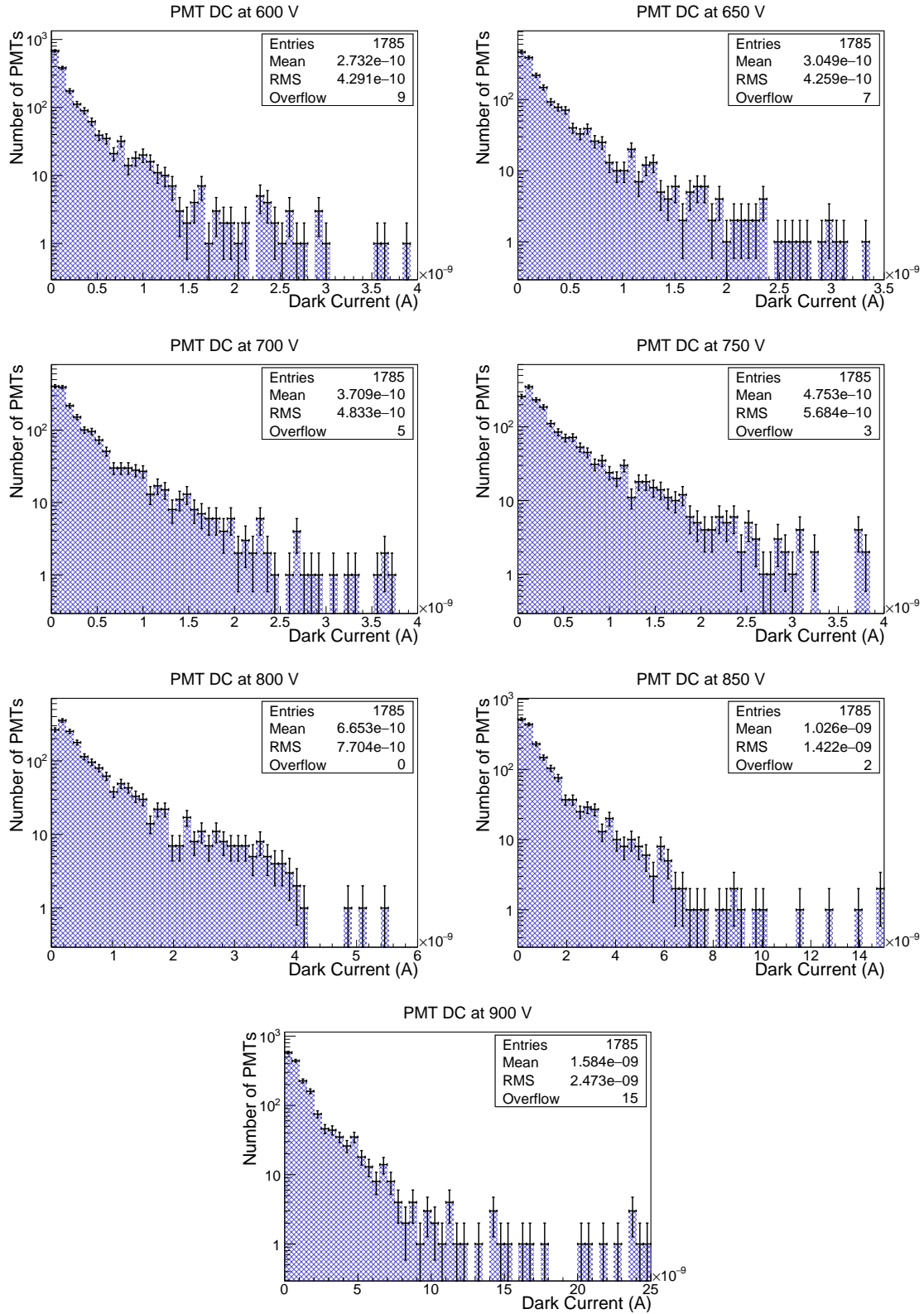


Figure 5.7: Dark current distributions of R7600U-200-M4 PMTs at various operating voltages of 600, 650, 700, 750, 800, 850 and 900 V.

Table 5.3: Summary of dark current results of R7600U-200-M4 PMTs.

DC ($\times 10^{-9}$ A)	Operating Voltages (V)						
	600	650	700	750	800	850	900
Mean	0.273	0.305	0.371	0.475	0.665	1.026	1.584
RMS	0.429	0.426	0.483	0.568	0.770	1.422	2.473

5.5 Timing Measurements

Every PMT type has a different response time, which is determined as the time that passes for the emitted/multiplied photoelectrons to reach the anode. The timing characteristics of a PMT depends on various parameters such as the window type, dynode material and shape, and engineering. Replacing the previous R7525 PMTs with extremely fast time responsive R7600U-200-M4 PMTs is one of the goals of the HF calorimeter upgrade. The time characteristics of the new PMTs need to be studied and characterized accordingly. Here, we tested each PMT for pulse width, rise time, transit time, transit time spread and single pulse linearity.

5.5.1 Pulse Width

It is the full width at half maximum (FWHM) of the amplitude. For the new multi-anode PMTs, the expected pulse width should be lower than 15 ns. Figure 5.8 shows timing distributions of multi-anode R7600U-200-M4 PMTs at 800 V and plot (a) is the pulse width distribution. Table 5.4 shows the mean and RMS of timing characteristics for new PMTs.

The mean (RMS) of pulse width is 5.209 (0.183) ns at 800 V, which is significantly smaller than 15 ns.

5.5.2 Rise Time

This is defined as the amount of time for the output signal to rise from 10% to 90% of its maximum amplitude (peak pulse height). The expected rise time from the new PMTs is 2 ns at maximum. Figure 5.8 (b) shows the rise time distribution for R7600U-200-M4 PMTs at 800 V. The mean (RMS) of rise time is 2.322 (0.120) ns at 800 V. Rise time should be smaller than 2 ns for all the PMTs but the mean is about 2.3 ns, which is 15% higher than the expected limit. Since all the other timing measurements have good agreement with the required specifications, this result would be acceptable and be compensated with fast electronics.

5.5.3 Transit Time

The transit time is the time interval of emitted photoelectrons to travel from cathode to the anode. It is related to supply voltage and dynode structure of the PMTs. Figure 5.8 (c) shows the transit time distribution for R7600U-200-M4 PMTs at 800 V. The mean (RMS) of transit time for 1785 PMTs is 5.496 (0.232) ns at 800 V, which is an extraordinary result comparing to required limit for transit time, 25 ns. The smallness of transit time provides a narrow signal peak with less signal shoulders. This is a perfect result for smooth and stable operation of the HF calorimeter.

5.5.4 Transit Time Spread

There might be fluctuations of transit time between light pulses. The full width at half maximum (FWHM) of the frequency distribution of the transit times is called the transit time spread. We calculate the average transit time of all the PMTs and subtract this value from the each transit time value and the final result gives us the transit time spread. Here, $t_{1 \rightarrow 1800}$ is the transit time and $ts_{1 \rightarrow 1800}$ is the transit time spread, which gives the deviation of all the transit time values.

$$t_1, t_2, \dots, t_{1800}$$

$$a = (t_1 + t_2 + \dots + t_{1800})/1800$$

$$ts_1 = t_1 - a, ts_2 = t_2 - a, \dots, ts_{1800} = t_{1800} - a$$

$$ts_{1 \rightarrow 1800} = t_{1 \rightarrow 1800} - a$$

Figure 5.8 (d) shows the transit time spread for R7600U-200-M4 PMTs at 800 V. The mean (RMS) of transit time spread for these PMTs is 0.132 (0.032) ns at 800 V, which is an exceptional result when compared to the required limit, 2 ns. This result shows that the most of the PMTs have transit time results very close to each other.

5.5.5 Single Pulse Linearity

Single Pulse Linearity is defined as a measure of gain variance corresponding to varying light intensities for a PMT. The output signal was plotted as a function of

light intensity at 800 V for each PMT and the deviation from the linear trend is found. This gives us the correct energy information for each PMT. Figure 5.8 (e) shows the deviation distribution for all the R7600U-200-M4 PMTs at 800 V. The mean (RMS) of the deviation from linearity for 1785 PMTs is 0.357 (0.091)% at 800 V. Since all the PMTs have a deviation less than 1%, we conclude that PMTs respond in a very linear manner with increasing light intensity and they demonstrate good agreement with expectations.

Table 5.4 summarizes the timing results of all the new multi-anode PMTs at 800 V.

Table 5.4: Summary of timing characteristics of R7600U-200-M4 PMTs.

	at 800 V				
	Pulse Width (nsec)	Rise Time (nsec)	Transit Time (nsec)	TT Spread (nsec)	Pulse Linearity (%)
Mean	5.209	2.322	5.496	0.132	0.357
RMS	0.183	0.120	0.232	0.032	0.091

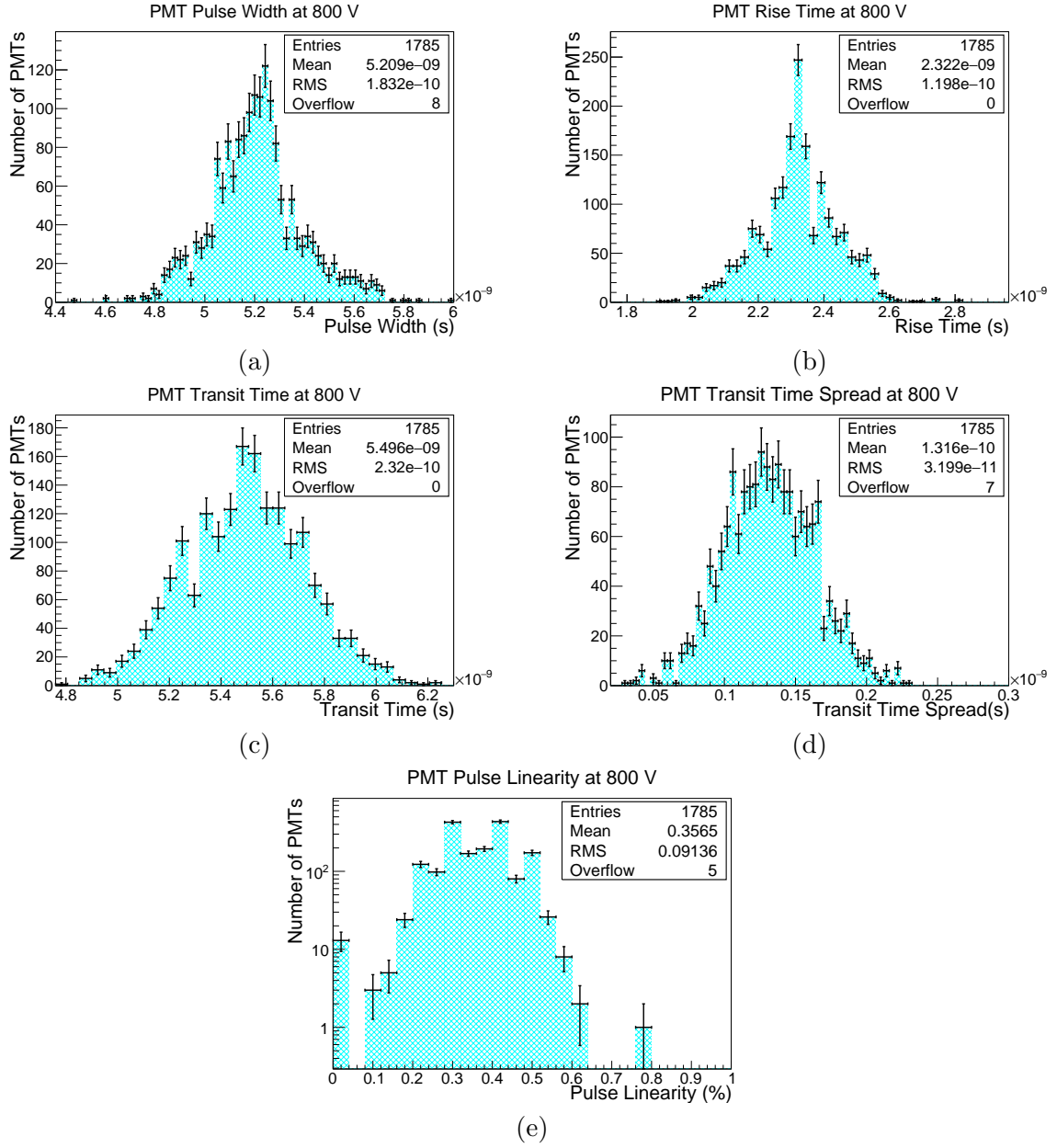


Figure 5.8: Timing distributions of R7600U-200-M4 PMTs at 800 V. (a) is pulse width, (b) is rise time, (c) is transit time, (d) is transit time spread and (e) is pulse linearity distribution.

5.6 Summary of the PMT Results

The PMTs which performed well and passed the characterization tests were categorized in terms of their characterization results and shipped to CERN to be mounted on the detector. Only 30 PMTs out of 1785 PMTs (1.7%) were rejected and sent back to the company. Overall, the selected PMTs have low dark current, high-gain and fast timing characteristics.

The High Energy Physics (HEP) group at the UI also tested a readout box (RBX) prototype with a beam test at Fermilab and organized the installation of the PMTs into the HF calorimeter according to their gain results. In the HF calorimeter, the towers, which are close to the beam interaction point (IP) are exposed to more particles (that produces more scintillation light in the tower) than the towers far from the IP. So, PMTs with higher gains were installed into those towers close to the IP. After they were all installed, they started to be used for data collection and reconstruction of collision events. The characterization results will provide insights about the expected performance of the CMS-HF detector.

CHAPTER 6

SECONDARY EMISSION IONIZATION CALORIMETRY

Hamamatsu single anode R7761 and multi-anode R5900-00-M16 Photomultiplier Tubes have been characterized for use in a Secondary Emission (SE) Ionization Calorimetry study. SE Ionization Calorimetry is a novel technique to measure electromagnetic shower particles in extreme radiation environments. The different operation modes used in these tests were developed by modifying the conventional PMT bias circuit. These modifications were simple changes to the arrangement of the voltage dividers of the baseboard circuits. The PMTs with modified bases, referred to as operating in SE mode, are used as an SE detector module in an SE calorimeter prototype, and placed between absorber materials (Fe, Cu, Pb, W, etc.). Here, the technical design of different operation modes, as well as the characterization measurements of both SE modes and the conventional PMT mode are reported¹.

6.1 Introduction

The increasing instantaneous luminosity and resulting unprecedented radiation conditions at particle accelerators, such as the Large Hadron Collider (LHC), necessitate a major detector transformation in order to maintain/improve physics measurement capabilities. These highly demanding experimental conditions require radiation-hard detectors and calorimeters for robust and reliable performance. In this

¹This study was published in JINST in 2016 by the author. This chapter in this thesis was included from Ref. [84].

context, we have studied Secondary Emission [85] (SE) Ionization Calorimetry as a new, novel particle calorimetry technique in high radiation environments. Since there are no dedicated secondary emission modules commercially available, we developed adaptations in the biasing modes of photomultiplier tubes (PMTs) to demonstrate the secondary emission mechanism in the dynode chain and the possibility to use such detectors in calorimetry.

Traditional PMT baseboards create a high potential difference between the photocathode of the PMT (usually coated metals with a favorable work function) and the anode of the PMT, with several intermediate dynodes at increasing potentials in between. A photon striking the photocathode induces electron emission. Those electrons are then accelerated through the potential difference directly into the next PMT dynode. This knocks more free electrons, which are accelerated into the next dynode, and so forth, creating a cascading amplifying effect. This amplification process provides the experimenter with sufficient signal to detect a single photon.

In an SE module, Secondary Emission electrons (SEe) are generated from an SE surface, cathode or dynodes, when charged particles (shower particles) penetrate the module [86,87]. An SE cathode is a thin film. These films are typically simple metal-oxides Al_2O_3 , MgO , CuO/BeO , or other higher yield materials. These materials are known to be very radiation-hard, as they are used in PMTs (up to 50 Grad dose) and in accelerator beam monitors (flux of $>1020 \text{ MIP/cm}^2$).

On the inner surface of a metal plate in vacuum, which serves as the entrance "window" to a compact vacuum vessel (metal or metal-ceramic), an SE film cathode is

analogous to a photocathode, and the shower particles are similar to incident photons. The SEe produced from the top SE surface by the passage of shower particles, as well as the SEe produced from the passage of the shower particles through the dynodes, are similar to photoelectrons. The statistics of photoelectrons and SEe are similar. The SEe are then amplified by sheets of dynodes.

By observing the intrinsic similarities of the PMTs and the envisaged SE modules, a PMT can be used to validate the concept of an SE module with simple modifications. In order to validate this approach, we started with conventional PMTs. The PMTs were selected such that they had excessive usage, hence had potentially degraded photocathode performance. Although it would be ideal to be able to use the photocathode as an SE film cathode mentioned above, the contributions from the Cerenkov photons created at the glass entry window of the PMT cannot be prevented and would bias the SE measurements. Therefore, the validation procedure consists of disabling the photocathode from the multiplication chain rendering the PMT non-responsive to photons incident on the photocathode. In this case, the entire dynode chain is utilized as SE surfaces. The largest contribution comes from an initial SEe production at the first dynode.

In order to study the effects of multiple schemes in disabling the photocathode, we developed two modules. The first module was constructed with seven Hamamatsu single anode R7761 and the second one with nine Hamamatsu 16 pixel R5900-00-M16 multi-anode photomultipliers [88]. For the former, two different SE modes are developed in order to observe the effect of secondary emissions. One mode is the

so-called ‘cathode float’ (CF) mode, where the photocathode is removed from the signal chain. The other mode is the so-called ‘cathode/first dynode shorted’ (C-D1) mode, where the photocathode is included in the signal chain. For the multi-anode tubes, we have only developed the C-D1 mode. This is due to the fact that the multi-anode PMTs have metal channel dynode structure which has a significantly smaller fraction of the area of the photocathode. By applying C-D1 mode, cathode to D2 multiplication is enabled to some extent.

We can also operate the PMTs in the traditional (PM) mode. For the two different PMT types, two different circuit boards were developed to power them in all mentioned modes. Each PMT was tested for gain and dark current in both PM and SE modes.

Here, we report on the technical design of SE operation modes and measurements performed on 74 PMTs. These tubes are used in a later calorimetric measurement study to be published as a separate article.

6.2 Technical Design

The Hamamatsu single anode R7761 PMT has a bialkali photocathode material with borosilicate glass and it has 19 dynode stages that are secondary emissive electrodes in a fine mesh structure. The 16 anode R5900-00-M16 PMT has the same photocathode and window materials but metal channel dynode structure as the multiplication chain. The dynodes of both PMT types are either nickel, stainless steel or copper-beryllium alloy that are coated with different emissive materials such as BeO,

MgO, GaP and GaAsP. Both PMT types were previously used for collecting data in the CDF experiment at Fermi National Accelerator Laboratory (Fermilab) [89–91].

A circuit board was designed to power seven Hamamatsu R7761 tubes with negative high voltage (Fig. 6.1 left). Each tube was powered by a common voltage divider located on the board. The values for this voltage divider are chosen following the reference design by Hamamatsu.

Figure 6.1 right shows the bases for powering each Hamamatsu R5900-00-M16 PMT. The assemblies shown in Fig. 6.1 were primarily constructed for the SE calorimeter tests.

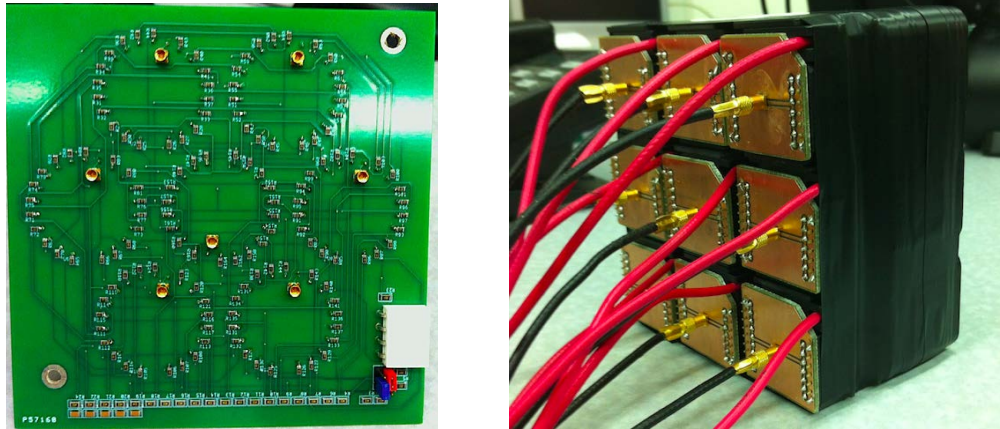


Figure 6.1: Circuit boards for powering R7761 and R5900-00-M16 PMTs. Seven R7761 PMTs are powered with circuit boards on the left and each R5900-00-M16 PMTs are powered separate bases on the right. Both designs have switches/jumpers to select the mode of operation.

Figure 6.2 shows the schematic of the voltage divider for the R7761 baseboard. The values of resistors R2-R20 are chosen such that they follow closely the reference

design from Hamamatsu for negative high voltage operation, and provide a linear voltage divider. Despite depletion of the photocathode and considering the population of the board, base current is only slightly increased over the nominal single-socket reference current operating at about $300\mu\text{A}$. To mitigate standing current depletion during pulses with multiple photomultiplier tubes, capacitors C1-C5 are added to store charge for the final dynodes. Finally, R_i is used to attenuate noise introduced from the high voltage supply.

Three different modes of operation exist on the baseboard for R7761 PMTs:

Mode 1 - normal divider or PM mode: In this mode, the voltage divider chain is unmodified and the potential difference seen across the dynodes is equal, with the exception for 2x potential across the C-D1 gap. This is the reference design from Hamamatsu.

Mode 2 - cathode-first dynode (C-D1) shorted: In this mode, jumpers on the board enable the bridging of R1, so that there is 0 potential across the C-D1 gap ($V_C - V_{D1} = 0\text{V}$).

Mode 3 - cathode separated, cathode independent or cathode float mode: The design of the board allows the cathode to be separated from the remainder of the divider chain. A second voltage input to the baseboard allows specific tuning of the voltage present on D1. With proper jumper selection and two high voltage sources, the potential across the C-D1 gap can be manipulated such that it becomes positive with respect to the gap of D1-D2. In this mode, if a second high voltage source is not used, there is a slight possibility that the photocathode can still be

charging up. Previous tests with a single R7761 and a positive high voltage base applying +2kV to the anode and a few hundred volts to the cathode keeping D1 at ground were performed. The cathode positive voltage was varied slowly down to ground and there was no notable change in response to beam particles. In any case, Mode 3 is not the foreseen operation mode for a future, dedicated SE detector. It serves as a comparison tool in the framework of this study.

All of these modes can be examined in Fig. 6.2, where A-B bridge forms normal operation mode (Mode 1) with HV input on HV1, B-C bridge forms Mode 2 with HV input on HV1, and B-D bridge forms Mode 3 with HV input on HV2.

There are only two different modes of operation for the baseboards of R5900-00-M16 multi-anode PMTs: Mode 1 and Mode 2. The schematic diagram of the secondary emission voltage divider for R5900-00-M16 is shown in Fig. 6.3. The A-B bridge forms Mode 1 and the B-C bridge forms Mode 2, both with HV input on HV1.

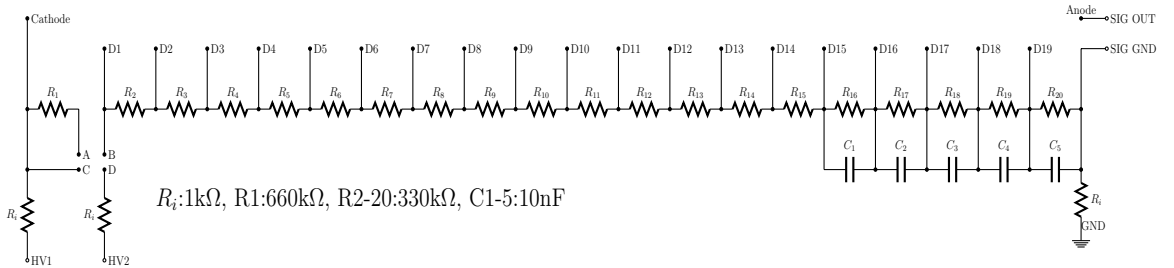


Figure 6.2: Schematic diagram of the secondary emission baseboard common voltage divider for R7761 PMTs.

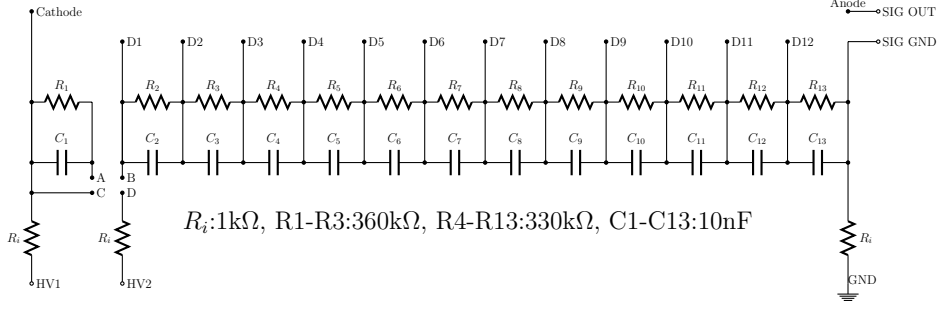


Figure 6.3: Schematic diagram of the secondary emission voltage divider for R5900-00-M16 PMTs.

6.3 Laboratory Measurements and Results

The PM and SE mode characterization tests were done at the University of Iowa PMT test station [79,83]. All the tests were performed in light-tight boxes. Each anode of the R5900-00-M16 multi-anode PMT was tested for response uniformity. A 20 Hz, 337 nm nitrogen laser was used as a source with a neutral density filter and the light was transmitted to the window of the PMT by a 1 mm diameter wavelength shifting optical fiber. The fiber was placed at the center of each anode and the measurements were taken across all 16 anodes.

Figure 6.4 shows the response uniformity measurement for a R5900-00-M16 PMT. The responses were normalized to that of anode 11. The non-uniformity is measured to be less than 3%. This result shows that the variation of sensitivity across the effective area of multianode PMTs is low enough to be considered as active layers in calorimetric measurements with beams.

For the dark current measurements, each PMT was placed in a light-tight

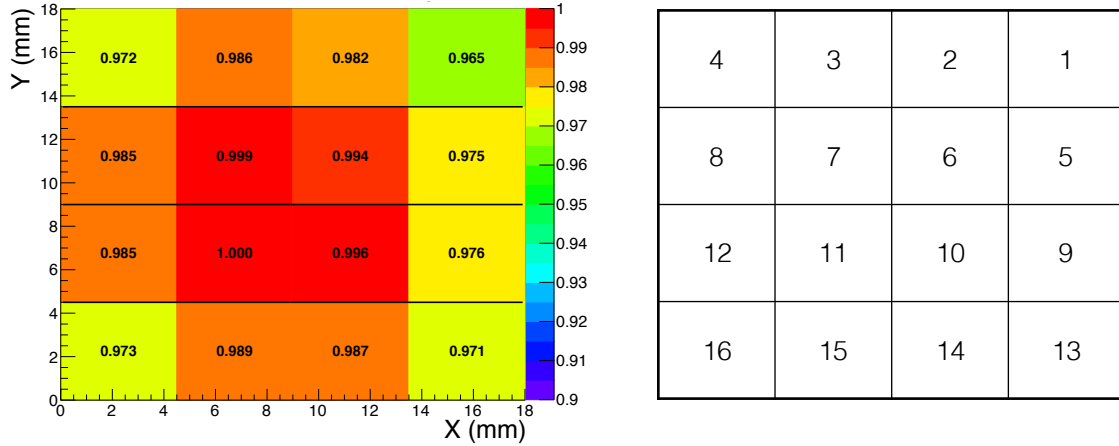


Figure 6.4: The response uniformity of R5900-00-M16 PMTs (left) as light incidence on channels 1-16, respectively. Right is the top view of R5900-00-M16 PMT, the integers indicate the channel numbers.

box, and the anode current is read out by the Keithley-6485 picoammeter right after the current was settled. The dark current distributions for both single anode R7761 PMTs and multi-anode R5900-00-M16 PMTs show that the majority of the PMTs have dark currents below 1 nA at the range of operation voltages 1500-2000 V and 800-1200 V respectively, for all the different operation modes.

The anode and cathode currents at various light intensities were measured in a light tight box and gains were calculated for both PMT types in all modes. The purpose of the measurements is to obtain a relative gain for the SE modes, i.e. for multiplication starting at D1 instead of the photocathode, in comparison with the conventional PMT mode. In these tests, uniformly distributed light pulses are used to illuminate the PMT window. A tungsten light in the opposite end of the light-tight box is used as a light source. A neutral density filter, which reduces the light intensity to the desired level, and a light diffuser, which distributes the light uniformly through

the face of the PMT, are used in the upstream direction of the PMT. Since there is no natural way of initiating a multiplication chain such as thermal excitation, we tried to forcefully generate a photoelectron from the photocathode with a light source and have it multiplied with the modified bias arrangement.

Figure 6.5 shows the gain distributions of R5900-00-M16 PMTs in Mode 1 and Mode 2 at 800, 1000 and 1200 V. This is the total gain of all 16 anodes. Table 6.1 summarizes Mode 1 and Mode 2 gains (Mean and RMS). The performance of Mode 2 at 1000 V with an average gain of 16×10^5 is comparable to the gain of Mode 1 at 800 V. The decrease in the gain due to the smaller number of steps in the multiplication chain can be roughly compensated with an increase of 200 V in the operating voltage. As the gain of Mode 2 rises to the Mode 1 levels, the spread of the gains across different Mode 2 PMTs gets smaller. This is an indication that with the combination of the stable, dedicated SE modules and the correct operating conditions, large sizes of calorimeters based on SE principle can be constructed.

Figure 6.6 shows the gain distributions of R7761 PMTs in Mode 1, Mode 2 and Mode 3 at 1500, 1800 and 2000 V. Table 6.2 summarizes gains (Mean and RMS) of all mentioned modes. The performance of Mode 2 is almost identical to Mode 1 at the range of operation voltages 1500 - 2000 V. The advantage of the mesh dynode structure over the metal channel structure is clearly visible. The geometry and size of the metal channels further constrain the favorable location of the first SEe, hence a larger voltage difference is needed to compensate for this effect. On the other hand, the mesh dynodes constitute a more uniform surface (like the photocathode).

Therefore, the gains in Mode 2 are comparable to Mode 1 in contrast with R5900-00-M16 PMTs.

The significantly lower gain of Mode 3 is understood to be due to some of the SEe not being able to reach D2 and be amplified in the dynode chain. Here, the relative electric field between the floating cathode and D1, and between D1 and D2 play an important role. Even small fluctuations seem to yield lower gains. The performance of Mode 3 at 2000 V with a gain of 5.72×10^5 is hardly comparable to those of Mode 1 and Mode 2 at 1500 V.

The statistical uncertainty of gains and dark currents were determined after retesting the same PMTs several times and it was about 10% for both gain and dark current measurements.

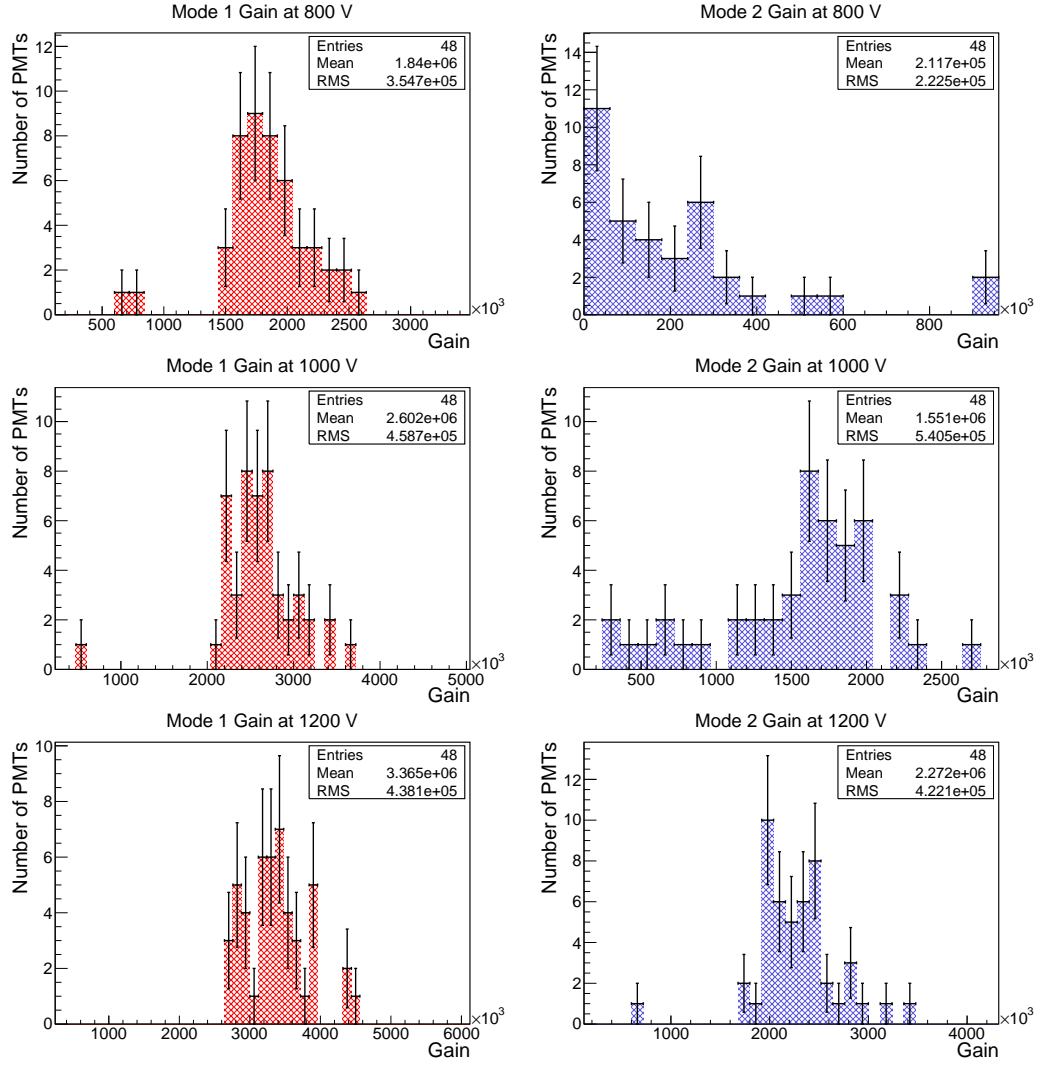


Figure 6.5: Gain distributions of R5900-00-M16 PMTs in different modes. Left column is Mode 1 results and right column is Mode 2 results for R5900-00-M16 PMTs at 800 V (top row), 1000 V (middle row) and 1200 V (bottom row).

Table 6.1: Summary of gains for Mode 1 and Mode 2 of R5900-00-M16 PMTs.

Gains ($\times 10^5$)	800 V		1000 V		1200 V	
	Mean	RMS	Mean	RMS	Mean	RMS
Mode 1	18.4	3.55	26.02	4.59	33.65	4.38
Mode 2	2.12	2.23	15.51	5.41	22.72	4.22

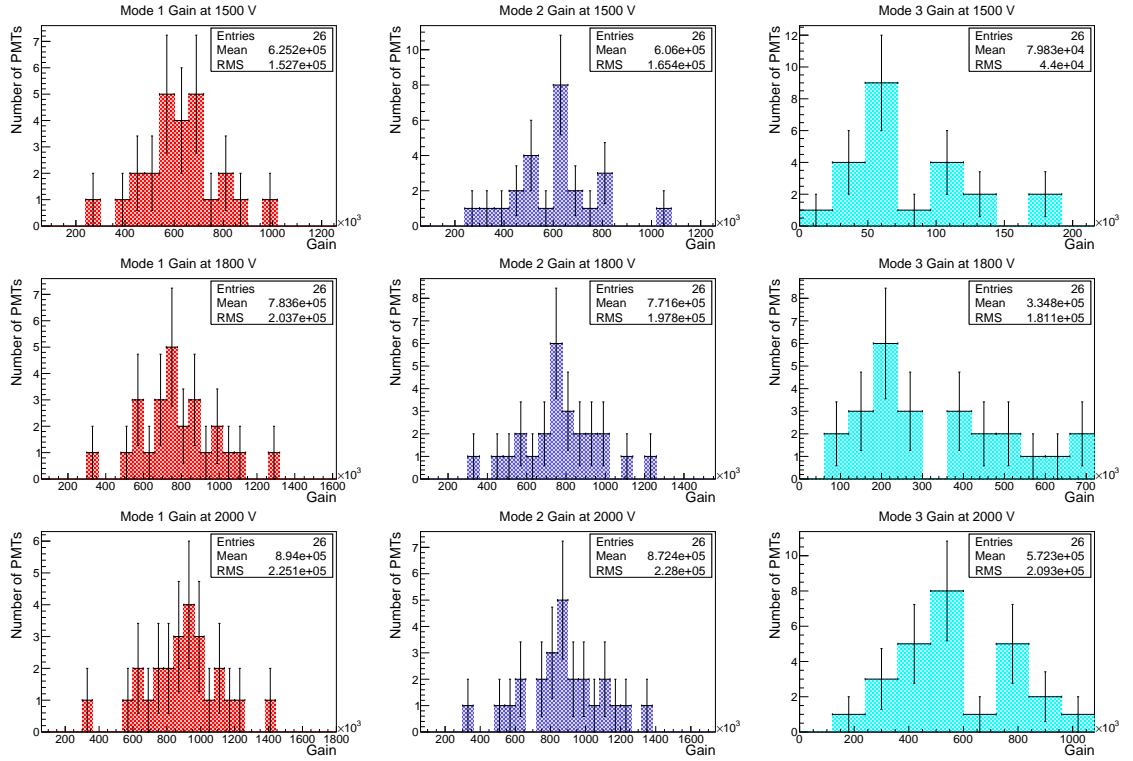


Figure 6.6: Gain distributions of R7761 PMTs in different modes. Leftmost column is Mode 1 results, middle column is Mode 2 results and rightmost column is Mode 3 results for R7761 PMTs at 1500 V (top row), 1800 V (middle row) and 2000 V (bottom row).

Table 6.2: Summary of gains for Mode 1, Mode 2 and Mode 3 of R7761 PMTs.

Gains ($\times 10^5$)	1500 V		1800 V		2000 V	
	Mean	RMS	Mean	RMS	Mean	RMS
Mode 1	6.25	1.53	7.84	2.04	8.94	2.25
Mode 2	6.06	1.65	7.72	1.98	8.72	2.28
Mode 3	0.80	0.44	3.35	1.81	5.72	2.09

6.4 Conclusion

We developed secondary emission readout modes as a simple bias modification in the voltage dividers of photomultiplier tubes with mesh and metal channel dynode structures. In the first secondary emission module, seven single anode Hamamatsu R7761 PMTs were powered by a dedicated circuit board, which can be operated in three different modes; normal divider (Mode 1), cathode-first dynode shorted (Mode 2) and cathode float mode (Mode 3). The second secondary emission module was produced with nine multianode Hamamatsu R5900-00-M16 PMTs, powered by separate bases, which can be used in two different modes; normal divider (Mode 1) and cathode-first dynode shorted mode (Mode 2). Both PMT types run smoothly in both traditional PM and SE modes, even after being used to collect data at the CDF experiment at Fermilab for several years. All the PMTs have low dark currents, below 1 nA for all the different operation modes. The multianode PMTs have a response non-uniformity of less than 3% across the anodes. Average gain for the R5900-00-M16 in Mode 1 is $15\text{-}30 \times 10^5$ and in Mode 2 is $2\text{-}20 \times 10^5$ for the range of operating voltages

800-1200 V. Average gain for R7761 is $6-9 \times 10^5$ both for Mode 1 and Mode 2, and in Mode 3 is $1-6 \times 10^5$ for the range of operating voltages 1500-2000 V. Both modules are operating stably and can serve as active layers in calorimetric measurements with beams in order to validate the concept of secondary emission calorimetry.

CHAPTER 7

RADIATION HARD SCINTILLATING MATERIAL SEARCH

The increase in energy at particle physics experiments offers an excellent opportunity to disclose the properties of the exotic particles and discover new particles beyond the Standard Model (SM). However, this results in more radiation and requires more radiation resistant, sensitive, and fast scintillating materials. In this regard, we¹ have investigated various scintillating materials for radiation hardness, timing and light yield characteristics². While the primary goal of this study is geared for Large Hadron Collider (LHC) detector upgrades, these new technologies could easily be used for future experiments such as Future Circular Collider (FCC) and International Linear Collider (ILC).

The LHC will reach up to ten times its original design luminosity ($5 - 10 \times 10^{34} \text{cm}^{-2} \text{s}^{-1}$) resulting in unprecedented radiation conditions in a collider experiment [98]. The CMS Hadronic Endcap (HE) calorimeters covering pseudorapidity between 1.6 and 3 will need to be replaced with a high granularity calorimeter and a backing hadron calorimeter during Phase II upgrades in order to maintain and improve the superior performance of CMS. The backing hadron calorimeter will have scintillator tiles as active media, and either directly couple the tiles to photodetectors

¹This study was completed in collaboration with Dr. James Wetzel and Dr. Burak Bilki under the supervisions of Prof. Yasar Onel at the University of Iowa and Prof. David Winn at Fairfield University.

²The results of this study were published as two journal articles [92, 93] and several conference proceedings [94–97]. Some parts of this chapter were included from these publications.

or utilize wavelength shifting (WLS) fibers. With these research and development (R&D) studies on novel scintillating materials, we attempted to identify the most suitable active media and readout options for this upgrade. However, the extent of the R&D is not limited to future CMS upgrades but can find implementation areas in future collider detector experiments and in facilities where measurements in high radiation areas are crucial.

7.1 Novel Scintillating Materials

We have studied radiation-hard quartz plates with various scintillating coatings. For quartz, the signal generation produced by Cherenkov radiation is insufficient. The solution developed to overcome this issue is coating quartz plates with organic and inorganic scintillators such as para-Terphenyl (pTp), Anthracene (AN) and Gallium-doped Zinc Oxide (ZnO:Ga) in order to enhance the light yield.

Organic scintillators; pTp and AN are aromatic hydrocarbons with three benzene rings (C_6H_6) formed. They exhibit blue fluorescence under ultraviolet (UV) light. Vacuum deposition is used for coating pTp, Fig. 7.1 (a) and RF sputtering technique is used for coating AN on the quartz plates, Fig. 7.1 (b) [94].



Figure 7.1: Para-Terphenyl (pTp) evaporation (a) and Anthracene (AN) sputtering (b) on quartz plates [94].

The radiation hardness of pTp was tested with proton beams at CERN and at the Indiana University Cyclotron Facility (IUCF). The light yield of the pTp sample dropped to 84% of the initial light yield after 20 Mrad proton irradiation, and 80% of the initial light yield after 40 MRad proton irradiation [99].

Inorganic scintillators such as ZnO:Ga is also deposited on quartz plates to increase light yield. It has a short de-excitation time of 0.7 ns and very high luminous yield of 15k photons/MeV [100].

In addition to quartz plates, we have investigated intrinsically radiation-hard and cheap plastic scintillators such as Polyethylene Naphthalate (PEN), Polyethylene Terephthalate (PET), a lab produced scintillator (SiX) [101] and other scintillators such as High Efficiency Mirror (HEM), Kuraray brand SCSN-81 (HE), and Eljen brand EJ-260 (EJN) and overdoped version, EJ-260 (EJ2P).

PEN was created by the Japanese company Teijin Chemicals [102]. The com-

pany initially produced a sample in a size of 5 mm x 35 mm x 35 mm and measured its light yield as 10,500 photons per MeV. PEN produces intrinsically blue scintillation, as can be seen in Fig. 7.2 with a peak emission spectrum of 425 nm [94, 103]. PET is a common type of polyester and it is widely used to make plastic bottles and as a substrate in thin film solar cells. The emission spectrum of PET peaks at 385 nm and it produces 2,200 photons per MeV [103].

PEN scintillators have been used in radiation dosimeters in nuclear experiments and medical physics [104] but neither PEN nor PET have been used in particle physics experiments.

Another radiation-hard material is HEM, which is structurally a multi-layer of polymer mirrors. We have made a stack of alternating slices of HEM sheet and quartz plates and tested the scintillating properties of the stack.

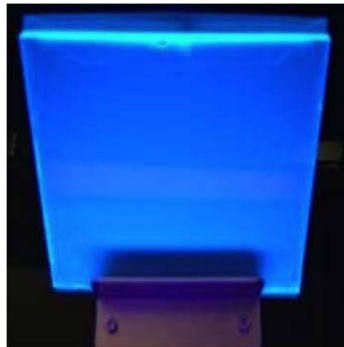


Figure 7.2: The intrinsic blue scintillation of PEN [94].

HE, EJN and EJ2P scintillators are materials known to the CMS collaboration so we tested and used them as control samples (baseline) for comparison purposes.

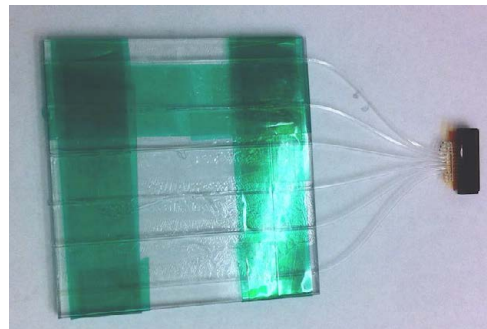
7.2 Laboratory Measurements

Various tiles were prepared and their radiation hardness, timing characteristics, scintillation and transmission properties were studied at the high energy physics (HEP) laboratory at the University of Iowa.

Different geometries and different readout methods such as silicon photomultipliers (SiPM) and photomultiplier tubes (PMTs) were also tested to identify the most suitable active media and readout options. Scintillator tiles were either directly coupled to photodetectors or indirectly coupled through an optical fiber, usually wavelength shifting fibers (WLS). WLS fibers are inserted into the tiles with either sigma or bar shaped grooves. Figure 7.3 shows different tiles' groove geometries [94].



(a)



(b)

Figure 7.3: Different geometries, sigma and bar shape grooved scintillators. Picture of sigma shape grooved tile with one WLS fiber (a) and a bar shape grooved tile with several WLS fibers (b) [94].

7.2.1 Scintillation and Transmission Measurements

Scintillation and transmission measurements of HE and PEN tiles were done with two different experimental setups. For transmission spectrum analysis, a scintillator tile was pulsed with Ocean Optics PX-2 xenon light source (220 - 750 nm emission) [105], and the light through the tile is carried to the spectrometer (200nm - 1100nm input range) by an optical fiber, Fig. 7.4 (a). The analyzed spectra are the average of 100 xenon lamp pulses.

For scintillation light yield measurement, a scintillator tile was stimulated with a 334 nm wavelength nitrogen UV laser and the stimulated emission through a WLS optical fiber was read out with a PMT (Hamamatsu R7525), Fig. 7.4 (b). The PMT was powered at 1800 volts (V) and the signal was recorded using a Tektronix TDS 5034 digital oscilloscope [106]. For every measurement, 50 waveforms, triggered by 50 laser pulses, were averaged and the average waveform was saved. All the experiments were done in a light-tight box and at a constant room temperature, 22.5 °C.

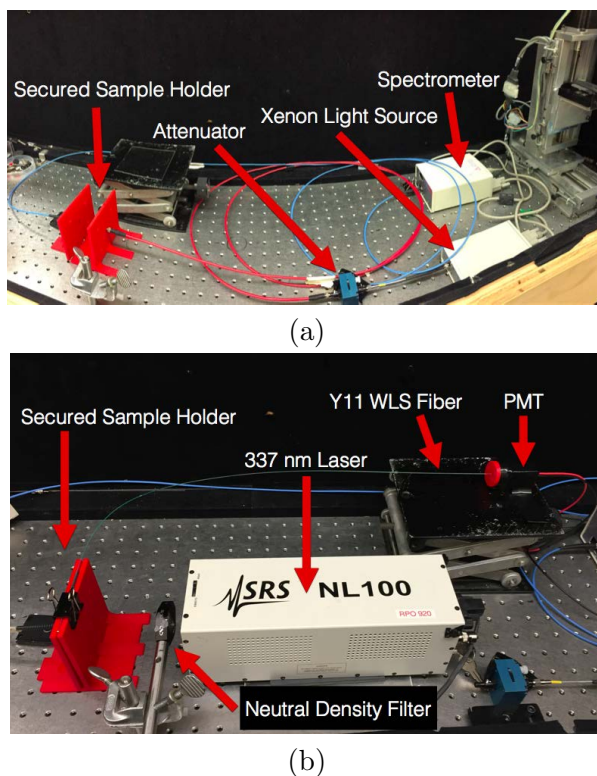


Figure 7.4: Scintillator transmission spectrum setup (a) and scintillation light yield setup (b).

Three 5 cm x 5 cm x 0.1 cm PEN samples were prepared and two of them placed into FoodSaver[®] freezer bags. One of the samples in the bag was placed in an N_2 filled glass pressure vessel and sealed, Fig. 7.5 and other sample was left in air. One sample was kept in the laboratory as a baseline for further calibration studies.

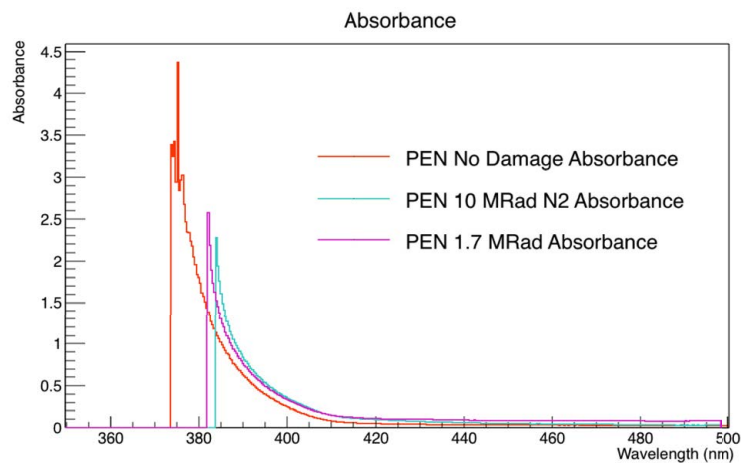


Figure 7.5: PEN sample before irradiation in a vacuum bag.

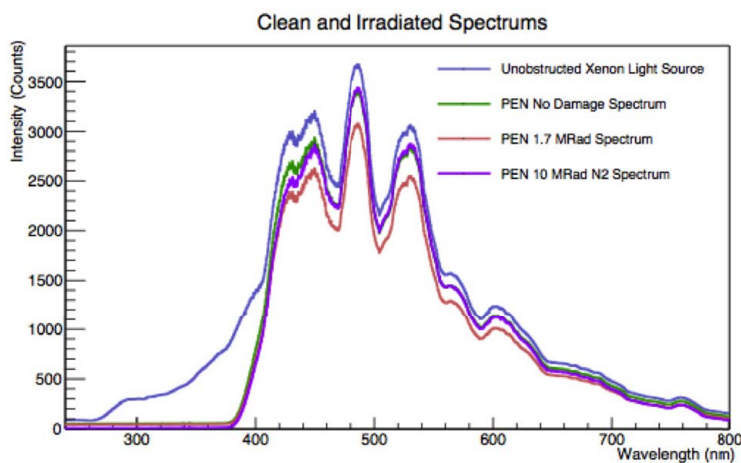
Two samples, one filled with N_2 and one filled with air were exposed to a ^{60}Co radiation source at the University of Michigan. The sample in the N_2 vessel was irradiated to 10 Mrad, while the air sample was irradiated to 1.7 Mrad.

Upon return, all the samples were tested for absorption, scintillation and transmission properties. Figure 7.6 shows the absorption spectrum (a), luminescence spectrum (b) and transmission spectrum (c) as a function of wavelength for all PEN scintillators. Two irradiated samples, in air and in N_2 , showed similar effects. The radiation damage changed their absorption spectrum slightly. They absorbed less light and in a narrower wavelength than the undamaged sample, Fig. 7.6 (a).

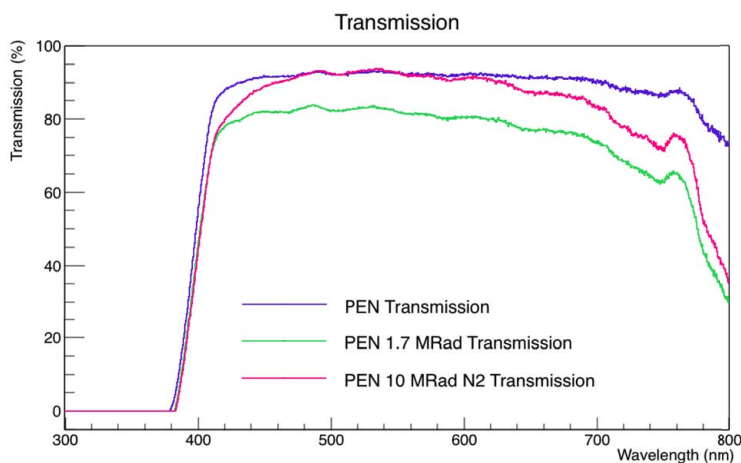
In terms of the luminescence spectrum, there is a small radiation effect on the samples. The baseline, unirradiated tile indicates slightly better light intensity versus wavelength behavior than irradiated tiles, Fig. 7.6 (b).



(a)



(b)



(c)

Figure 7.6: Absorption spectrum (a), luminescence spectrum (b), and transmission spectrum (c) of the unirradiated and irradiated PEN samples.

As can be seen in Fig. 7.6 (c), the transmission of the damaged PEN samples show that being in a nitrogen atmosphere has a protective effect overall on the PEN sample compared with irradiation in ambient atmosphere, but in particular over the wavelengths of approximately 460-620 nm. In this range, the sample irradiated in nitrogen has a similar transmission spectrum as the undamaged sample. In contrast, the sample irradiated in air appears to have a constant degradation across all wavelengths.

Figure 7.7 shows the light yields spectrum for all the PEN samples. Right after the radiation exposure, the air sample yielded 70% light, and the N2 yielded 12% light. However, the results of the samples changed dramatically after 10 days exposure to fluorescent room lights. After they recovered from radiation damage, the air sample yielded 86% light, and the N2 sample yielded 94% light, indicating recovery by factors of 1.2 and 7.8 respectively, Fig. 7.7.

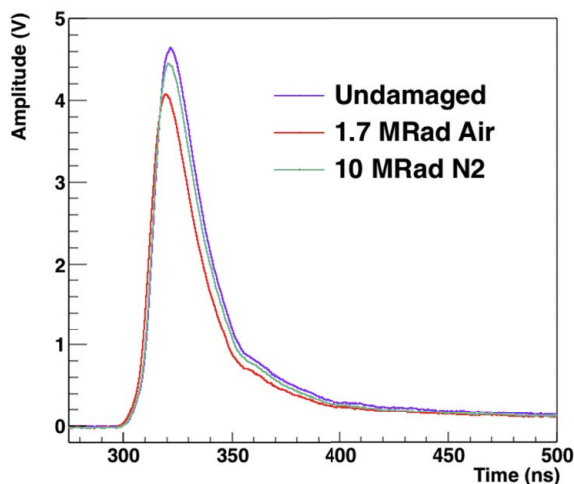
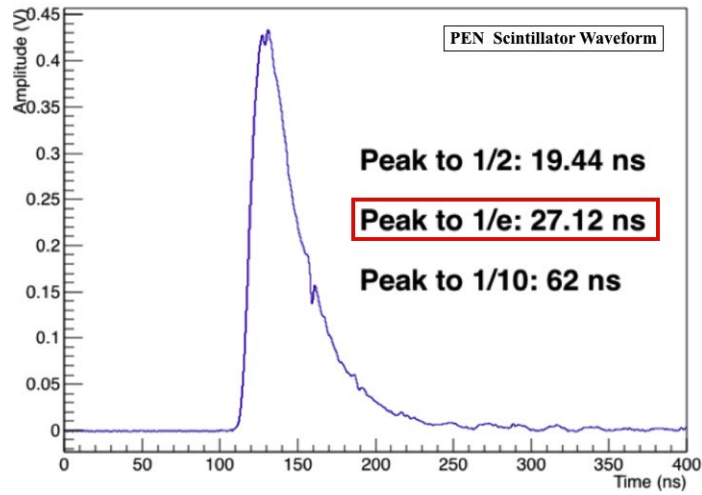


Figure 7.7: Scintillation (light yield) spectrum of the unirradiated and irradiated PEN samples

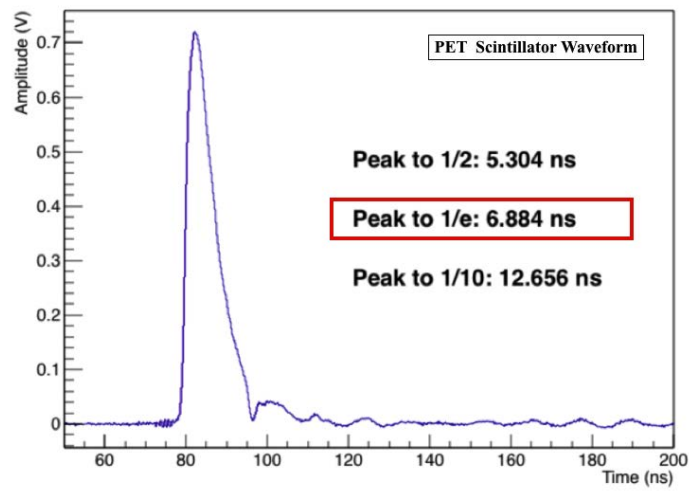
7.2.2 Timing Measurements

A new set of PEN, PET and HE tiles in sizes of 10 cm \times 10 cm with thickness of 0.1 cm, 0.2 cm and 0.5 cm, respectively were prepared and tested for timing characteristics in an experimental setup explained previously, Fig. 7.4 (b). The scintillation signal of each tile is recorded with Tektronix TDS 5034 digital oscilloscope and the saved waveform pulses were analyzed for timing.

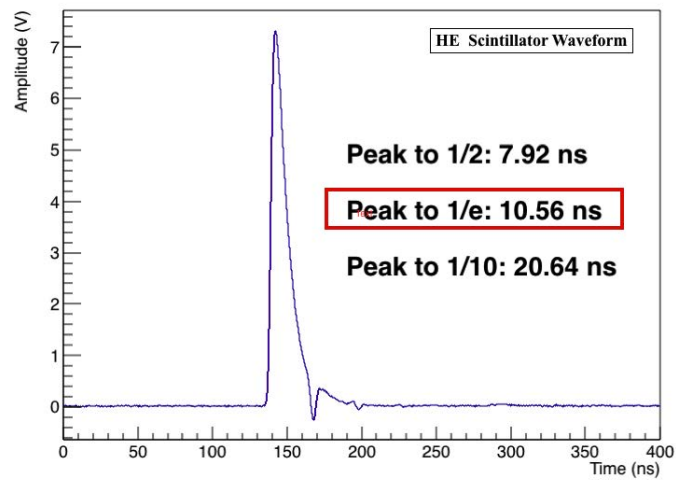
Figure 7.8 shows the timing characteristics of HE (a), PET (b) and PEN (c) [94]. Signal timing was calculated, which is the time takes to fall from peak to half ($1/2$), from peak to $1/e$ and from peak to $1/10$ of the signal. Peak to $1/e$ values for tiles, HE, PET and PEN are respectively 10.56 ± 0.32 ns, 6.884 ± 0.21 ns and 27.12 ± 0.81 ns. The errors associated with the results are only statistical errors. PET has a much faster response than the HE baseline tile, scintillator used in the CMS experiment, however PEN is slower.



(a)



(b)



(c)

Figure 7.8: Signal timing of PEN (a), PET (b) and Kuraray SCSN-81 HE Tile (c) [94].

7.2.3 Radiation Damage Studies

Two samples of PEN and PET were irradiated at 1.4 and 14 Mrad using gamma radiation from a ^{137}Cs source at the University of Iowa RadCore Facility. Their radiation hardness in terms of the light yield was measured afterwards. The sample size of the PEN and PET tiles are 10 cm x 10 cm x 0.1 cm and 10 cm x 10 cm x 0.2 cm, respectively. They were uniformly exposed to the radiation source.

Before and after the irradiation, the light yield of the samples were measured by using the experimental setup in Fig. 7.9. We used a control sample to calibrate the experimental setup before every measurement. Each sample was kept and tested in a temperature and humidity controlled room at 22.5 °C.

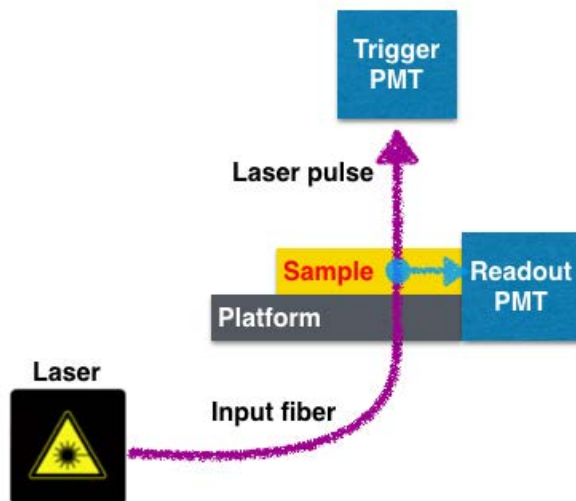


Figure 7.9: Experimental setup for the light yield measurement.

In the experimental setup, Fig. 7.9, we pulsed a 337 nm nitrogen laser with

a 3 ns pulse width perpendicular to the surface of the sample. The scintillated light was read out from the the edge of the tile with a directly coupled Hamamatsu R7600 PMT, triggered by a Hamamatsu R7525 PMT [107] on the top of the setup. The trigger R7525 PMT and the signal R7600 PMT were powered at 1700 V and 700 V, respectively and the signal was recorded using a Tektronix TDS 5034 digital oscilloscope [106]. For every measurement, 100 waveforms, triggered by 100 laser pulses, were averaged and the average waveform was saved. Each sample was removed, replaced, rotated, and retested four times to understand the systematic uncertainty on placement, which was found to be less than 5%.

Figure 7.10 shows the percent light loss after irradiation as a function of time for PEN at 1.4 Mrad (top left) and at 14 Mrad (top right), and PET at 1.4 Mrad (bottom left) and at 14 Mrad (bottom right) [92, 95].

Table 7.1 shows the initial light yield, recovered light yield and recovery time of PEN and PET, which are drawn from Fig. 7.10. Here, the initial light yield is the measured light yield compared to the undamaged sample immediately after the exposure. After some time, the tile recovers from the radiation damage and the light yield reaches to a maximum value (a plateau), which gives the recovered light yield and the recovery time is the time takes a sample to reach that plateau value.

Initially, PEN was damaged 28.6% at 1.4 Mrad and 53.3% at 14 Mrad and PET was damaged 65% at 1.4 Mrad and 87.8% at 14 Mrad. This shows that PET was damaged more than PEN initially. After the recovery, the permanant damage on PEN is 14.1% at 1.4 Mrad and 20.5% at 14 Mrad, and the permanent damage on

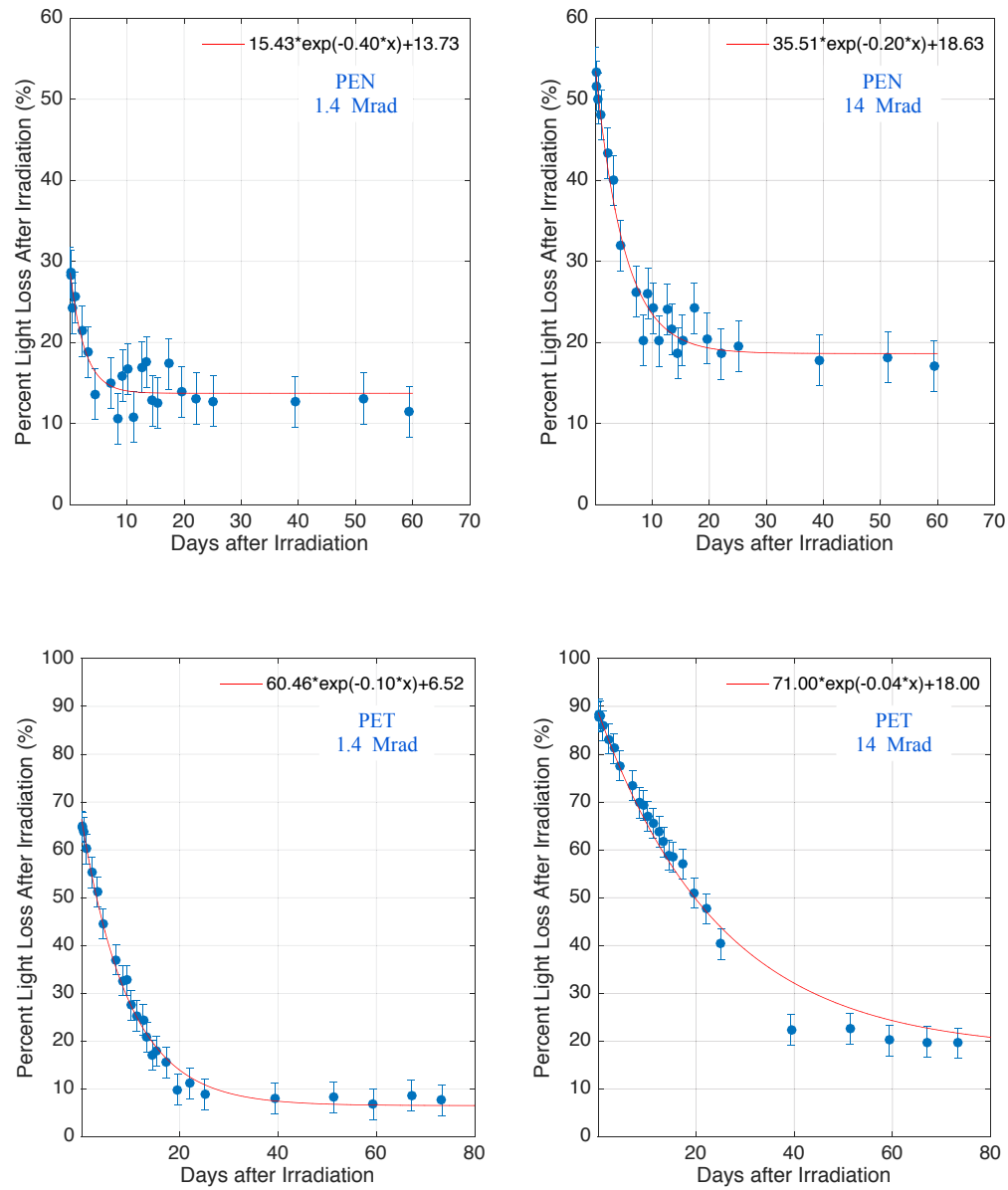


Figure 7.10: PEN and PET light yield results over 50 days after irradiation. PEN results, top left at 1.4 Mrad and top right at 14 Mrad and PET results, bottom left at 1.4 Mrad and bottom right at 14 Mrad [92,95].

PET is 6.5% at 1.4 Mrad and 20% at 14 Mrad. The permanent damage is almost same for both scintillators at 14 Mrad and PEN needs much shorter time than PET

Table 7.1: Summary of the PEN and PET light yield results [92].

	Initial Light Yield (%)		Recovered Light Yield (%)		Recovery Time (days)	
	1.4 Mrad	14 Mrad	1.4 Mrad	14 Mrad	1.4 Mrad	14 Mrad
PEN	71.4 ± 2.4	46.7 ± 2.7	85.9 ± 2.4	79.5 ± 2.7	5	9
PET	35.0 ± 2.4	12.2 ± 2.7	93.5 ± 2.4	80.0 ± 2.7	22	60

to recover.

7.2.4 LED Stimulated Recovery Studies

Four 5 cm x 5 cm x 0.1 cm PEN samples were prepared. Three of them placed into unsealed FoodSaver[®] vacuum bags and one of them evacuated and sealed (PEN vacuum sample), Fig. 7.5. The other two samples remained in unsealed bags (PEN air samples). The last sample was kept in the laboratory as a baseline for further calibration studies.

Samples were exposed to ^{137}Cs gamma source at RadCore facility at the University of Iowa up to 13.73 Mrad. Upon return, the light yield of the samples were measured and a baseline was recorded. One of the PEN air samples and vacuum sample was kept in a light-tight box between measurements. The other air sample was placed onto an array of tri-color (red-green-blue, RGB) LEDs, Fig. 7.11. The LEDs were connected to an Arduino Uno [108] and programmed to oscillate every 10 seconds between only red, only green, only blue, and all colors at the same time. A piece of light-reflective HEM foil was placed on top of the PEN sample, which was

further covered by a piece of light-tight Tedlar[®] [109]. This sample remained on the LED array between measurements.

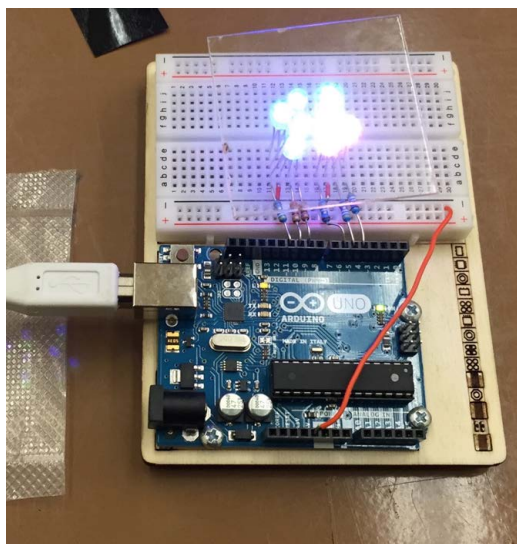


Figure 7.11: PEN sample resting on Arduino-powered “radiation damage recovery” LED array.

The samples’ light yields were measured by using the scintillation light yield setup in Fig. 7.9, discussed previously.

There were no significant differences in light yield among the three samples irradiated at the UI RadCore facility immediately after removal. This clearly indicates no effect on having a sample irradiated while under vacuum.

Figure 7.12 shows the light yields of different PEN samples after 3 days (a) and 7 days (b) [93]. After 3 days, there was a clear separation between the tiles recovering in the dark versus the tile recovering on the LED array, Fig. 7.12 (a). After 7 days, the sample left in the dark recovered to a maximum of 37%. In contrast, the PEN

sample exposed to RGB LEDs recovered to 70%, Fig. 7.12 (b). This implies that exposing the tiles to RGB LEDs light improves the overall recovery process.

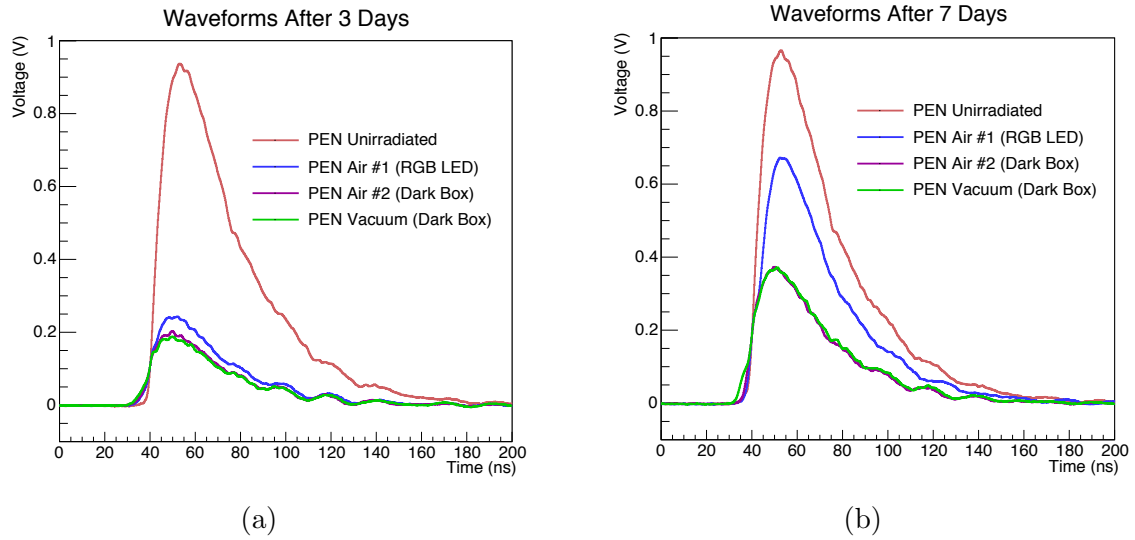


Figure 7.12: Scintillation (light yield) spectrum of PEN samples for recovery from 13.73 Mrad gamma ray exposure. (a) shows results for 3 days and (b) shows results after 7 days of the exposure [93].

These initial test results encouraged us to develop a more robust test of this novel method. New tests were developed with different brand of scintillators, which have peak emission wavelengths in blue and green spectrum regions. Lab produced SiX, Eljen brand EJ-260 (EJN) and Eljen brand over-doped EJ-260 (EJ2P) scintillators were tested in a separate irradiation. SiX and previously tested PEN are called blue scintillators, and EJN and EJ2P are called green scintillators due to their emission spectra.

In the new tests, two tiles of each SiX as 2.5 cm x 4.5 cm x 1 cm rectangles,

and both EJN and EJ2P as 2 cm x 3 cm x 1 cm rectangles were exposed to ^{137}Cs gamma source at UI RadCore facility and irradiated up to 14 Mrad. After irradiation, one of the samples of each scintillators were kept in a light-tight box and the other samples were placed onto an array of tri-color RGB LEDs as in Fig. 7.11, between measurements. These samples were tested immediately after irradiation, and in regular intervals up to 40 days until they reach to full recovery.

Figure 7.13 shows the recovery plots (percentage damage vs time) from radiation damage for samples of SiX (a), EJN (b) and EJ2P (c) [93]. Each plot shows the recovery of two samples; one was kept in a light-tight box and the other was placed on RGB LEDs.

The data points on each plot were fitted to an exponential function of the form, $a \times e^{-b \cdot x} + c$, in which ‘ a ’ represents the total recovery, ‘ b ’ represents the recovery constant, ‘ c ’ represents the permanent damage, and ‘ $a + c$ ’ represents the total initial damage of the tiles. According to fit parameters in Table 7.2, only SiX showed significant effect to RGB LEDs. The SiX sample placed on RGB LEDs recovering about 10% more (total recovery) and a day faster (4.55 vs 5.56 days) than the sample in the light-tight box. Neither EJN nor EJ2P scintillators showed significant effect to RGB LED recovery. The recovery characteristics of both EJN and EJ2P for samples in light-tight box and on RGB LEDs are almost the same.

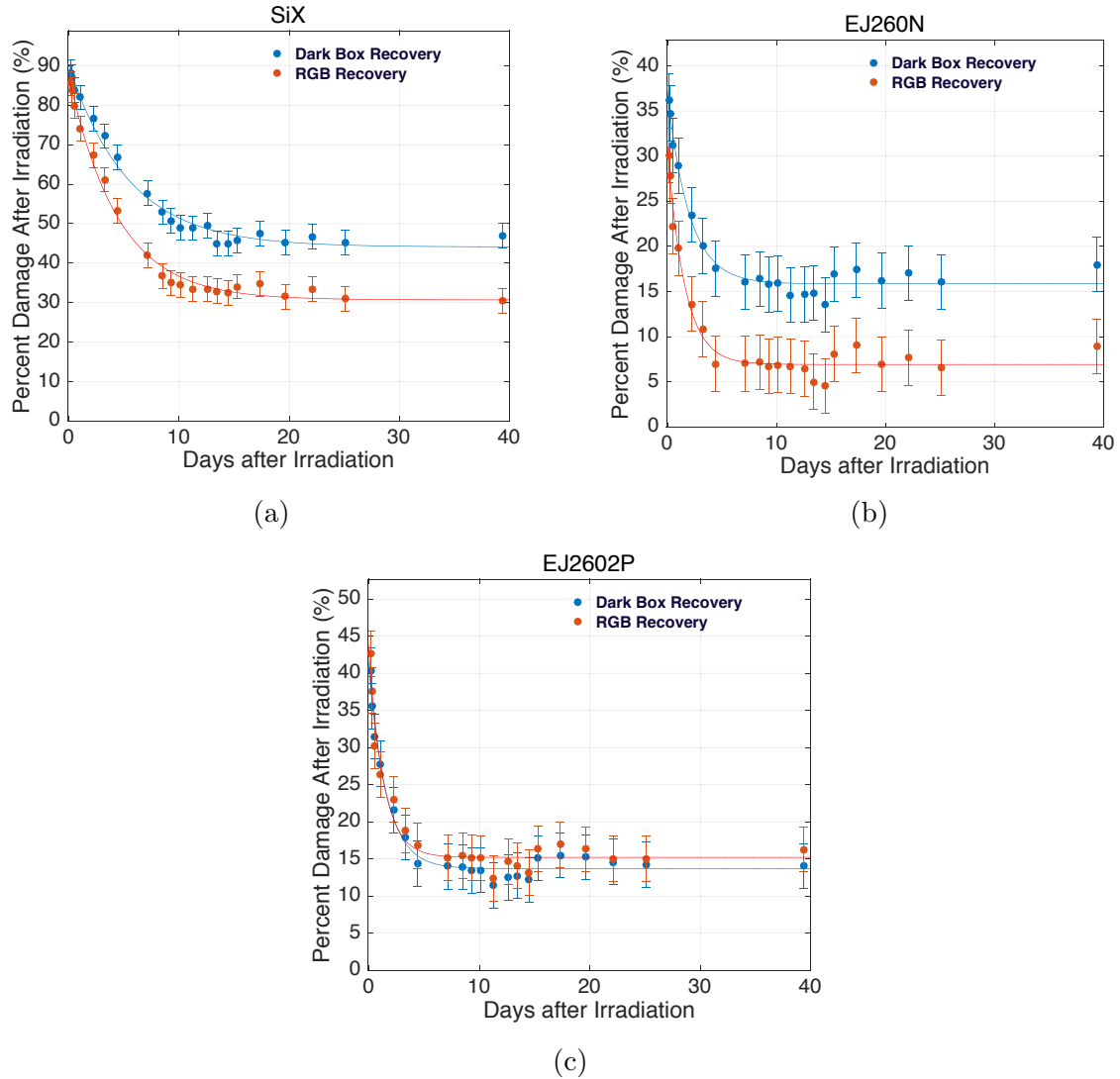


Figure 7.13: Percent damage on various tiles after irradiation. SiX (a), EJN (b), and EJ2P (c) tiles kept in dark box (Dark Box Recovery) and on RGB LEDs (RGB Recovery) over time [93].

These results with the combination of previous PEN results imply that so called blue scintillators, PEN and SiX respond to color spectrum but not the green scintillators, EJN and EJ2P.

Table 7.2: Summary of the recovery plots of SiX, EJN and EJ2P with fit parameters ‘ a ’, ‘ b ’, and ‘ c ’ of data points [93].

Tile	Total Recovery ‘ a ’	Permanent Damage ‘ c ’	Recovery Constant ‘ b ’ (days ⁻¹)
SiX RGB	$56.3 \pm 2.4\%$	$30.7 \pm 1.6\%$	0.22 ± 0.03
SiX dark box	$45.7 \pm 2.5\%$	$44.1 \pm 1.9\%$	0.18 ± 0.03
EJN RGB	$24.0 \pm 2.2\%$	$6.92 \pm 0.7\%$	0.64 ± 0.16
EJN dark box	$21.1 \pm 1.8\%$	$15.9 \pm 0.6\%$	0.50 ± 0.11
EJ2P RGB	$26.9 \pm 3.1\%$	$15.2 \pm 0.9\%$	0.75 ± 0.22
EJ2P dark box	$26.5 \pm 2.2\%$	$13.7 \pm 0.7\%$	0.62 ± 0.14

7.3 Test Beam Activities and Results

The assembled tiles were also tested at Fermilab Test Beam Facility (FTBF) in Batavia, IL, USA and CERN H2 Test Beam Area in Geneva, Switzerland with beams in order to validate the results of laboratory measurements and characterize the scintillators in a high-energy beam environment.

FTBF provides primary high-energy proton beams (120 GeV) at intensities around 1-300 kHz. The facility can also provides secondary particle beams (shower particles) consisting of pions (π), muons (μ), electrons (e^-), positrons (e^+) and kaons (K) of energies down to 1 GeV [110].

CERN H2 Test Beam Area provides primary proton beams at 400 GeV and secondary shower particle beams (e^- , e^+ , μ , π , K) at energies of 10-360 GeV [111].

In October 2014, we joined the test beam effort at CERN and tested various tiles such as quartz tile with pTp coating, quartz tile with AN coating, HEM, PEN, PET and HE (reference tile) with muons, minimum ionizing particles (MIPs). There

are five wire chambers (WC, A-E) and various sizes of trigger counters upstream of the experimental setup to select the straight MIP particles (muons) and trigger the tiles when MIPs pass through the tile.

Each tile had a size of 10 cm x 10 cm but a different thickness (0.1 cm to 0.5 cm) because of the manufacturing limits and was located in a light tight 3D printed scintillator case. The scintillation light from the tile is carried out with either a single WLS fiber (sigma shape), Fig. 7.3 (a) or several WLS fibers (bar shape), Fig. 7.3. WLS fiber or fibers from scintillators are connected to a ~ 1 m long clear optical fiber with optical connectors to carry the light outside of the beam active area. The clear optical fiber with an optical cookie at the other end couples directly to Hamamatsu R7600U-200-M4 PMTs located in Hadronic Forward (HF) readout box (RBX) prototype. The PMTs were powered at the same voltage, 700V and the ADC counts were recorded with a data acquisition system (DAQ). Figure 7.14 (a) shows several scintillator cases and a scintillator with bar shape WLS fibers connected to clear optical fiber in the case. Figure 7.14 (b) shows the test beam experimental setup.

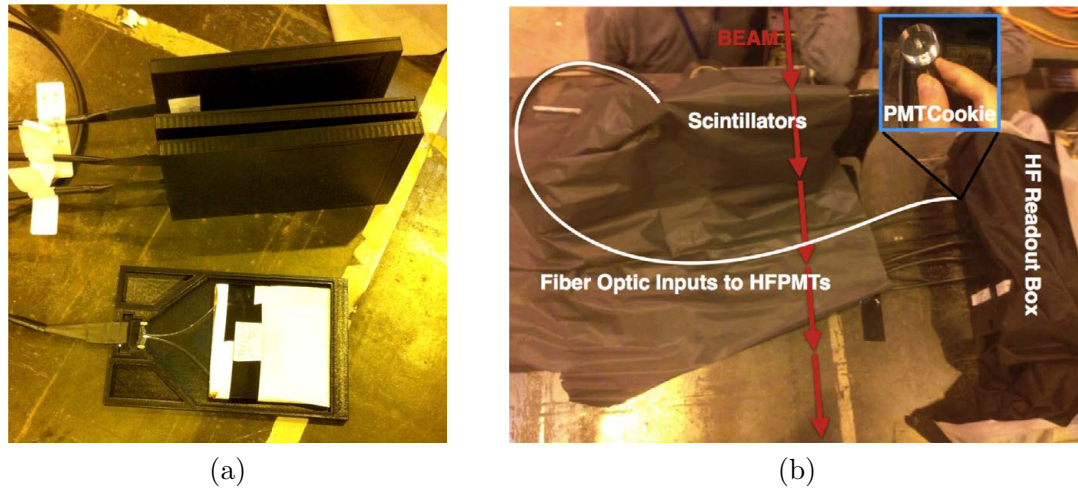


Figure 7.14: Light-tight 3D printed cases for tiles (a) and the experimental setup at CERN H2 Test Beam Area (b).

After performing the experiment, an analysis was performed to determine scintillation light yield, timing and response uniformity of the tiles. Corrections for thickness or geometry of the tiles and for WLS optical fibers were not included in this analysis.

Figure 7.15 shows the response uniformity of the same size PEN tiles, the first PEN sample with a single optical fiber as sigma shape (a) and the other PEN sample with several optical fibers as bar shape (b). The effects of the optical fiber in the tile and the shape of it are clearly seen.

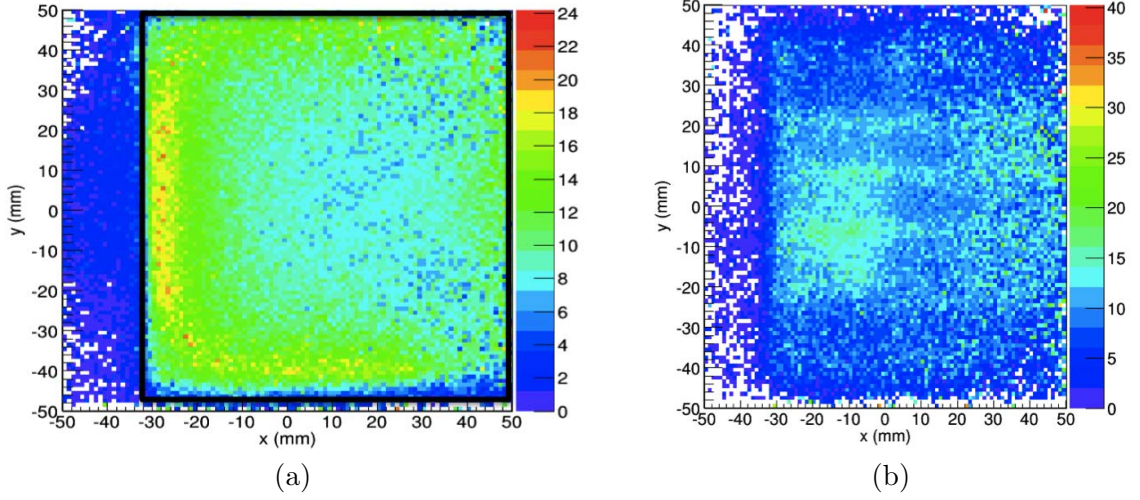


Figure 7.15: Response uniformity of PEN with different geometries PEN with a sigma shaped WLS fiber is in (a) and PEN with bar shaped WLS fibers is in (b).

Figure 7.16 shows the light yield response to MIPs (muons) of various tiles [94]. For this test, the same PMT was used [112]. The most probable values (MPVs) of the Landau fits to the charge spectra above 15 fC for PEN, PET, HEM, coated quartz with pTp and AN are compared with the baseline HE tile. The measured MPV of HE is 36.15 ± 0.15 fC and the other tiles have 29.22 ± 0.15 fC, 19.83 ± 0.78 fC, 23.86 ± 0.13 fC, 20.82 ± 0.55 fC and 22.8 ± 0.1 fC respectively. PEN has the closest response compared to HE. The systematic effects associated with WLS fiber coupling has not been studied in detail.

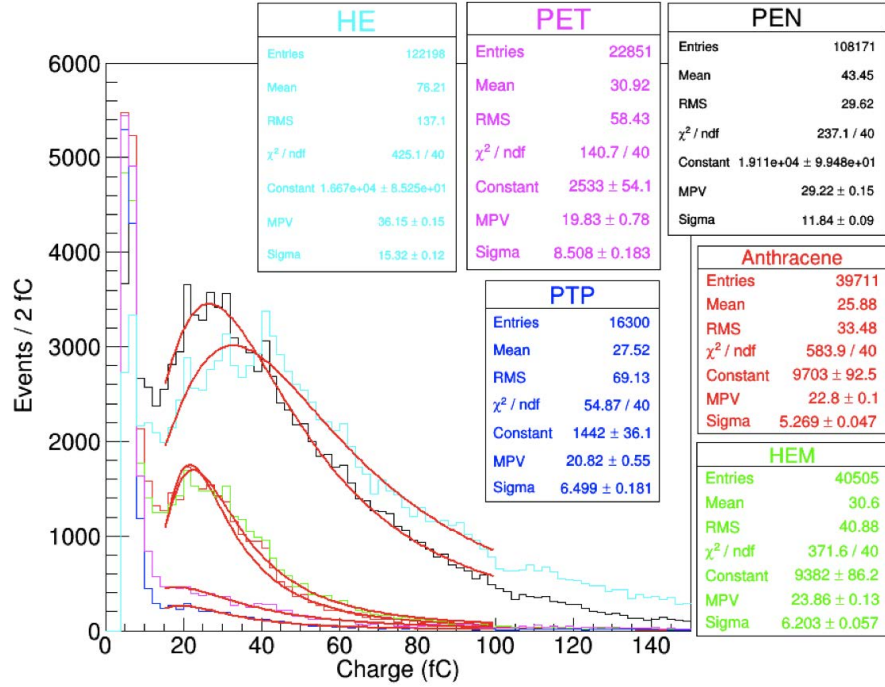


Figure 7.16: The MIP (muon) response of various tiles, tested at CERN H2 Test Beam Area [94].

During 2014-2016, we ran several beam tests for scintillators with primary protons (MIPs) and secondary shower beams (e, e^+, π, K) at FTBF. In these tests, the tiles' sizes were chosen same as the ones used at CERN beam test previously. We didn't have bar shape grooved tiles, shown in Fig. 7.3 (b), but only sigma shape grooved tiles with a single WLS fiber, shown in Fig. 7.3 (a). There are three wire chambers (WC1-WC3) and 1 cm^2 active area trigger counters upstream of the experimental setup to select the straight MIP (protons) and shower particles and trigger the tiles when they pass through the tile, Fig. 7.17 (a). Figure 7.17 (b) shows the experimental setup on a motion table at FTBF. A single tile with a WLS fiber located in a scintillator case was tested at a time. Again, $\sim 1 \text{ m}$ long clear optical fiber

connected to WLS carries the light and the other end with an optical cookie directly coupled to Hamamatsu R7600 PMT [112]. The signal from this single PMT was read out with a Tektronix TDS 5034 digital oscilloscope and average waveform for each tile was saved for further analysis.

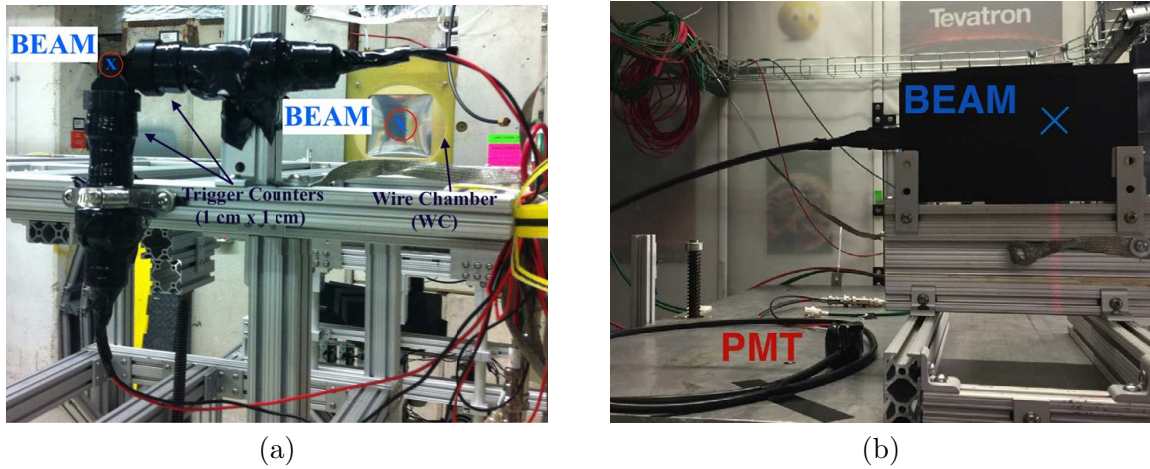


Figure 7.17: Experimental setup at Fermilab Test Beam Facility (FTBF). Trigger counters (1 cm x 1 cm active area) and Wire Chamber (WC) are shown in (a) and scintillator setup on a motion table at FTBF in (b).

Figure 7.18 shows the average scintillation waveform of quartz plate coated with p-Terphenyl (pTp) (a), quartz plate coated with Anthracene (AN) (b), and HE (black) and PEN (red) tile (c). Full width at half maximum (FWHM) was precisely calculated for HE and PEN only and it's 10.7 ns and 20.2 ns, respectively. FWHM is approximately ~ 14 ns and 27 ns for quartz coated with pTp and quartz coated with AN, respectively.

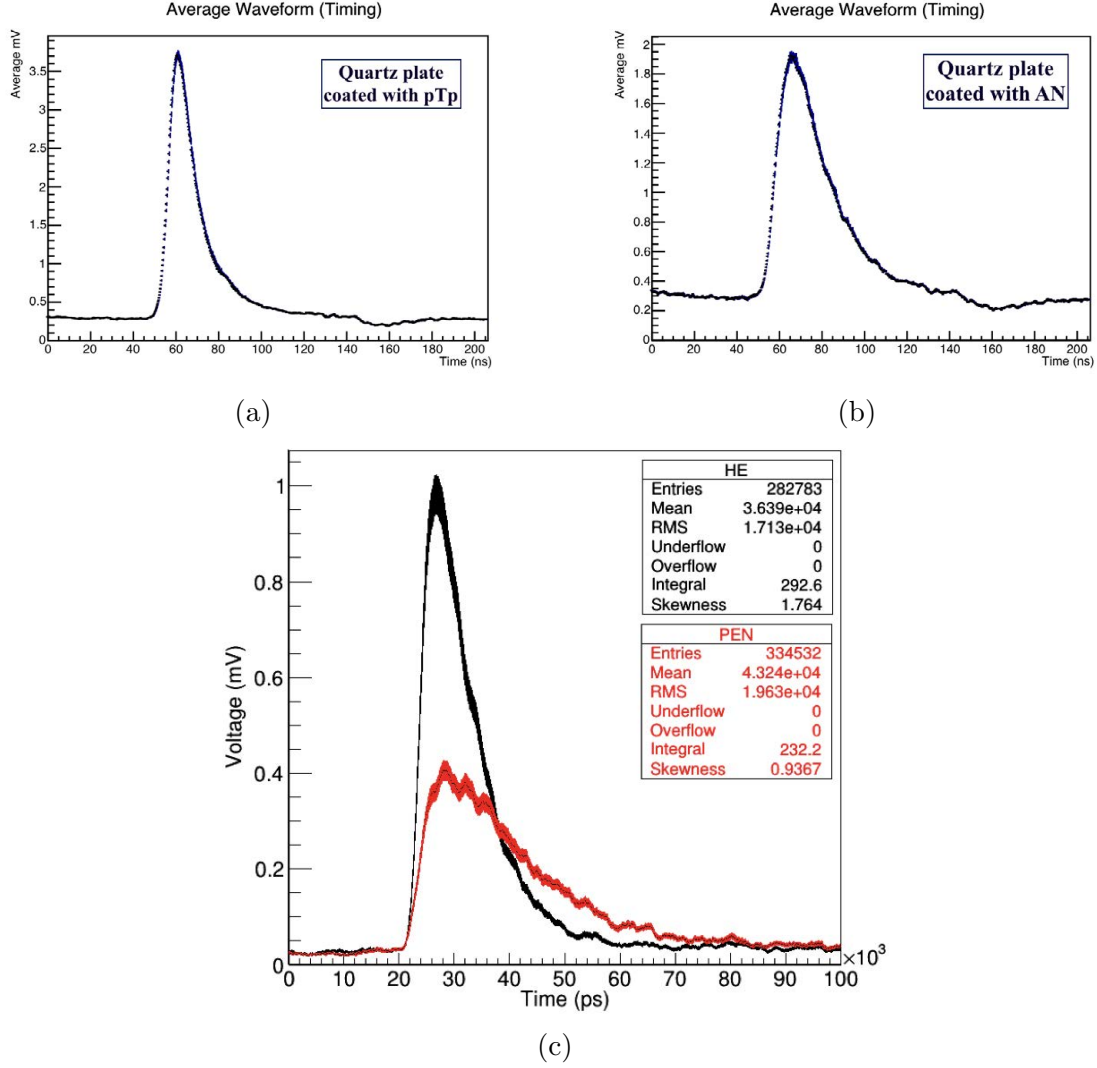


Figure 7.18: Average scintillation waveform of various tiles. The results are, quartz plate coated with pTp (a), quartz plate coated with AN (b), and HE and PEN tile (c).

7.4 Summary of Laboratory and Test Beam Studies

Table 7.3 shows the light yield and timing response summary of HE (SCSN-81), PEN, PET, quartz coated with pTp, quartz coated with AN, and HEM. In Table 7.3, *Light Yield* represents the MIP (muon) response results as most probable values

(MPV) in unit of fC of the tiles recorded at CMS-H2 Test Beam Area. *Timing at Lab* row represents the timing measurement results as peak to 1/e values (ns) recorded at the high energy physics (HEP) laboratory at UI with a UV light source and *Timing at TB* represents the timing measurements as FWHM values (ns) recorded at Fermilab Test Beam Facility (FTBF). The *n/a* in the table shows that those samples were not available during the tests and not tested. The HE tile is a well-known scintillator with its high light yield and fast timing characteristic and currently used as the active medium in the Hadron Endcap Calorimeters at CMS so its taken as a baseline tile here.

As can be seen in Table 7.3, the light yield PEN is much higher than PET but still lower than HE, baseline tile. Quartz-pTp, Quartz-AN and HEM have all lower light yields than HE but they are in acceptable range. However, PET has a faster time response than PEN, our baseline HE tile and all the other tiles, which is an incredible result. Quartz-pTp timing characteristic is also comparable with HE timing characteristic. According to these results, PEN, PET and Quartz plates specifically Quartz coated with pTp need to be kept for further analysis and investigated.

The systematic uncertainty for the timing measurements at the HEP laboratory at the UI and at test beam studies at Fermilab was found to be less than 5%. The errors on both light yield and timing measurements are only statistical errors, shown in Table 7.3. The statistical errors on the timing measurements were approximated to 3%.

Table 7.4 shows the summary of radiation responses of PEN, PET, SiX,

Table 7.3: Summary of light yield (MIP response) and timing responses of the scintillators.

Tiles	Light Yield (MPV, fC)	Timing at Lab (1/e, ns)	Timing at Test Beam (fwhm, ns)
HE	36.15 ± 0.15	10.56 ± 0.32	10.7 ± 0.32
PEN	29.22 ± 0.15	27.12 ± 0.81	20.2 ± 0.61
PET	19.83 ± 0.78	6.884 ± 0.21	n/a
Quartz-pTp	20.82 ± 0.55	n/a	13.52 ± 0.41
Quartz-AN	22.8 ± 0.10	n/a	25.51 ± 0.77
HEM	23.86 ± 0.13	n/a	n/a

EJ260N and EJ2602P scintillator tiles after they are exposed to ^{137}Cs gamma radiation up to 14 Mrad. In Table 7.4, *Light Loss* and *Light Loss-LED* rows represent the percentage of permanent damage for the tiles kept a light-tight box and on a RGB LED array, respectively. *Recovery Time* and *Recovery Time-LED* rows represent the recovery time (days) for the tiles, kept in a light-tight box and on a RGB LED array, respectively. The dash in the table shows that no test results available for those tiles since they were not available during the tests.

The results in Table 7.4 imply that the permanent damage is almost same for PEN and PET, it's much higher for SiX and it's much less for EJ260N and EJ2602P samples. RGB LED has a significant effect on the recovery of SiX, and it has a slight effect on EJ260N recovery but no effect on EJ2602P. In terms of recovery time, PEN needs much shorter time than PET but longer time than other samples. RGB LED machinery has shorten the recovery time of SiX only. Here, the superior results of EJ260N, EJ2602P and SiX are seen, but the fact remains that the PEN and PET

samples in these tests had a surface area ~ 9 times bigger than SiX sample and ~ 17 times bigger than both EJ260N and EJ2602P samples.

Table 7.4: Summary of radiation responses of the scintillators after ^{137}Cs gamma exposure up to 14 Mrad. LL is an abbreviation of Light Loss and RT is an abbreviation of Recovery Time.

Tiles	PEN	PET	SiX	EJ260N	EJ2602P
LL (%)	20.5 ± 0.7	20 ± 0.68	44.1 ± 1.9	15.9 ± 0.6	13.7 ± 0.7
LL-LED (%)	n/a	n/a	30.7 ± 1.6	6.92 ± 0.7	15.2 ± 0.9
RT (days)	9	60	5.6 ± 0.8	2 ± 0.4	1.6 ± 0.4
RT-LED (days)	n/a	n/a	4.5 ± 0.6	1.6 ± 0.4	1.3 ± 0.4

In conclusion, the radiation hardness, light yield and timing results of the tiles, PEN, PET, SiX and quartz plates and especially quartz coated with pTp are worthy of further investigation. Although the light yield of PEN is much higher than PET and the recovery time from radiation is faster than PET, PET has a faster time response than PEN and our baseline HE tile.

A blended sample of PEN and PET was produced and tested by H. Nakamura, et al. and the light yield of the blended substrate was measured at 0.85 times that of PEN and much higher than that of PET [113]. The blended sample is yet to be investigated for signal timing properties. A further investigation of a blended sample of PEN and PET will no doubt bring us substantial additions to our study.

CHAPTER 8

CONCLUSIONS AND FUTURE PERSPECTIVE

We have performed a search for new physics signal in two same sign electron (dielectron) channel due to a heavy Majorana neutrino (MN) using 19.7 fb^{-1} data collected by Compact Muon Solenoid (CMS) detector at the Large Hadron Collider (LHC) during 2012 pp collisions at a center-of-mass energy of 8 TeV. We extended the previous search limits for heavy MN mass (m_N) up to 500 GeV at high mass and 40 GeV at low mass. The mass range below $m_N = 40 \text{ GeV}$ is not considered in this study because of the low selection efficiency for the signal in this mass region. No excess events above the expected standard model background prediction is observed. The exclusion upper limits are set on $|V_{eN}|^2$ with a 95% confidence level (CL), where V_{eN} is the mixing element of the heavy Majorana neutrino with the standard model ν_e neutrino. The 95% CL exclusion limits on cross section times branching fraction are also set for $\sigma(pp \rightarrow Ne^\pm \rightarrow e^\pm e^\pm q\bar{q})$ as a function of m_N . The limits are $|V_{eN}|^2 < 0.020$ for $m_N = 90 \text{ GeV}$, $|V_{eN}|^2 < 0.017$ for $m_N = 200 \text{ GeV}$, $|V_{eN}|^2 < 0.71$ for $m_N = 500 \text{ GeV}$. At least an order of magnitude more stringent limits have been achieved on $|V_{eN}|^2$ than the limits previously set by CMS with the 7 TeV data. The limits are the most restricted limits for $m_N > 100 \text{ GeV}$ and the first limits for $m_N > 200 \text{ GeV}$ so far. The results of this study were published as a scientific paper in Journal of High Energy Physics (JHEP) in 2015 [51].

The second part of the thesis focuses on the detector research and development (R&D) for collider experiments and specifically CMS Phase I and Phase II

upgrades for the Hadronic Forward (HF) and Hadronic Endcap (HE) calorimeters. During the Phase I upgrade, the previous single-anode Hamamatsu R7525 PMTs at HF calorimeter were replaced with Hamamatsu R7600U-200-M4 multi-anode photo-multiplier tubes because of the large energy events detected by the previous PMTs. These large energy events resulted in fake background at the experiment. The new multi-anode PMTs with improved specifications were aimed to overcome large energy window event issues in the HF calorimeter, reduce fake background and make the experiment more efficient.

We tested gain, dark current, time characteristics and linearity of 1785 new multi-anode PMTs, which provide insights on the expected performance of the upgraded CMS detector. The vast majority ($\sim 99\%$) of multi-anode PMTs have low dark currents, below 1 nA and have high-gain, above 10^6 . They show fast timing characteristics with a transit time and pulse width less than 6 ns and rise time less than 3 ns. Only a few out of 1785 PMTs were shipped back to Hamamatsu due to either low gain or high dark current issues. The ones that passed the characterization tests were shipped to CERN and mounted to the experiment. They operate stably and are now being used to collect data at the CMS experiment. The results of this study was published at Journal of Instrumentation (JINST) in 2014 [83] and have been presented at multiple conferences and workshops [114].

In a separate study, we developed secondary emission readout modes as a simple bias modification in the voltage dividers of photomultiplier tubes with mesh and metal channel dynode structures. Hamamatsu single anode R7761 and multi-

anode R5900-00-M16 Photomultiplier Tubes have been characterized for use in the secondary emission modules. All the PMTs have low dark currents, below 1 nA for all the different operation modes. The multianode PMTs have a response non-uniformity of less than 3% across the anodes. Average gain for the R5900-00-M16 in Mode 1 is $15\text{-}30 \times 10^5$ and in Mode 2 is $2\text{-}20 \times 10^5$ for the range of operating voltages 800-1200 V. Average gain for R7761 is $6\text{-}9 \times 10^5$ both for Mode 1 and Mode 2, and in Mode 3 is $1\text{-}6 \times 10^5$ for the range of operating voltages 1500-2000 V. Both modules are operating stably and can serve as active layers in calorimetric measurements with beams in order to validate the concept of secondary emission calorimetry. The results of this study was published at JINST in 2016 [84] and also presented at many conferences.

In the last R&D project, we have investigated various scintillating materials for the upcoming Phase II upgrade of the CMS in specific and future particle physics experiments in general. We have introduced novel, radiation-hard and cheap scintillating materials such as Polyethylene Naphthalate (PEN), Polyethylene Terephthalate (PET), a lab produced plastic scintillator (SiX), high efficiency mirror (HEM) and quartz plates with various organic and inorganic coating materials such as p-Terphenyl (pTp), Anthracene (AN) and Gallium-doped Zinc Oxide (ZnO:Ga) to the high energy physics experiments. We have also tested Eljen brand EJ-260 (EJN), overdoped EJ-260 (EJ2P), and a known scintillator SCSN-81, for the CMS experiment. The radiation hardness, light yield and timing properties of the new materials have been studied at test stations at the University of Iowa (UI), Fermilab Test Beam Facility (FTBF) at Fermilab and CERN H2 Test Beam Area at CERN. In conclusion,

scintillator tiles, PEN, PET, SiX and quartz plates and especially quartz coated with pTp are worth to be investigated further. Although the light yield of PEN is much higher than PET and the recovery time from radiation is faster than PET, PET has a faster time response than PEN and our baseline HE tile. So, a blended sample of PEN and PET would be worth further investigation. The results of this study were published as scientific papers in JINST in 2016 [92] and Nuclear Instruments and Methods in Physics Research Section B (NIMB) in 2017 [93], and as several conference proceedings [94–97]. The results have been presented at many international conferences.

8.1 Future Work

The Majorana neutrino analysis with a new dataset at $\sqrt{s} = 13$ TeV collected by CMS detector at LHC is still ongoing. We are conducting optimization studies for s channel (dilepton + dijet) and t channel (trilepton + a neutrino). The trileptonic t channel was not studied previously with $\sqrt{s} = 8$ TeV dataset. The new dataset at $\sqrt{s} = 13$ TeV is expected to provide at least an order of magnitude better exclusion limits on $|V_{tN}|^2$ and cross section \times branching fraction when compared to dataset at $\sqrt{s} = 8$ TeV.

The detector research and development studies are also ongoing, specifically the radiation-hard and high light yield material search. We will continue to optimize the blending of the PEN and PET plastic scintillators for further investigations.

Recently, I have joined to the neutrino team at Iowa State University (ISU)

as a postdoctoral research associate to contribute neutrino physics effort at Fermilab. As a run coordinator, I am working on commissioning, operations and data analysis of the Accelerator Neutrino Neutron Interaction Experiment (ANNIE) [115] as well as operations and data analysis on the NuMI Off-Axis ν_e Appearance (NOvA) experiment [116] at Fermilab. ANNIE is located along the Booster Neutrino Beam (BNB) at Fermilab and it has a goal of measuring the final state neutron multiplicity from charged current neutrino-nucleus interactions within the gadolinium-loaded water. Currently, ANNIE is running in Phase-I and it will be upgraded to Phase-II in the summer of 2017, by installing Large Area Picosecond Photodetectors (LAPPDs) in the detector. LAPPDs are a novel photodetector technology with single photoelectron time resolutions less than 100 picoseconds, and spatial imaging capabilities to within a single centimeter. They will play a crucial role to separate events of charged-current quasi-elastic (CCQE) interactions and inelastic multi-track charged current interactions. NOvA is a long baseline neutrino oscillation experiment and it consists of two detectors; a near detector at Fermilab and a far detector in Minnesota along the NuMI (Neutrinos at the Main Injector) beamline.

APPENDIX A MAJORANA NEUTRINO SEARCH RESULTS IN $\mu^\pm\mu^\pm$ (DIMUON) + JETS EVENTS

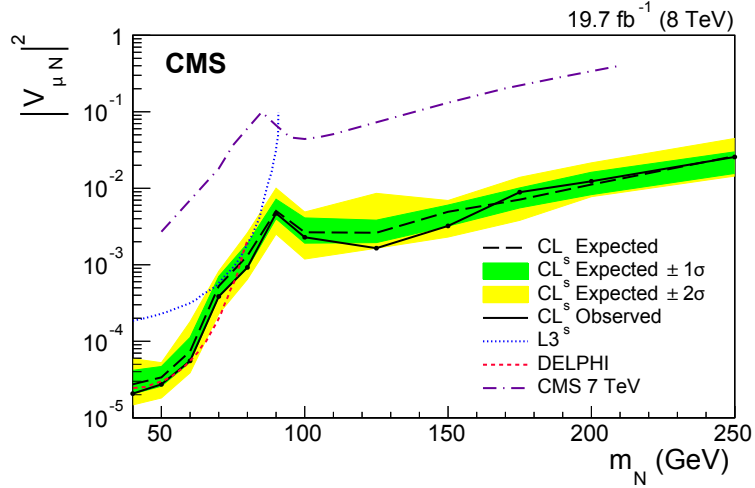
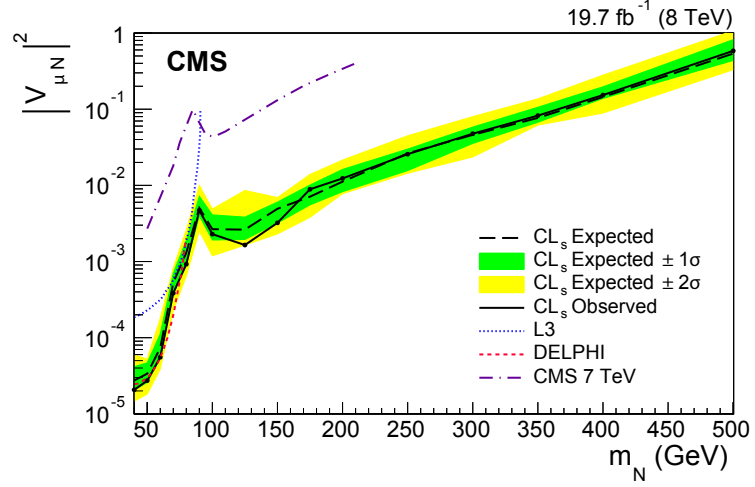


Figure A.1: Exclusion upper limits on $|V_{\mu N}|^2$ with a 95% CL as a function of Majorana neutrino mass, m_N (a) and expended view of the $40 \text{ GeV}/c^2 < m_N < 250 \text{ GeV}/c^2$ (b). The upper limits from direct searches from L3 and DELPHI collaborations, and the upper limits obtained by CMS experiment with the LHC data corresponding to $\sqrt{s} = 7 \text{ TeV}$, are also shown (CMS, 2015) [117].

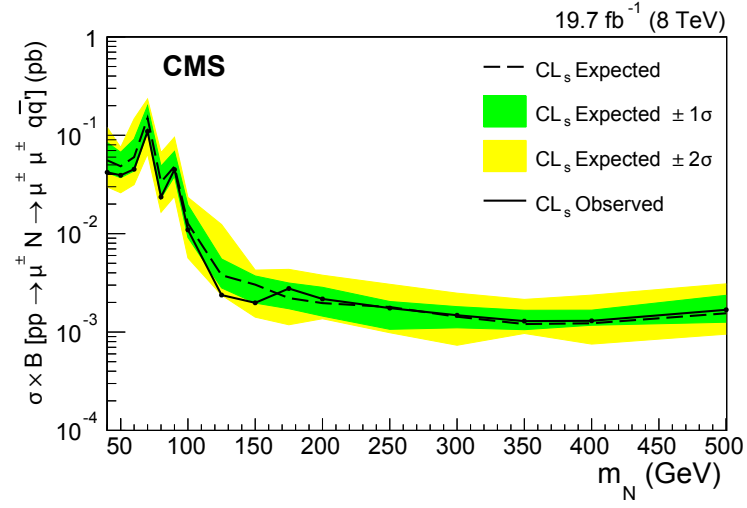


Figure A.2: Exclusion limits on cross section times branching fraction with a 95% CL as a function of Majorana neutrino mass, m_N (CMS, 2015) [117].

APPENDIX B
MAJORANA NEUTRINO SEARCH RESULTS IN $E^\pm\mu^\pm, \mu^\pm E^\pm + \text{JETS}$
EVENTS

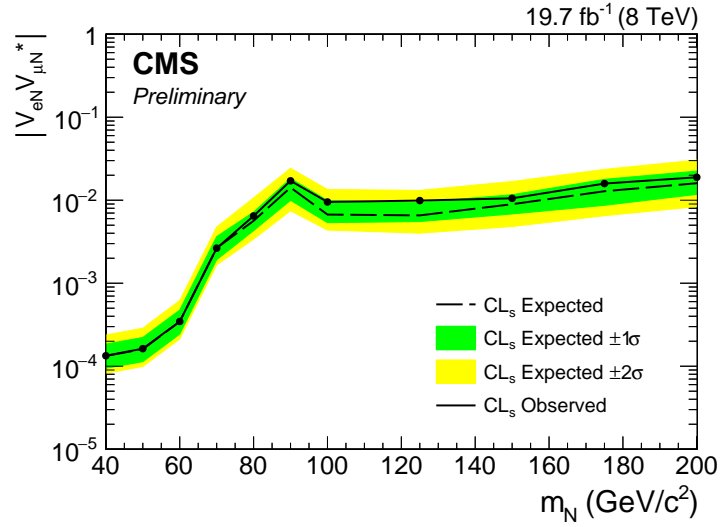
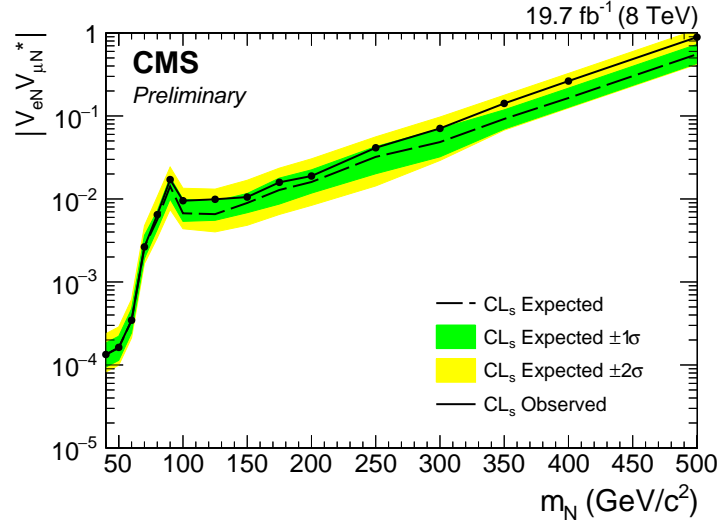


Figure B.1: Exclusion upper limits on $|V_{eN}V_{\mu N}^*|$ with a 95% CL as a function of Majorana neutrino mass, m_N (a) and expended view of the $40 \text{ GeV}/c^2 < m_N < 200 \text{ GeV}/c^2$ (b) (CMS, 2016) [51].

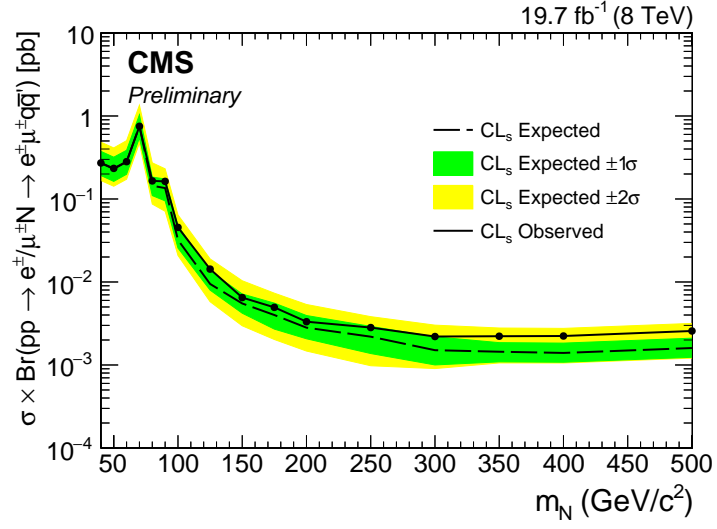


Figure B.2: Exclusion limits on cross section times branching fraction with a 95% CL as a function of Majorana neutrino mass, m_N (CMS, 2016) [51].

REFERENCES

- [1] Compact Muon Solenoid at LHC, 2016. <http://cms.web.cern.ch/>.
- [2] Large Hadron Collider at CERN, 2016. <http://home.cern/topics/large-hadron-collider>.
- [3] David J. Griffiths. *Introduction to Elementary Particles*. Weinheim: Wiley-VCH, 2nd edition, 2008.
- [4] Georges Aad et al. Observation of a new particle in the search for the Standard Model Higgs boson with the ATLAS detector at the LHC. *Phys. Lett.*, B716:1–29, 2012.
- [5] Serguei Chatrchyan et al. Observation of a new boson at a mass of 125 GeV with the CMS experiment at the LHC. *Phys. Lett.*, B716:30–61, 2012.
- [6] Particle Data Group. <http://pdg.lbl.gov/>.
- [7] V. Barger, D. Marfatia, and K. Whisnant. *The Physics of Neutrinos*. Princeton University Press, 2012.
- [8] R.N. Mohapatra and P.B. Pal. *Massive Neutrinos in Physics and Astrophysics*. World Scientific Publishing Company, 2004.
- [9] M. Fukugita and T. Yanagida. *Physics of neutrinos and applications to astrophysics*. Texts and monographs in physics. Springer, 2003.
- [10] Fred L Wilson. Fermi’s theory of beta decay. *American Journal of Physics*, 36(12):1150–1160, 1968.
- [11] C. L. Cowan, F. Reines, F. B. Harrison, H. W. Kruse, and A. D. McGuire. Detection of the free neutrino: A confirmation. *Science*, 124(3212):103–104, 1956.
- [12] C. S. Wu, E. Ambler, R. W. Hayward, D. D. Hoppes, and R. P. Hudson. Experimental test of parity conservation in beta decay. *Phys. Rev.*, 105:1413–1415, Feb 1957.
- [13] M. Goldhaber, L. Grodzins, and A. W. Sunyar. Helicity of neutrinos. *Phys. Rev.*, 109:1015–1017, Feb 1958.

- [14] K. Kodama et al. Observation of tau neutrino interactions. *Phys. Lett.*, B504:218–224, 2001.
- [15] B. Pontecorvo. Inverse beta processes and nonconservation of lepton charge. *Sov. Phys. JETP*, 7:172–173, 1958. [Zh. Eksp. Teor. Fiz.34,247(1957)].
- [16] Ziro Maki, Masami Nakagawa, and Shoichi Sakata. Remarks on the unified model of elementary particles. *Prog. Theor. Phys.*, 28:870–880, 1962.
- [17] Y. Fukuda et al. Evidence for oscillation of atmospheric neutrinos. *Phys. Rev. Lett.*, 81:1562–1567, 1998.
- [18] Q. R. Ahmad et al. Measurement of the rate of $\nu_e + d \rightarrow p + p + e^-$ interactions produced by 8B solar neutrinos at the Sudbury Neutrino Observatory. *Phys. Rev. Lett.*, 87:071301, 2001.
- [19] Q. R. Ahmad et al. Measurement of day and night neutrino energy spectra at SNO and constraints on neutrino mixing parameters. *Phys. Rev. Lett.*, 89:011302, 2002.
- [20] K. Eguchi et al. First results from KamLAND: Evidence for reactor anti-neutrino disappearance. *Phys. Rev. Lett.*, 90:021802, 2003.
- [21] M. H. Ahn et al. Measurement of Neutrino Oscillation by the K2K Experiment. *Phys. Rev.*, D74:072003, 2006.
- [22] CMS Luminosity (Public Results), 2016. <https://twiki.cern.ch/twiki/bin/view/CMSPublic/LumiPublicResults>.
- [23] CMS Technical Design Reports (TDRs), 2016. <https://cmsdoc.cern.ch/cms/cpt/tdr/>.
- [24] CMS Tracker Detector, 2016. <http://cms.web.cern.ch/news/tracker-detector>.
- [25] CMS Collaboration. *The CMS tracker: addendum to the Technical Design Report*. Technical Design Report CMS. CERN, Geneva, 2000. <https://cds.cern.ch/record/490194>.
- [26] CMS Electromagnetic Calorimeter, 2016. <http://cms.web.cern.ch/news/electromagnetic-calorimeter>.
- [27] CMS Hadronic Calorimeter, 2016. <http://cms.web.cern.ch/news/hadron-calorimeter>.

- [28] CMS Muon Detectors, 2016. <http://cms.web.cern.ch/news/muon-detectors>.
- [29] LHC Upgrade Schedule, 2016. <https://lhc-commissioning.web.cern.ch/lhc-commissioning/>.
- [30] CMS Collaboration. Technical proposal for the upgrade of the CMS detector through 2020. Technical Report CERN-LHCC-2011-006. LHCC-P-004, Jun 2011. <https://cds.cern.ch/record/1355706>.
- [31] D. Contardo, M. Klute, J. Mans, L. Silvestris, and J. Butler. Technical Proposal for the Phase-II Upgrade of the CMS Detector. Technical report, Geneva, Jun 2015. <http://cds.cern.ch/record/2020886>.
- [32] C. Athanassopoulos and et al. Results on $\nu_\mu \rightarrow \nu_e$ neutrino oscillations from the lsnd experiment. *Phys. Rev. Lett.*, 81:1774–1777, Aug 1998.
- [33] S. Hatakeyama and et al. Measurement of the flux and zenith-angle distribution of upward through-going muons in kamiokande ii+iii. *Phys. Rev. Lett.*, 81:2016–2019, Sep 1998.
- [34] Peter Minkowski. $\mu \rightarrow e\gamma$ at a Rate of One Out of 1-Billion Muon Decays? *Phys.Lett.*, B67:421, 1977.
- [35] M. Gell-Mann, P. Ramond, and R. Slansky. In P.V. Nieuwenhuizen and D.Z. Freedman, editors, *Supergravity: proceedings of the Supergravity Workshop at Stony Brook*, page 315. North-Holland, 1979.
- [36] T. Yanagida. In O. Sawada and A. Sugamoto, editors, *Proceedings of the Workshop on the Unified Theory and the Baryon Number in the Universe*, page 95. National Laboratory for High Energy Physics (KEK), 1979.
- [37] Rabindra N. Mohapatra and Goran Senjanovic. Neutrino Mass and Spontaneous Parity Violation. *Phys.Rev.Lett.*, 44:912, 1980.
- [38] M. Magg and C. Wetterich. Neutrino Mass Problem and Gauge Hierarchy. *Phys. Lett.*, 94B:61–64, 1980.
- [39] J. Schechter and J. W. F. Valle. Neutrino Decay and Spontaneous Violation of Lepton Number. *Phys. Rev.*, D25:774, 1982.
- [40] Robert Foot, H. Lew, X. G. He, and Girish C. Joshi. Seesaw Neutrino Masses Induced by a Triplet of Leptons. *Z. Phys.*, C44:441, 1989.

- [41] J. Schechter and J. W. F. Valle. Neutrino Masses in $SU(2) \times U(1)$ Theories. *Phys. Rev.*, D22:2227, 1980.
- [42] T. P. Cheng and Ling-Fong Li. Neutrino Masses, Mixings and Oscillations in $SU(2) \times U(1)$ Models of Electroweak Interactions. *Phys. Rev.*, D22:2860, 1980.
- [43] Wai-Yee Keung and Goran Senjanovic. Majorana Neutrinos And The Production Of The Right-Handed Charged Gauge Boson. *Phys.Rev.Lett.*, 50:1427, 1983.
- [44] Duane A. Dicus, Debra Dzialo Karatas, and Probir Roy. Lepton nonconservation at supercollider energies. *Phys.Rev.*, D44:2033–2037, 1991.
- [45] A. Datta, M. Guchait, and A. Pilaftsis. Probing lepton number violation via majorana neutrinos at hadron supercolliders. *Phys.Rev.*, D50:3195–3203, 1994.
- [46] Jr. Almeida, F.M.L., Yara Do Amaral Coutinho, Jose Antonio Martins Simoes, and M.A.B. do Vale. On a signature for heavy Majorana neutrinos in hadronic collisions. *Phys.Rev.*, D62:075004, 2000. Latex2e(epsfig), 12 pages, 8 figures, to appear Physical Review D.
- [47] O. Panella, M. Cannoni, C. Carimalo, and Y.N. Srivastava. Signals of heavy Majorana neutrinos at hadron colliders. *Phys.Rev.*, D65:035005, 2002.
- [48] Tao Han and Bin Zhang. Signatures for Majorana neutrinos at hadron colliders. *Phys.Rev.Lett.*, 97:171804, 2006.
- [49] Anupama Atre, Tao Han, Silvia Pascoli, and Bin Zhang. The Search for Heavy Majorana Neutrinos. *JHEP*, 0905:030, 2009.
- [50] F. del Aguila, J.A. Aguilar-Saavedra, and R. Pittau. Heavy neutrino signals at large hadron colliders. *JHEP*, 0710:047, 2007.
- [51] CMS Collaboration. Search for heavy Majorana neutrinos in $e^\pm e^\pm$ +jets and $e^\pm \mu^\pm$ +jets events in proton-proton collisions at $\sqrt{s} = 8$ TeV. *JHEP*, 1604:169, 2016.
- [52] Search for heavy Majorana neutrinos in $e^\pm e^\pm$ +jets and $e^\pm \mu^\pm$ +jets events in proton-proton collisions at $\sqrt{s} = 8$ TeV. Technical Report CMS-PAS-EXO-14-014, CERN, Geneva, 2015.
- [53] J. Almond et al. Search for heavy majorana neutrinos in same-sign dielectron events in pp collisions at $\sqrt{s} = 8$ tev. *CMS Note*, AN-14-204, 2015.

- [54] O. Adriani et al. Search for isosinglet neutral heavy leptons in Z0 decays. *Phys.Lett.*, B295:371–382, 1992.
- [55] P. Abreu et al. Search for neutral heavy leptons produced in Z decays. *Z.Phys.*, C74:57–71, 1997.
- [56] The CMS Collaboration. Search for heavy Majorana neutrinos in $\mu^\pm\mu^\pm$ + jets and $e^\pm e^\pm$ + jets events in pp collisions at $\sqrt{s} = 7$ TeV. *Phys. Lett.*, B717:109–128, 2012.
- [57] The ATLAS Collaboration. Search for majorana neutrino production in pp collisions at sqrt(s)=7 TeV in dimuon final states with the atlas detector. 2012.
- [58] J. Almond. *A Search for a Heavy Majorana Neutrino at ATLAS Using 4.7 fb⁻¹ of pp Collisions at $\sqrt{s} = 7$ TeV*. Ph.D., The University of Manchester, 2012.
- [59] M. L. Mangano, M. Moretti, F. Piccinini, R. Pittau, and A. D. Polosa. ALP-GEN, a generator for hard multiparton processes in hadronic collisions. 2003.
- [60] Torbjorn Sjostrand, Stephen Mrenna, and Peter Z. Skands. PYTHIA 6.4 physics and manual. *JHEP*, 0605:026, 2006.
- [61] S. Agostinelli et al. GEANT4: A Simulation toolkit. *Nucl.Instrum.Meth.*, A506:250–303, 2003.
- [62] Ryan Gavin, Ye Li, Frank Petriello, and Seth Quackenbush. FEWZ 2.0: A code for hadronic Z production at next-to-next-to-leading order. *Comput. Phys. Commun.*, 182:2388–2403, 2011.
- [63] Ryan Gavin, Ye Li, Frank Petriello, and Seth Quackenbush. W Physics at the LHC with FEWZ 2.1. *Comput. Phys. Commun.*, 184:208–214, 2013.
- [64] The CMS Collaboration. Description and performance of track and primary-vertex reconstruction with the CMS tracker. *Journal of Instrumentation*, 9(10):P10009, 2014.
- [65] CMS EGamma Twiki Page. <https://twiki.cern.ch/twiki/bin/viewauth/CMS/EgammaCutBasedIdentification>.
- [66] CMS EGamma Physics Object Group Twiki Page. <https://twiki.cern.ch/twiki/bin/view/CMS/EgammaPOG>.
- [67] The CMS Collaboration. Performance of cms muon reconstruction in pp collisions at $\sqrt{s} = 7$ tev. *CMS Physics Analysis Summary*, CMS-PAS-MOU-10-004, 2010.

- [68] CMS JetMET Twiki Page. <https://twiki.cern.ch/twiki/bin/view/CMS/JetMET>.
- [69] CMS MET Filter Twiki Page. <https://twiki.cern.ch/twiki/bin/viewauth/CMS/MissingETOptionalFilters>.
- [70] G. Punzi. Sensitivity of searches for new signals and its optimization. 2003.
- [71] SSDilep2013 CMS Twiki Page. <https://twiki.cern.ch/twiki/bin/viewauth/CMS/SameSignDilepton2013>.
- [72] W. Andrews and et. al. Search for higgs boson decay to two w bosons in the fully leptonic final state at $\sqrt{7}$ tev with 2011 data with the cms detector. *CMS Note*, AN-2011-147, 2011.
- [73] D. Barge and et. al. Inclusive search for new physics with same-sign dileptons using early lhc data. *CMS Note*, AN-2010-247, 2010.
- [74] D. Barge and et. al. Search for new physics with same-sign dileptons using the 2011 dataset of cms. *CMS Note*, AN-2011-258, 2011.
- [75] G. Bauer, J. Bendavid, E. Butz, et al. Lepton efficiencies for the inclusive w cross section measurement with 36.1 pb^{-1} . *CMS Note*, AN-2011-097, 2011.
- [76] L. K. Saini, I. Kravchenko, and Y. Maravin. A study of efficiencies and scale factors for cut-based electron identification at cms experiment using data from proton-proton collisions at $\sqrt{s}=8$ tev. *CMS Note*, AN-2014-055, 2014.
- [77] CMS Collaboration. The egamma id group, tag and probe methodology for analyses using electrons and photons. *CMS Note*, CMS Note AN-2012-116, 2012.
- [78] Tag and Probe Study. http://home.fnal.gov/~etiras/index_tnp_bwcb.html.
- [79] E. Tiras. *Characterization of 900 four-anode photomultiplier tubes for use in 2013 hadronic forward calorimeter upgrade*. M.Sc., University of Iowa, 2012.
- [80] Burak Bilki et al. Tests of CMS hadron forward calorimeter upgrade readout box prototype. *JINST*, 2012.
- [81] A. R. Moeller. *Forward physics in CMS: simulation of PMT hits in HF and Higgs mass reconstruction methods with a focus on forward jet tagging*. Ph.D., The University of Iowa, 2014.

- [82] The CMS Collaboration. Missing transverse energy performance of the CMS detector. *JINST*, 6(09):P09001, 2011.
- [83] Ugur Akgun et al. Characterization of 1800 Hamamatsu R7600-M4 PMTs for CMS HF Calorimeter upgrade. *JINST*, 9:T06005, 2014.
- [84] E. Tiras, K. Dilsiz, H. Ogul, D. Southwick, B. Bilki, J. Wetzel, J. Nachtman, Y. Onel, and D. Winn. Characterization of photomultiplier tubes in a novel operation mode for secondary emission ionization calorimetry. *JINST*, 11(10):P10004, 2016.
- [85] Robert G. Lye and A. J. Dekker. Theory of secondary emission. *Phys. Rev.*, 107:977–981, Aug 1957.
- [86] David R. Winn and Yasar Onel. Secondary emission calorimeter sensor development. volume 404, page 012021, 2012.
- [87] A. Albayrak-Yetkin et al. In *Secondary Emission Calorimetry: Fast and Radiation-Hard*, 2013.
- [88] Hamamatsu Photonics, 2016.
- [89] A. Artikov et al. CDF central preshower and crack detector upgrade. 2007.
- [90] C. Grozis et al. The time-of-flight detector at CDF. *Nucl. Phys. Proc. Suppl.*, 93:344–347, 2001.
- [91] R. Blair et al. The CDF-II detector: Technical design report. 1996.
- [92] J. Wetzel, E. Tiras, B. Bilki, Y. Onel, and D. Winn. Radiation Damage and Recovery Properties of Common Plastics PEN (Polyethylene Naphthalate) and PET (Polyethylene Terephthalate) Using a ^{137}Cs Gamma Ray Source Up To 1.4 Mrad and 14 Mrad. *JINST*, 11:P08023, 2016.
- [93] J. Wetzel, E. Tiras, B. Bilki, Y. Onel, and D. Winn. Using LEDs to stimulate the recovery of radiation damage to plastic scintillators. *Nuclear Instruments and Methods in Physics Research Section B: Beam Interactions with Materials and Atoms*, 395:13 – 16, 2017.
- [94] Tiras E. Radiation Hard & High Light Yield Scintillator Search for CMS Phase II Upgrade. *Proceedings, Meeting of the APS DPF*, 2015.
- [95] E. Tiras, J. Wetzel, B. Bilki, D. Winn, and Y. Onel. Development of Radiation Hard Scintillators. *Proceedings of Science*,, 2016.

- [96] B. Bilki, Y. Onel, E. Tiras, J. Wetzel, and D. Winn. New Radiation-Hard Wavelength Shifting Fibers. *IEEE Transactions on Nuclear Science*, 2017. Accepted.
- [97] B. Bilki, Y. Onel, E. Tiras, J. Wetzel, and D. Winn. Radiation Damage Studies of New Intrinsically Radiation-Hard Scintillators. *IEEE Transactions on Nuclear Science*, 2017. Accepted.
- [98] CMS Collaboration. Technical proposal for the upgrade of the CMS detector through 2020. Technical Report CERN-LHCC-2011-006. LHCC-P-004, CERN, Geneva, Jun 2011.
- [99] Burak Bilki and CMS HCAL Collaboration. CMS Hadron Endcap Calorimeter upgrade studies for Super-LHC. *Journal of Physics: Conference Series*, 293(1):012068, 2011.
- [100] Stephen E Derenzo, Marvin J Weber, and Mattias K Klintonberg. Temperature dependence of the fast, near-band-edge scintillation from CuI, HgI₂, PbI₂, ZnO:Ga and CdS:In. *Nuclear Instruments and Methods in Physics Research Section A: Accelerators, Spectrometers, Detectors and Associated Equipment*, 486(1):214–219, 2002.
- [101] M. Dettmann et al. Radiation hard elastomer scintillators for a new generation of particle detectors. *Journal of Instrumentation*, JINST 23 P0716, 2017.
- [102] Teijin Limited. <http://www.teijin.com>. Accessed: 06-07-2017.
- [103] H. Nakamura, Y. Shirakawa, S. Takahashi, and H. Shimizu. Evidence of deep-blue photon emission at high efficiency by common plastic. *EPL (Europhysics Letters)*, 95(2):22001, 2011.
- [104] D. Fluhs et al. Polyethylene naphthalate scintillator: A novel detector for the dosimetry of radioactive ophthalmic applicators. *Ocular Oncology and Pathology*, v.2(1), 2015.
- [105] Ocean Optics PX-2 Xenon Light Source. <https://oceanoptics.com/product/px-2/>. Accessed: 06-07-2017.
- [106] Tektronix TDS5034 Oscilloscope. <http://www.tek.com/datasheet/tds5000-series-digital-phosphor-oscilloscope>. Accessed: 06-07-2017.
- [107] U Akgun, A S Ayan, G Aydin, F Duru, J Olson, and Y Onel. Afterpulse timing and rate investigation of three different hamamatsu photomultiplier tubes. *Journal of Instrumentation*, 3(01):T01001, 2008.

- [108] D. K. Fisher. Open-source hardware is a low-cost alternative for scientific instrumentation and research. *Modern Instrumentation*, 1, 2012.
- [109] Dupont Tedlar. <http://www.dupont.com/products-and-services/membranes-films/pvf-films/brands/tedlar-pvf-films.html>. Accessed: 06-07-2017.
- [110] Fermilab Test Beam Facility. <http://ftbf.fnal.gov/>. Accessed: 06-13-2017.
- [111] CERN H2 Test Beam Area. <http://sba.web.cern.ch/sba/BeamsAndAreas/h2/H2manual.html>. Accessed: 06-13-2017.
- [112] Hamamatsu R7600-00-M16 Multianode Photomultiplier Tube. <http://www.hamamatsu.com/us/en/product/alpha/P/3002/H8711/index.html>. Accessed: 06-07-2017.
- [113] H. Nakamura, Y. Shirakawa, H. Kitamura, T. Yamada, Z. Shidara, T. Yokozuka, P. Nguyen, T. Takahashi, and S. Takahashi. Blended polyethylene terephthalate and polyethylene naphthalate polymers for scintillation base substrates. *Radiation Measurements*, 59:172 – 175, 2013.
- [114] E. Tiras, B. Bilki, and Y. Onel. Commissioning of CMS Forward Hadron Calorimeters with Upgraded Multi-anode PMTs and μ TCA Readout. *Proceedings of Science*, 2016.
- [115] I. Anghel et al. Letter of Intent: The Accelerator Neutrino Neutron Interaction Experiment (ANNIE). Technical report, 2015.
- [116] D. S. Ayres et al. NOvA: Proposal to Build a 30 Kiloton Off-Axis Detector to Study $\nu_\mu \rightarrow \nu_e$ Oscillations in the NuMI Beamline. Technical report, 2004.
- [117] V. Khachatryan et al. Search for heavy Majorana neutrinos in $\mu^\pm\mu^\pm +$ jets events in proton-proton collisions at $\sqrt{s} = 8$ TeV. *Phys. Lett.*, B748:144–166, 2015.